OPTIMAL PATH PLANNING FOR SINGLE AND MULTIPLE AIRCRAFT USING A REDUCED ORDER FORMULATION

A Thesis
Presented To
The Academic Faculty

By

Shannon S. Twigg

In Partial Fulfillment
Of the Requirements for the Degree
Doctor of Philosophy in Aerospace Engineering

Georgia Institute of Technology

May, 2007

OPTIMAL PATH PLANNING FOR SINGLE AND MULTIPLE AIRCRAFT USING A REDUCED ORDER FORMULATION

Approved by:

Dr. Eric N. Johnson
School of Aerospace Engineering
Georgia Institute of Technology

Dr. Eric Feron
School of Aerospace Engineering
Georgia Institute of Technology

Dr. Anthony Calise
School of Aerospace Engineering
Georgia Institute of Technology

Dr. J. Eric Corban
Guided Systems Technology

Dr. Panagiotis Tsiotras
School of Aerospace Engineering
Georgia Institute of Technology

Date Approved: April 6, 2007

TABLE OF CONTENTS

LIST OF TABLES

LIST OF FIGURES

CHAPTER 1

INTRODUCTION

High-flying unmanned reconnaissance and surveillance systems are now being used extensively in the United States military. Current development programs are producing demonstrations of next-generation unmanned flight systems that are designed to perform combat missions. Their use in first-strike combat operations will dictate operations in densely cluttered environments that include unknown obstacles and threats, and will require the use of terrain for masking. The demand for autonomy of operations in such environments dictates the need for advanced trajectory optimization capabilities. In addition, the ability to coordinate the movements of more than one aircraft in the same area is an emerging challenge.

There are presently many different methods being used to solve trajectory problems for both single and multiple vehicles. Most of these methods commonly consist of different ways of stringing together pre-determined potential flight segments into an optimal or near-optimal path. These include using a Hybrid A^* algorithm, Voroni polygons, probabilistic maps and other graphical methods. Some researchers are also experimenting with various analytical techniques to solve these path-planning problems, including singular perturbation, genetic algorithms and neighboring optimal control as well as other analytical techniques.

Many determine UAV trajectories using a Hybrid A^* or similar search tree algorithm. This consists of optimizing the trajectory based on any specified cost function using a library of predetermined vehicle movements. First, a library of potential motion

segments is built; then they are sequenced to find the path that minimizes the cost objective. This process has been used for both 2D and 3D motion planning.[1-6]

Several methods involve the use of Voroni polygons. This consists of dividing the potential flight space into a graph where the vertices represent a specific position and orientation of the vehicle. Costs of the path between two vortices are then determined via the vehicle dynamics and cost function. First a suboptimal path is found by searching a graph based on Voroni polygons, and then the path is improved through a variety of techniques, including cubic splines and nonlinear ordinary differential equations.[7-12]

Some researchers have examined other methods of graphically determining minimum paths between two points. First a set of flyable paths is determined by combining certain maneuvers into a flight path. These paths were then examined to find the one with the lowest cost. Two different basic path scenarios are generally used. One consists of flight paths of the form circular arc – straight line – circular arc.[13] Another considers paths that use three circular arc maneuvers.[14]

A large number of the analytical techniques used for optimal trajectory generation involve a direct solving method of nonlinear programming. This consists of solving the set of Karush–Kuhn–Tucker equations, instead of the Euler-Lagrange equations from classical optimal control.[15] One method is to first discretize the differential and algebraic constraints using a collocation method with the state variables approximated as polynomials and the control variables approximated as piecewise linear functions. This results in a purely algebraic problem that can be directly solved.[16-18] Another technique involves using either a Gauss or Legendre pseudospectral method.[19-22]

There are a wide variety of other analytical techniques that have been employed to determine optimal, or near-optimal, trajectories. One method involves using singular perturbation techniques to create a two-point boundary value problem.[23] Another involves using a probabilistic map – which is defined as the risk of exposure to threats as a function of position – to find an optimal path while avoiding threats.[24] A third uses a nonlinear trajectory generation algorithm that finds a trajectory parameterized by B-splines, the coefficients of which are then found to satisfy the optimization objectives and constraints.[25] In addition, neighboring optimal control is also used to find optimal trajectories.[26]

Several groups of researchers use genetic algorithms to solve optimal trajectory problems, for both single and multiple vehicles. One way is to have a set number of defined maneuvers and standard small-formation tactics, then use the genetic algorithm to determine how they can be integrated to optimize the problem.[27] Another possibility is to first convert the optimization problem to a nonlinear programming problem; then use a real-coded genetic algorithm to solve it.[28] A third method is to use the genetic algorithms to find an optimal set of waypoints defining the trajectory, then connect the points with flyable curves.[29] Others use a genetic algorithm to find a near optimal solution by searching a population of possible vehicle path portions.[30-33]

In the early 1990s, P. K. Menon and Eulgon Kim researched methods of optimal trajectory path planning for terrain following and terrain masking flight. This research produced a reduced order formulation based on a constant velocity approach.[34-35] Ping Lu and Bion Pierson then used an inverse dynamics approach to solve a terrain following problem that included a more realistic varying velocity.[36] In 2005, Tobies Ries conducted

similar research using a graphical optimization program called GESOP. This program allows the inclusion of a six degree-of-freedom UAV model with dynamics.[37]

This research expands on the work done by Menon and Kim. It was decided to continue investigating using a reduced order formulation in order to exploit the benefits of analytical methods of solving the optimal path planning problem before it became necessary to use any numerical methods. In most numerical methods, the time step for the discretization phase usually must be very small to avoid loss of information. This leads to very long solving times. Also, the graphical methods of solving this type of problem rarely lead to an optimal solution. The components of the research presented here include

- Inclusion of wind effects, moving target and moving threats to pseudo-3D constant velocity formulation.
- Examination of interior point constraints.
- Expansion of pseudo-3D equations of motion to full 3D equations of motion.
- Addition of velocity as a state to create a 3D varying velocity formulation.
- Expansion of pseudo-3D and 3D equations of motion to handle cooperative path planning for n-vehicles.
- Derived second order variation conditions for each formulation and used these conditions to assist in finding the optimal initial conditions.

Two pseudo-3D formulations are presented: one using local tangent plane equations of motion and one using simplified equations of motion. These equations of motion are used both with determining the trajectories for a single aircraft as well as for multiple vehicles. Figure 1 depicts a sample terrain profile with the X-Y-H coordinate

system and a local x_l-y_l-z_l coordinate system. The moving local coordinate system has its origin on the terrain surface at a current x, y position with the x_l-y_l plane being the tangent plane.

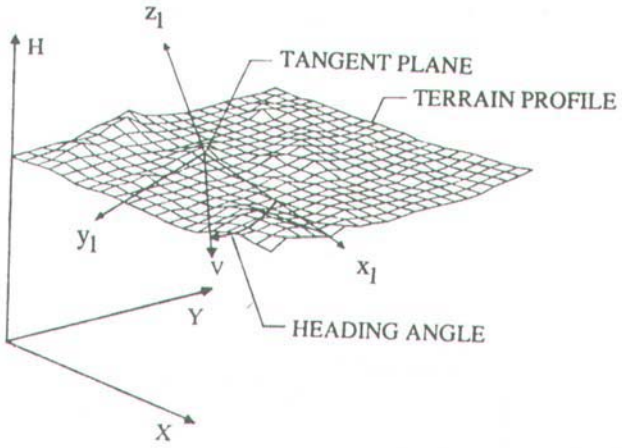

Figure 1.1: Relationship between Inertial Frame and Local Tangent Plane.

The local tangent plane formulation incorporates the constraint that the vehicle flies tangentially to the local terrain directly into the equations of motion and can be written as

$$\dot{x} = \frac{V\cos\psi}{A_1} + \frac{Vf_x f_y \sin\psi}{A_1 A_2} \tag{1.1}$$

$$\dot{y} = \frac{-VA_1 \sin\psi}{A_2} \tag{1.2}$$

The simplified equations of motion are an approximation written in the local level frame and neglect the effects of the terrain slope in the position kinematics.

$$\dot{x} = V\cos\psi \tag{1.3}$$

$$\dot{y} = V\sin\psi \tag{1.4}$$

Chapters 2 to 6 investigate the implementation of the optimal path planning with a single vehicle. Chapter 2 formulates the problem using both the simplified and local tangent plane equations of motion and includes the effects of adding a moving target, wind effects and moving threats. Chapter 3 details the results gathered from using these methods. Chapter 4 repeats this problem using 3D equations of motion, both with a constant velocity and with a varying velocity. Chapter 5 contains the results for these formulations. Chapter 6 compares the results from Chapters 2-5 and then investigates implementing the analytical results from these methods in a full six degree-of-freedom flight simulator. In addition, results are compared to those found using GESOP.

Chapters 7 through 10 deal with implementing this process using multiple vehicles. In Chapter 7, the necessary equations are derived for n-vehicles using the simplified and local tangent plane equations of motion. The corresponding results for these formulations are depicted in Chapter 8. In Chapter 9, the n-vehicle formulation is expanded to use the 3D constant velocity equations of motion and those results are in Chapter 10.

Details on the methods used to solve these problems are discussed in Chapter 11 while conclusions and future research are presented in Chapter 12. The second variation analysis of these problems is considered in Appendix A. Here the Legendre-Clebsch necessary condition and the Jacobi condtion – which are needed to ensure at least a weak local minimum – as well as the Weierstrass test – which is needed to ensure a strong local minimum – are examined. For the Legendre-Clebsch condition and the Weierstrass test, it is found that certain inequalities must be satisfied at all time. These specific

inequalities are examined throughout the thesis for each formulation. For the Jacobi condition, it is found that a matrix created by perturbing the optimal solution must be fully rank at all time. All the results presented in this thesis meet this requirement, and this condition is not discussed explicitly for the different sections Last, various necessary mathematical proofs are contained in Appendix B.

CHAPTER 2

SINGLE VEHICLE FORMULATION

2.1 Local Tangent Plane Equations of Motion

In this formulation, the equations of motion were described in equations (1.1) and (1.2) and are restated here.

$$\dot{x} = \frac{V\cos\psi}{A_1} + \frac{Vf_x f_y \sin\psi}{A_1 A_2} + u(x,y) \tag{2.1}$$

$$\dot{y} = \frac{-VA_1 \sin\psi}{A_2} + v(x,y) \tag{2.2}$$

These equations embody the constraint that at all times the vehicle flies tangentially to the local terrain. Here, x and y are the north and east components, respectively. V is the total aircraft velocity while u and v are the wind velocities in the x and y-directions, respectively. The heading of the vehicle is represented by ψ -- the heading angle measured with respect to the local tangent plane. Also, f_x and f_y are the partial derivatives of the terrain profile. A_1 and A_2 are given by

$$A_1 = \sqrt{1 + f_x^2} \tag{2.3}$$

$$A_2 = \sqrt{1 + f_x^2 + f_y^2} \tag{2.4}$$

The cost function for this problem can be seen in the following equation.

$$J = \int_0^{t_f} \left[(1-K) + Kg(x,y,t)\right]dt \tag{2.5}$$

In this equation, the combined threat and terrain function, $g(x,y,t)$, is given as a function of time as well as the position and can be defined as follows.

$$g(x,y,t) = f(x,y) + f_T(x,y,t) \tag{2.6}$$

Here, $f(x,y)$ is the function for the terrain profile and $f_T(x,y,t)$ is the function denoting the moving threat. The weighting parameter, K, can vary between 0 and 1 and determines the relative importance of time and terrain masking/threat avoidance used in the optimization. When $K = 0$, the equations are optimized with respect to time. When K is set to 1, the path is optimized with respect to the threats and the terrain. The Hamiltonian equation can then be given as

$$H = A_4 + \lambda_x \left[\frac{V\cos\psi}{A_1} + \frac{Vf_x f_y \sin\psi}{A_1 A_2} + u \right] + \lambda_y \left[\frac{-VA_1 \sin\psi}{A_2} + v \right] \tag{2.7}$$

In this expression, λ_x and λ_y are the costate equations and A_4 can be seen in the following equation.

$$A_4 = 1 - K + Kg(x,y,t) \tag{2.8}$$

The moving threat and target equations of motion are, respectively:

$$\begin{aligned} \dot{x}_T &= V_T \cos\psi_T \\ \dot{y}_T &= V_T \sin\psi_T \end{aligned} \tag{2.9}$$

$$\begin{aligned} \dot{x}_{Tg} &= V_{Tg} \cos\psi_{Tg} \\ \dot{y}_{Tg} &= V_{Tg} \sin\psi_{Tg} \end{aligned} \tag{2.10}$$

In each expression, it is assumed that the respective velocity and heading angle are known at all times. The moving target then results in a new boundary condition.

$$\Psi(t_f) = \left[\begin{matrix} x(t) - x_{Tg}(t) \\ y(t) - y_{Tg}(t) \end{matrix} \right]_{t=t_f} \tag{2.11}$$

In this expression, it can be seen that $\Psi(t_f)$ has an explicit dependence on the final time as a consequence of the fact that the target coordinates are assumed to satisfy equation (2.10). Therefore, for a free final time, the Hamiltonian equation satisfies

$$H(t_f) = -\lambda^T \left[\frac{\partial \Psi}{\partial t} \right]_{t=t_f} = V_{Tg} \left[\lambda_x \cos\psi_{Tg} + \lambda_y \sin\psi_{Tg} \right]_{t=t_f} \tag{2.12}$$

Due to the moving threat, the Hamiltonian equation, (2.7), is explicitly dependent on time. Given this, the optimality condition for a solution along an extremal arc shows that

$$\dot{H} = \frac{\partial H}{\partial t} = K g_t \tag{2.13}$$

where g_t denotes the partial derivative of the penalty function with respect to time. Assuming that the threat is constant when expressed in a coordinate system that is attached to the moving threat, then

$$g(x, y, t) = g[x - x_T(t), y - y_T(t)] \tag{2.14}$$

with the threat coordinates satisfying (2.9). Thus

$$\dot{H} = -KV_T \left(g_x \cos\psi_T + g_y \sin\psi_T \right) \tag{2.15}$$

Because the final time is free, the boundary condition for this expression is defined in (2.12).

The optimality condition for this problem is defined as

$$H_\psi = 0 \tag{2.16}$$

Evaluating this expression results in the following relationship

$$\lambda_y = \lambda_x \left[\frac{V f_x f_y \cos\psi}{A_1 A_2} - \frac{V \sin\psi}{A_1} \right] \frac{A_2}{V A_1 \cos\psi} \tag{2.17}$$

Equation (2.17) can then be substituted into the Hamiltonian equation, (2.7), to determine equations defining the two costates, λ_x and λ_y as follows.

$$\lambda_x = \frac{-(A_4 - H) A_1^2 \cos\psi}{Den} \tag{2.18}$$

$$\lambda_y = \frac{(A_4 - H)A_2 \sin\psi - (A_4 - H) f_x f_y \cos\psi}{Den} \tag{2.19}$$

where

$$Den = VA_1 + A_1^2 u \cos\psi + f_x f_y v \cos\psi - A_2 v \sin\psi \tag{2.20}$$

These new expressions for the costates can then be inserted into (2.12) to result in a new boundary condition for the Hamiltonian at the final time.

$$H(t_f) = \left[\frac{V_{Tg} A_4 \left(A_1^2 \cos\psi \cos\psi_{Tg} + f_x f_y \cos\psi \sin\psi_{Tg} - A_2 \sin\psi \sin\psi_{Tg} \right)}{V_{Tg} \left(A_1^2 \cos\psi \cos\psi_{Tg} + f_x f_y \cos\psi \sin\psi_{Tg} - A_2 \sin\psi \sin\psi_{Tg} \right) - Den} \right]_{t=t_f} \tag{2.21}$$

Differential equations for the costates can be found using

$$\begin{aligned} \dot{\lambda}_x &= -H_x \\ \dot{\lambda}_y &= -H_y \end{aligned} \tag{2.22}$$

This yields

$$\dot{\lambda}_x = -Kg_x - \lambda_x \left[\frac{D_2 \cos\psi + D_3 \sin\psi + D_1 u_x}{D_1} \right] - \lambda_y \left[\frac{D_4 \sin\psi + D_1 v_x}{D_1} \right] \tag{2.23}$$

$$\dot{\lambda}_y = -Kg_y - \lambda_x \left[\frac{D_5 \cos\psi + D_6 \sin\psi + D_1 u_y}{D_1} \right] - \lambda_y \left[\frac{D_7 \sin\psi + D_1 v_y}{D_1} \right] \tag{2.24}$$

where

$$D_1 = A_1^3 A_2^3 \tag{2.25}$$

$$D_2 = -Vf_x f_{xx} A_2^3 \tag{2.26}$$

$$D_3 = VA_1^2 A_2^2 B_2 - VA_2^2 f_x^2 f_y f_{xx} - VA_1^2 B_1 f_x f_y \tag{2.27}$$

$$D_4 = VA_1^4 B_1 - VA_1^2 A_2^2 f_x f_{xx} \tag{2.28}$$

$$D_5 = -Vf_x f_{xy} A_2^3 \tag{2.29}$$

$$D_6 = VA_1^2 A_2^2 B_3 - VA_2^2 f_x^2 f_y f_{xy} - VA_1^2 B_4 f_x f_y \tag{2.30}$$

$$D_7 = VA_1^4 B_4 - VA_1^2 A_2^2 f_x f_{xy} \tag{2.31}$$

$$B_1 = f_x f_{xx} + f_y f_{xy} \tag{2.32}$$

$$B_2 = f_x f_{xy} + f_y f_{xx} \tag{2.33}$$

$$B_3 = f_x f_{yy} + f_y f_{xy} \tag{2.34}$$

$$B_4 = f_x f_{xy} + f_y f_{yy} \tag{2.35}$$

Next, the time derivative of either equation (2.18) or (2.19) is taken and set equal to its counterpart in equation (2.23) or (2.24). This expression can then be solved for the derivative of the heading angle such that

$$\dot{\psi} = \frac{T_1 + T_2 u + T_3 v + T_4 u_x + T_5 u_y + T_6 v_x + T_7 v_y}{T_8} \tag{2.36}$$

where

$$T_1 = -KVS_1 + V(A_4 - H)S_2 \tag{2.37}$$

$$T_2 = -KS_3 + (A_4 - H)S_4 \tag{2.38}$$

$$T_3 = KS_5 + (A_4 - H)S_6 \tag{2.39}$$

$$T_4 = (A_4 - H)S_7 \tag{2.40}$$

$$T_5 = (A_4 - H)S_8 \tag{2.41}$$

$$T_6 = (A_4 - H)S_9 \tag{2.42}$$

$$T_7 = (A_4 - H)S_{10} \tag{2.43}$$

$$T_8 = (A_4 - H)A_1^3 A_2^2 \tag{2.44}$$

$$S_1 = A_1^2 A_2 \left[A_2 g_x \sin\psi + \left(g_y + f_x^2 g_y - g_x f_x f_y\right)\cos\psi\right] \tag{2.45}$$

$$S_2 = \left(f_x f_y^2 f_{xx} - A_1^2 f_y f_{xy}\right)\sin\psi + A_2 f_y f_{xx}\cos\psi \tag{2.46}$$

$$S_3 = A_1^3 A_2 \left[A_2 g_x \sin\psi + \left(g_y + f_x^2 g_y - g_x f_x f_y \right) \cos\psi \right] \cos\psi \tag{2.47}$$

$$\begin{aligned} S_4 &= A_1 A_2 \left(A_1^2 f_x f_{xy} - f_x^2 f_y f_{xx} + f_y f_{xx} \right) \cos^2\psi + \\ &+ A_1 \left(A_1^2 f_x f_{xx} - A_1^2 f_y f_{xy} + 2 f_x f_y^2 f_{xx} \right) \sin\psi \cos\psi \end{aligned} \tag{2.48}$$

$$\begin{aligned} S_5 &= A_1 A_2^2 \left(A_1^2 g_y - 2 g_x f_x f_y \right) \sin\psi \cos\psi + \\ &+ A_1 A_2^3 g_x \sin^2\psi + A_1 A_2 \left(g_x f_x^2 f_y^2 - A_1^2 f_x g_y f_y \right) \cos^2\psi \end{aligned} \tag{2.49}$$

$$\begin{aligned} S_6 &= A_1 A_2 \left(f_y f_{xy} - f_x^2 f_y f_{xy} + A_1^2 f_x f_{yy} \right) \cos^2\psi + \\ &+ A_1 \left(2 f_x f_y^2 f_{xy} + A_1^2 f_x f_{xy} - A_1^2 f_y f_{yy} \right) \sin\psi \cos\psi \end{aligned} \tag{2.50}$$

$$S_7 = A_1^3 A_2 \left(A_2 \sin\psi - f_x f_y \cos\psi \right) \cos\psi \tag{2.51}$$

$$S_8 = A_1^5 A_2 \cos^2\psi \tag{2.52}$$

$$S_9 = A_1 A_2^2 \left(2 f_x f_y \sin\psi \cos\psi - A_2 \right) + A_1 A_2 \left(A_2^2 - f_x^2 f_y^2 \right) \cos^2\psi \tag{2.53}$$

$$S_{10} = A_1^3 A_2 \left(f_x f_y \cos\psi - A_2 \sin\psi \right) \cos\psi \tag{2.54}$$

This solution consists of four differential equations -- x, y, H and ψ -- and requires two initial conditions to be found -- H and ψ. The final value of the Hamiltonian is known, via equation (2.21). The solution is reached when the final values of the Hamiltonian and position are met and the cost is minimized. When there are no moving threats, the Hamiltonian is constant in value – so there are only three differential equations – and the final value is still known. When there is no moving target, the final value of the Hamiltonian is zero.

2.1.1 Legendre-Clebsch Necessary Condition

The Hamiltonian equation for the local tangent plane equations of motion is

$$H = A_4 + \lambda_x \left[\frac{V\cos\psi}{A_1} + \frac{Vf_x f_y \sin\psi}{A_1 A_2} \right] + \lambda_y \left[\frac{-VA_1 \sin\psi}{A_2} \right] \tag{2.55}$$

and the algebraic equations for the costates are

$$\begin{aligned} \lambda_x &= \frac{-(A_4 - H)A_1 \cos\psi}{V} \\ \lambda_y &= \frac{(A_4 - H)(A_2 \sin\psi - f_x f_y \cos\psi)}{VA_1} \end{aligned} \tag{2.56}$$

Since there is only one control, the second partial derivative of the Hamiltonian with respect to the heading angle is a scalar value and is represented by

$$H_{uu} = \lambda_x \left[\frac{-V\cos\psi}{A_1} - \frac{Vf_x f_y \sin\psi}{A_1 A_2} \right] + \lambda_y \left[\frac{VA_1 \sin\psi}{A_2} \right] \tag{2.57}$$

Substituting in the equations for the optimal costates will result in

$$H_{uu} = (A_4 - H) \geq 0 \tag{2.58}$$

This condition must always be satisfied.

2.1.2 Weierstrass Test

The variational Hamiltonian can be found by substituting the costate equations from (2.56) for the optimal path into the Hamiltonian equation from (2.55) evaluated for any path. This yields

$$\begin{aligned} H(\psi) = A_4 + &\left[\frac{-(A_4 - H)A_1 \cos\psi^o}{V} \right] \left[\frac{V\cos\psi}{A_1} + \frac{Vf_x f_y \sin\psi}{A_1 A_2} \right] + \\ &\left[\frac{(A_4 - H)(A_2 \sin\psi - f_x f_y \cos\psi^o)}{VA_1} \right] \left[\frac{-VA_1 \sin\psi}{A_2} \right] \end{aligned} \tag{2.59}$$

This can be simplified to

$$H(\psi) = (A_4 - H)\left[1 - \cos(\psi^o - \psi)\right] \geq 0 \tag{2.60}$$

which will always be satisfied if equation (2.58) is satisfied.

2.2 Simplified Equations of Motion

The equations of motion used in the simplified formulation are described earlier in equations (1.3) and (1.4) and are restated here

$$\dot{x} = V\cos\psi + u(x, y) \tag{2.61}$$

$$\dot{y} = V\sin\psi + v(x, y) \tag{2.62}$$

These equations are written in the local level plane and neglect the effects of the terrain slope. The cost equation for this case is the same as earlier and can be found in equation (2.5). The corresponding Hamiltonian equation is therefore

$$H = A_4 + \lambda_x\left[V\cos\psi + u\right] + \lambda_y\left[V\sin\psi + v\right] \tag{2.63}$$

The equations governing the moving target and moving threat can be seen above in equations (2.9) and (2.10).

Evaluating the optimality condition stated in equation (2.16) for this formulation results in the expression

$$\lambda_y = \lambda_x \frac{\sin\psi}{\cos\psi} \tag{2.64}$$

Substituting this into the Hamiltonian equation results in the following costate equations

$$\lambda_x = \frac{-\left(A_4 - H\right)\cos\psi}{V + u\cos\psi + v\sin\psi} \tag{2.65}$$

$$\lambda_y = \frac{-\left(A_4 - H\right)\sin\psi}{V + u\cos\psi + v\sin\psi} \tag{2.66}$$

Therefore, the Hamiltonian evaluated at the final time will be

$$H(t_f) = \left[\frac{V_{Tg} A_4 \cos(\psi - \psi_{Tg})}{V_{Tg} \cos(\psi - \psi_{Tg}) - (V + u\cos\psi + v\sin\psi)} \right]_{t=t_f} \tag{2.67}$$

The costate differential equations can then be found to be

$$\dot{\lambda}_x = -H_x = -Kg_x - \lambda_x u_x - \lambda_y v_x \tag{2.68}$$

$$\dot{\lambda}_y = -H_y = -Kg_y - \lambda_x u_y - \lambda_y v_y \tag{2.69}$$

As before, the time derivative of (2.65) or (2.66) is found and equated to either (2.68) or (2.69). This expression can then be rearranged to result in the following heading differential equation.

$$\dot{\psi} = \frac{R_1 + R_2 u + R_3 v + R_4 (u_x - v_y) + R_5 u_y + R_6 v_x}{R_7} \tag{2.70}$$

with

$$R_1 = KV(g_y \cos\psi - g_x \sin\psi) \tag{2.71}$$

$$R_2 = K(g_y \cos\psi - g_x \sin\psi)\cos\psi \tag{2.72}$$

$$R_3 = K(g_y \cos\psi - g_x \sin\psi)\sin\psi \tag{2.73}$$

$$R_4 = (A_4 - H)\sin\psi\cos\psi \tag{2.74}$$

$$R_5 = -(A_4 - H)\cos^2\psi \tag{2.75}$$

$$R_6 = (A_4 - H)\sin^2\psi \tag{2.76}$$

$$R_7 = (A_4 - H) \tag{2.77}$$

Again, the inclusion of a moving target and moving threat results in a system of four differential equations with two initial parameters to be found.

2.2.1 Legendre-Clebsch Necessary Condition

The Hamiltonian equation for the simplified equations of motion is

$$H = A_4 + \lambda_x [V\cos\psi] + \lambda_y [V\sin\psi] \tag{2.78}$$

and the costate equations are

$$\begin{aligned} \lambda_x &= \frac{-(A_4 - H)\cos\psi}{V} \\ \lambda_y &= \frac{-(A_4 - H)\sin\psi}{V} \end{aligned} \tag{2.79}$$

The partial derivative of the Hamiltonian equation with respect to the heading angle is

$$H_{uu} = (A_4 - H) \geq 0 \tag{2.80}$$

whish must always be satisfied.

2.2.2 Weierstrass Test

Using the Hamiltonian equation in (2.78) and the costate equations in (2.79), the variational Hamiltonian can be written as

$$H = A_4 + \left[\frac{-(A_4 - H)\cos\psi^o}{V}\right][V\cos\psi] + \left[\frac{-(A_4 - H)\sin\psi^o}{V}\right][V\sin\psi] \tag{2.81}$$

This equation can be reduced to

$$H(\psi) = (A_4 - H)[1 - \cos(\psi^o - \psi)] \geq 0 \tag{2.82}$$

which will always be satisfied if equation (2.80) is satisfied.

2.3 Waypoints

One useful problem variation that can also be investigated is the implementation of interior point constraints during the flight.[38-39] For this problem, the constraints will be

implemented in the form of waypoints where a specific position is required in the middle of the flight. There can be n-number of waypoints during this flight, such that each waypoint – with a given x and y position – is reached at an unspecified time, t_i, in a specified order before ending at the specified final position.

In this type of problem, there are certain constraints on the costates and Hamiltonian that must be fulfilled at the interior points. They include

$$\begin{aligned} \lambda_x(t_i^+) &= \lambda_x(t_i^-) + \upsilon_{1i} \\ \lambda_y(t_i^+) &= \lambda_y(t_i^-) + \upsilon_{2i} \\ H(t_i^+) &= H(t_i^-) = 0 \end{aligned} \tag{2.83}$$

This implies that the value of each of the costates will jump at each waypoint while the Hamiltonian will remain constant. Because of that, the heading angle will also jump at each waypoint. This will result in a trajectory such as that seen in Figure 2.1. In this

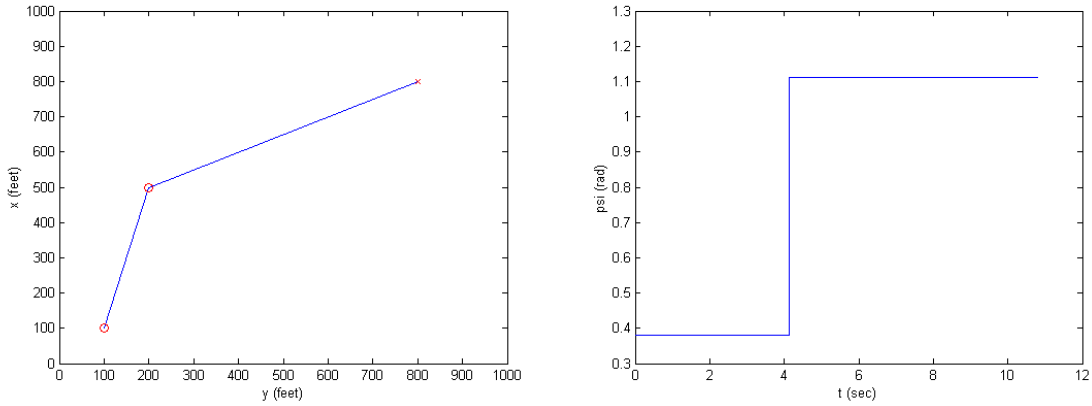

Figure 2.1: Solution with one waypoint.

example, flight over a flat plane with one waypoint is considered. Because all the terrain partial derivatives are zero, the local tangent plane equations of motion will reduce to the simplified equations of motion. In addition, both the costates will be at a constant value

at all times with a jump at the time of reaching the waypoint. This results in the heading angle also being a constant value with a jump at the waypoint. Having a jump in the heading angle will create an optimal path that is not flyable. Therefore, the equations of motion for this section will be modified to ensure a smooth trajectory.

The equations of motion for this section will include the equations used earlier with the addition of ψ as an additional state. This results in equations of motion of

$$\begin{aligned} \dot{x} &= \frac{V\cos\psi}{A_1} + \frac{Vf_x f_y \sin\psi}{A_1 A_2} \\ \dot{y} &= \frac{-VA_1 \sin\psi}{A_2} \\ \dot{\psi} &= u \end{aligned} \tag{2.84}$$

for the local tangent plane or

$$\begin{aligned} \dot{x} &= V\cos\psi \\ \dot{y} &= V\sin\psi \\ \dot{\psi} &= u \end{aligned} \tag{2.85}$$

for the simplified equations of motion. In these equations, u designates the control variable for the system. The new cost equation is

$$J = \int_0^{t_f} \left\{ (1 - K + Kf) + Wu^2 \right\} dt = \int_0^{t_f} \left\{ A_4 + Wu^2 \right\} dt \tag{2.86}$$

which is the same as above with the inclusion of the control in the cost multiplied by a weighing factor.

The Hamiltonian for this problem is now

$$H = A_4 + Wu^2 + \lambda_x \dot{x} + \lambda_y \dot{y} + \lambda_\psi u \tag{2.87}$$

For both formulations, evaluating the optimality equation results in

$$H_u = 0 = 2Wu + \lambda_\psi \tag{2.88}$$

This yields the following equation for the control

$$u = \dot{\psi} = \frac{-\lambda_{\psi}}{2W} \tag{2.89}$$

At each interior point, the following conditions on the costates and the Hamiltonian must be met.

$$\begin{aligned} \lambda_x(t_i^+) &= \lambda_x(t_i^-) + \upsilon_{1i} \\ \lambda_y(t_i^+) &= \lambda_y(t_i^-) + \upsilon_{2i} \\ \lambda_{\psi}(t_i^+) &= \lambda_{\psi}(t_i^-) \\ H(t_i^+) &= H(t_i^-) = 0 \end{aligned} \tag{2.90}$$

Using these conditions from (2.90) as well as equations (2.87) and (2.86), an independent equation for λ_y is found as follows.

$$\lambda_y = \frac{Wu^2 - A_4 - \lambda_x \dot{x}}{\dot{y}} \tag{2.91}$$

Next the differential equations for the other two costates can be determined using

$$\begin{aligned} \dot{\lambda}_x &= -H_x \\ \dot{\lambda}_{\psi} &= -H_{\psi} \end{aligned} \tag{2.92}$$

This yields

$$\begin{aligned} \dot{\lambda}_x &= -Kf_x - \lambda_x \left[\frac{D_2 \cos\psi + D_3 \sin\psi}{D_1} \right] - \lambda_y \left[\frac{D_4 \sin\psi}{D_1} \right] \\ \dot{\lambda}_{\psi} &= \lambda_x \left[\frac{V \sin\psi}{A_1} - \frac{Vf_x f_y \cos\psi}{A_1 A_2} \right] + \lambda_y \left[\frac{VA_1 \cos\psi}{A_2} \right] \end{aligned} \tag{2.93}$$

for the local tangent plane equations of motion with D_1 through D_7 defined in equations (2.25) – (2.31). For the simplified equations of motion, the costate differential equations are

$$\begin{aligned}\dot{\lambda}_x &= -Kf_x \\ \dot{\lambda}_\psi &= \lambda_x V \sin\psi - \lambda_y V \cos\psi\end{aligned} \tag{2.94}$$

This results in a system of six differential equations. The initial conditions for the two costates – λ_x and λ_ψ – must be found as well as υ_l for each waypoint.

2.3.1 Legendre-Clebsch Necessary Condition

The Hamiltonian equation is stated in equation (2.87). The second partial derivative of it then

$$H_{uu} = 2W > 0 \tag{2.95}$$

which means that this condition is always satisfied.

2.3.2 Weierstrass Test

Using the Hamiltonian equations in (2.87) and the algebraic equations for λ_y and λ_ψ found in (2.91) and (2.89), the variational Hamiltonian can be found to be

$$H(u) = W\left(u - u^o\right)^2 \geq 0 \tag{2.96}$$

This shows that the Weierstrass test is always satisfied.

CHAPTER 3

SINGLE VEHICLE RESULTS

3.1 Terrain Data

Two general types of terrain models are used for the results throughout this thesis. The first is a generic terrain model used for the initial testing of the equations. This consists of variations of a flat plane with one or more constructed hills. The second consists of actual terrain data for a larger area. This allows the opportunity for the various equations to be tested in a more realistic manner.

A sample terrain of the generic model is shown in Figure 3.1. In this case a mostly flat plane with a single hill is used. This hill in this terrain is formulated using the exponential function

$$f = Ae^{-r^2/b} \tag{3.1}$$

where A is the amplitude, b is a scaling factor to adjust the width and r is the distance from any position to the center of the threat.

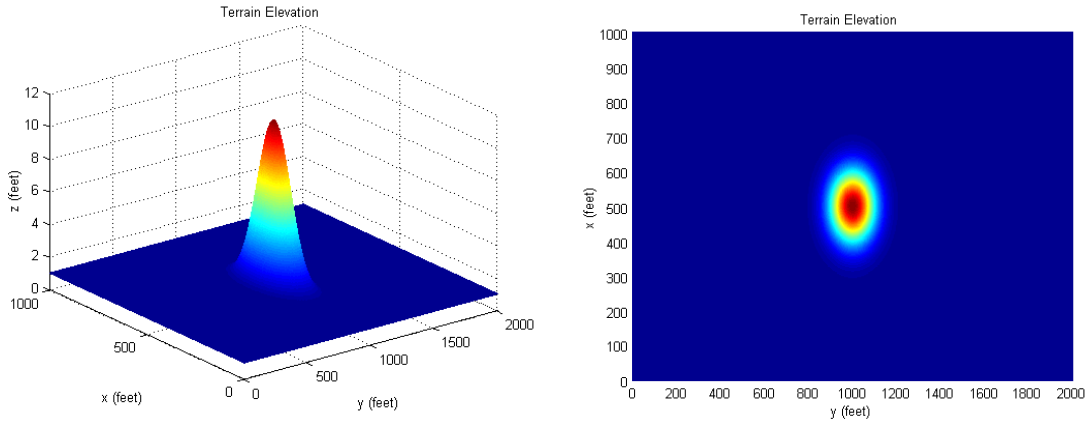

Figure 3.1: Terrain with threats formulated as an exponential function.

Real terrain data was acquired from the United States Geological Survey to incorporate into this model.[40] The data was found in tabular format relating the altitude to the locations longitude and latitude, with data points spaced approximately every 48 feet. This data was then converted to matrix form, from which it could then be used as $f(x,y)$. Because of the distance between the sampled altitude points in the matrix, the data was then smoothed to appear more continuous and to remove discontinuities in altitude. The gradients of this matrix, along both the x and y directions, were calculated numerically to form matrices representing $f_x(x,y)$ and $f_y(x,y)$. The gradients of these two matrices yielded matrices for $f_{xx}(x,y)$, $f_{yy}(x,y)$ and $f_{xy}(x,y)$.

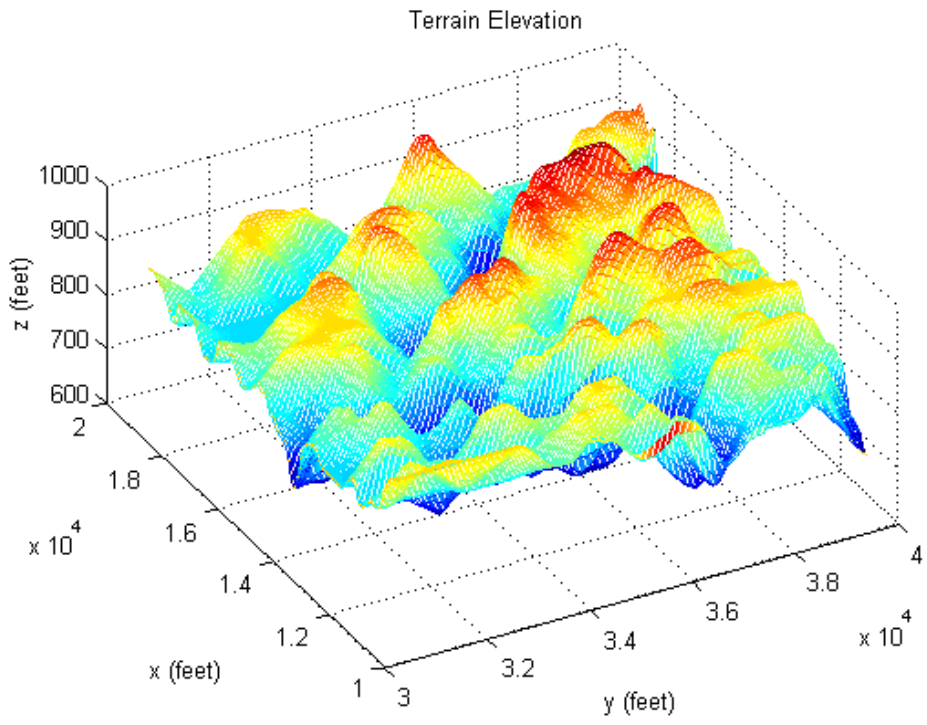

Figure 3.2: Terrain plot of an area near Columbus Ohio.

For this portion of the testing, it was decided to use a section of terrain near Columbus, Ohio. A profile of this terrain can be seen in Figure 3.2. In this graph, the x and y-axes depict the position coordinates, measured in feet, such that the x-axis point north and the y-axis points east. The altitude of the terrain is measured along the z-axis and is also given in feet. This plot depicts a square plot of land, with 10,000 feet to a side. The measurements along the x and y-axes are relative to a set origin for the terrain data collected; this plot is just one small portion of the database.

3.2 Wind Effects

First, the effects of a wind blowing were investigated. For this portion, the terrain model shown in Figure 3.1 was used with the single hill. For these flights, the initial and final points are (500,1800) and (500,200). Therefore the hill is directly between the two endpoints. With *K* set to 1, the optimal path found will curve around the hill. Since this is a symmetric field, there are two possible optimal paths when there is no wind – the path flying clockwise around the hill and the path flying counter-clockwise around the hill.

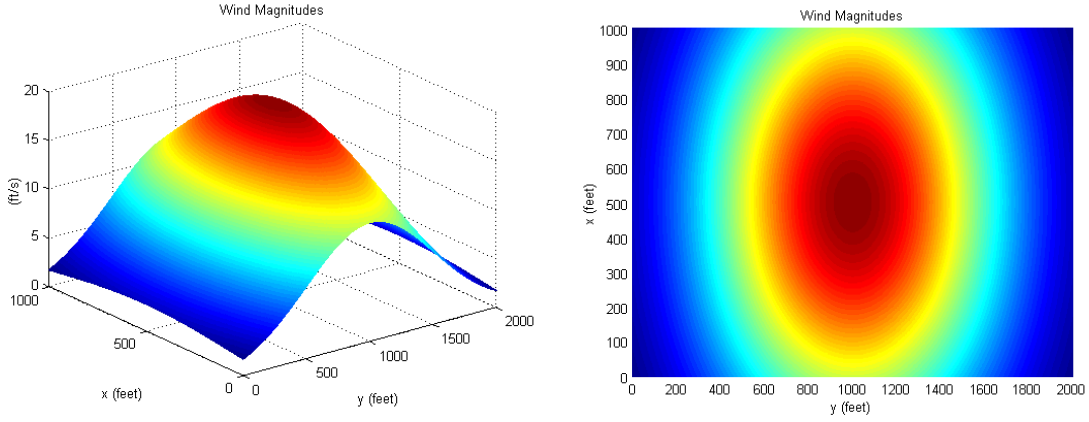

Figure 3.3: Wind magnitudes of a circulating pattern.

Here, a circulating wind pattern was introduced to the problem. In this case, the wind moved in a circular pattern centered at the top of the hill with a decreasing speed moving away from the hill. The magnitudes of the wind can be seen in Figure 3.3. This plot was generated using equation (3.1).

With the winds added, the optimal path is the option where the aircraft moves in the same direction as the circulating wind flow. Figure 3.4 shows the solutions found with the winds moving in a clockwise direction. The trajectory is on the left and the heading angle is plotted on the right. In Figure 3.5 the trajectory and heading angle for a flight with counter-clockwise wind are depicted.

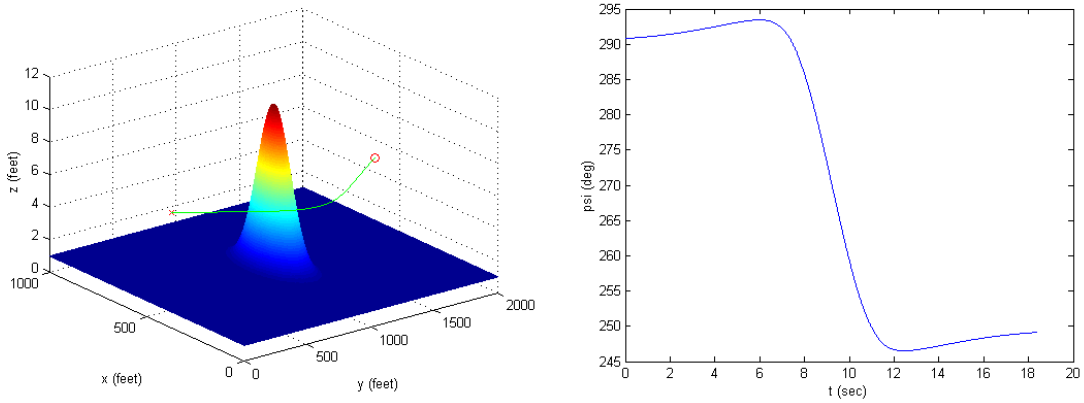

Figure 3.4: Trajectories for flights with clockwise wind.

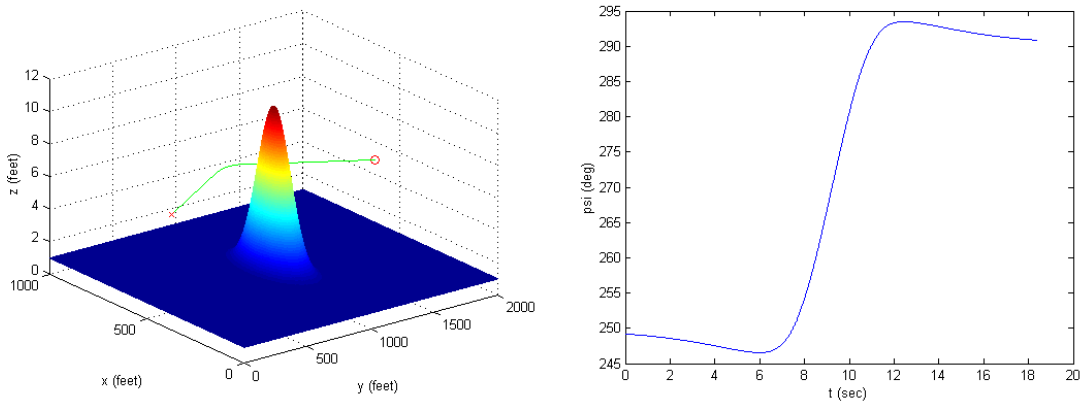

Figure 3.5: Trajectories for flights with counter-clockwise wind.

3.3 Moving Target and Threats

The simple terrain depicted above in Figure 3.1 consisting of a flat plain with a single hill was also used to test the moving threat and target formulation with K=1. The initial position is located at (500, 1800). The moving target begins at the point (900, 200) and travels south while the two threats begin at (600, 1400) and (600, 400), respectively, and travel in a south-easterly direction. For this situation, the results from the simplified equations of motion and the local tangent plane equations of motion are the same, so only one set of results are depicted.

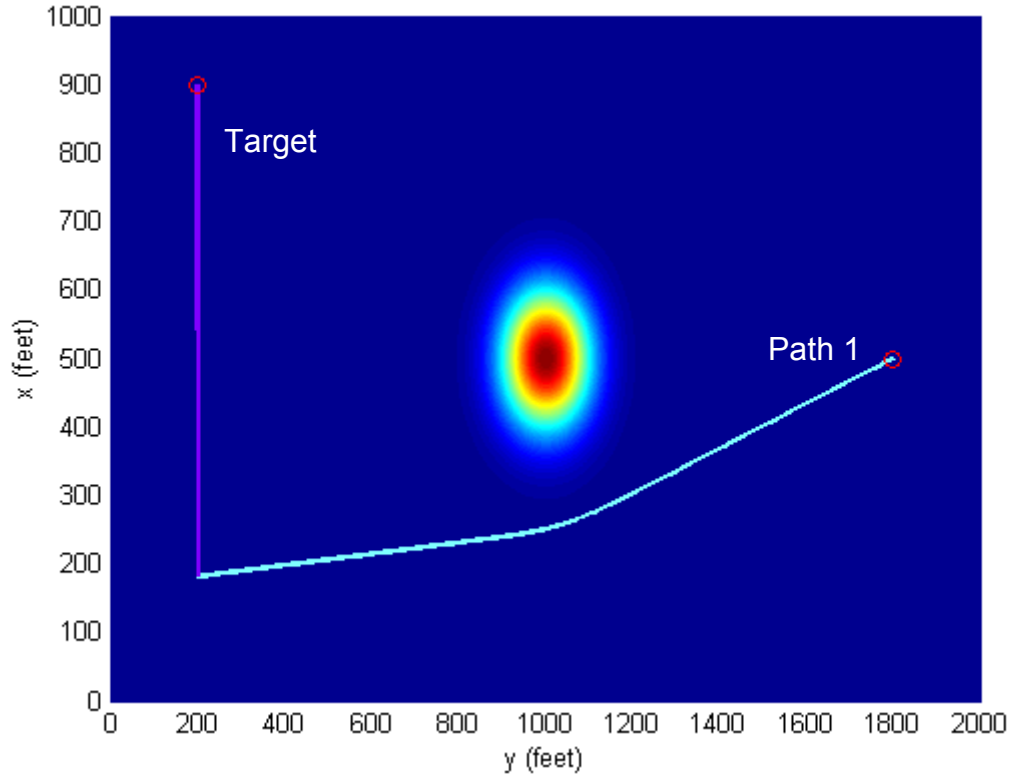

Figure 3.6: Paths generated with a moving target.

Figure 3.6 shows the first result. This is the case when there is a moving target and no threats are present. The target is represented by the purple line and the trajectory is depicted by the blue line.

The second case is depicted in Figure 3.7. In this scenario, the moving target is still present, but there is also one threat in the area to be avoided. The threat is shown as the red line in the plot. This figure also includes the result with the first case shown in Figure 3.6. Figure 3.8 shows the distances between the vehicle and the threat when path

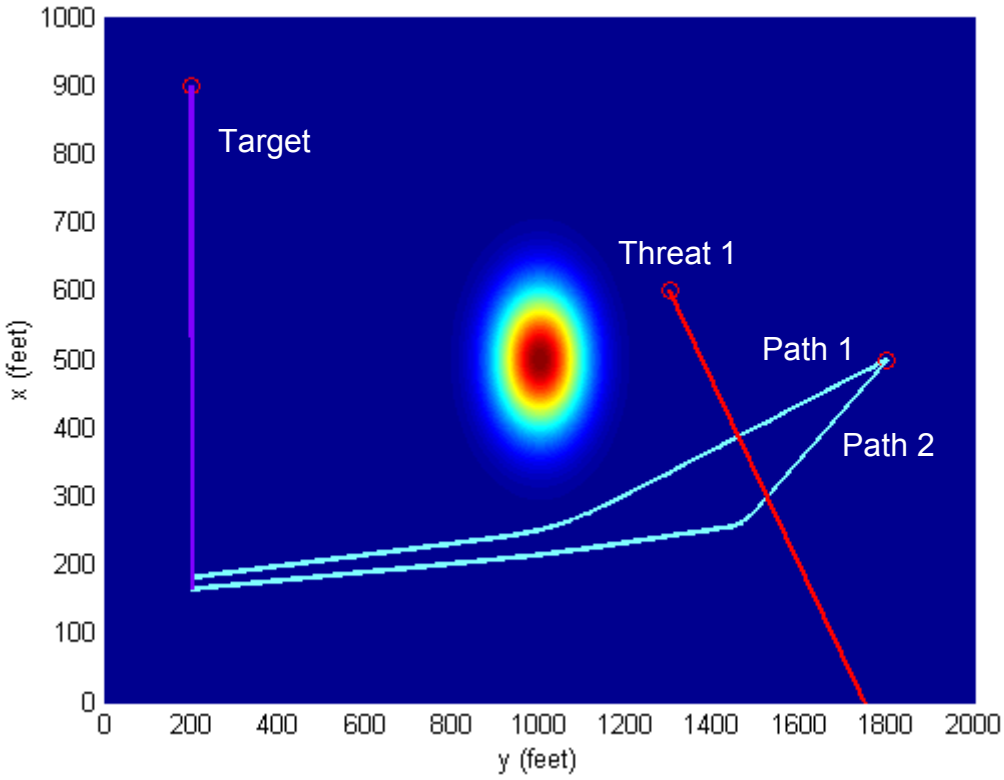

Figure 3.7: Paths generated with a moving target and one moving threat.

1 or path 2 are flown. It can be seen there that path 1 – the blue line – collides with the threat while path 2 – the red line – is about 100 feet away from the threat at its closest point. Thus it can be seen how path 2 changes to avoid the threat.

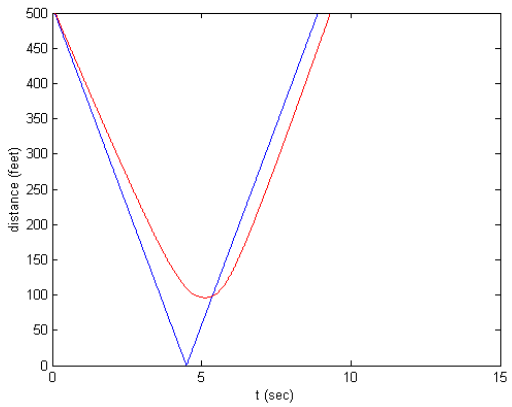

Figure 3.8: Distance between trajectories and threat 1.

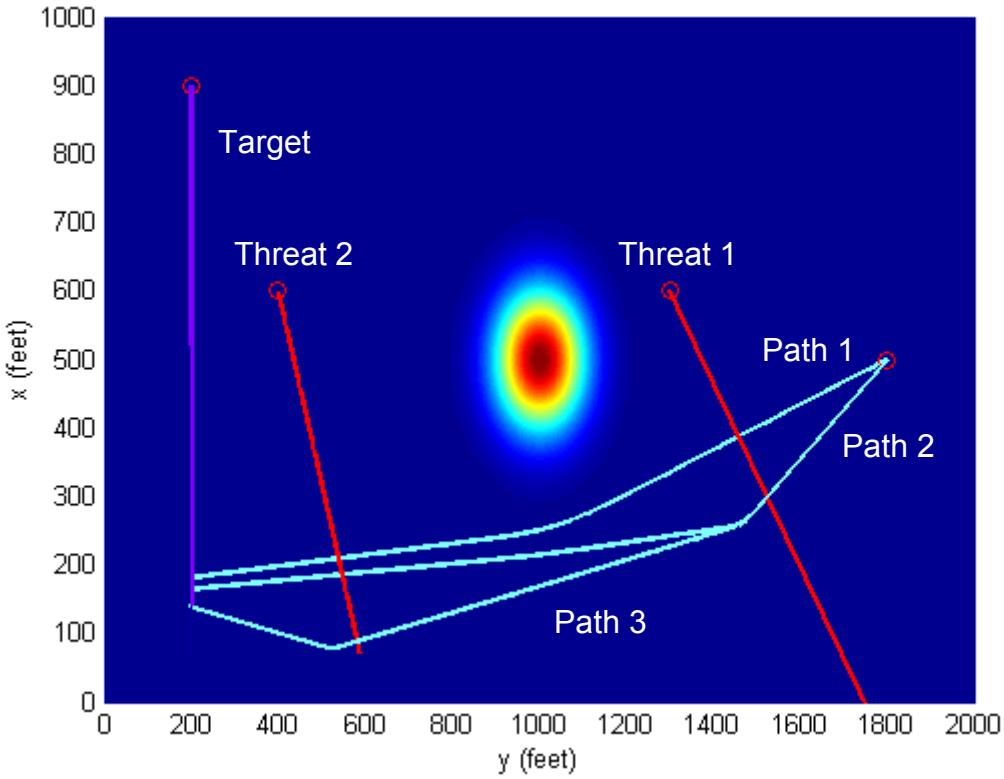

Figure 3.9: Path generated with a moving target and two moving threats.

Figure 3.9 shows the results from Figure 3.6 with the addition of a second threat and a new trajectory, path 3. The beginning of the flight is the same as path 2 until the

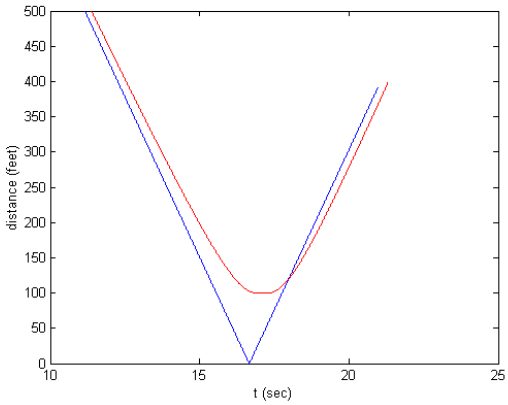

Figure 3.10: Distance between trajectories and threat 2.

first threat is avoided, then the new trajectory shifts to avoid the second threat. Figure 3.10 shows the distances between threat 2 and both path 2 and path 3. Here it can be seen that path 2 – shown with the blue line – collides with the threat while path 3 – depicted by the red line – stays a minimum of about 100 feet from the threat.

It was shown in the previous chapter that the Legendre-Clebsch and Weierstrass tests are satisfied if the following inequality is satisfied for all time.

$$A_4 - H > 0 \tag{3.2}$$

When considering the case of moving targets and moving threats, the Hamiltonian is no longer zero at all times, so this condition must be tested. Figure 3.11 shows the value for this function at all times for each of the three paths found in this section. It can be seen here that this function is always positive.

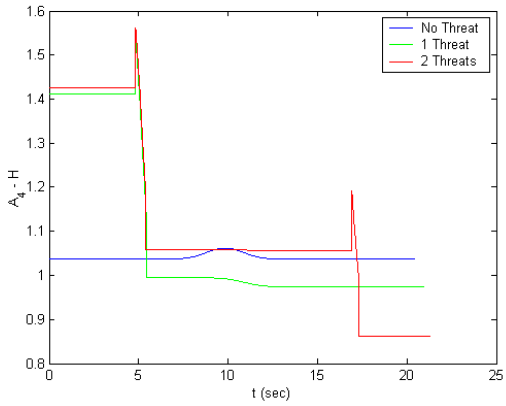

Figure 3.11: Weierstrass and Legendre-Clebsch test.

3.4 Pop-up Threats

The case of pop-up threats during flight was also investigated. In this case, the optimal path is in mid-flight when a stationary threat appears. A new trajectory must then be calculated. To test this, a flight through the Columbus terrain – shown in Figure 3.2 – was used, utilizing the constant velocity, local tangent plane equations of motion. In this case, a threat was added to the terrain as a single hill, as shown above in Figure 3.1, with a height of 300 feet above the level of the terrain at that point.

The results for this section can be seen in Figure 3.12. In this plot, the black dashed line depicts the original trajectory found; here it goes directly through the new threat. The three new trajectories are then shown as solid red lines. These depict the results when the threat is detected at three different times in the flight – at 7 seconds, 12 seconds and 16 seconds into the approximately 36-second flight. The plot on the right contains the plots of the heading angle for these four flights. The black line represents the heading angle for the nominal trajectory while the blue, red and green lines represent the heading angles for the trajectories when the threat is detected at 7, 12 and 16 seconds,

respectively. For each of these flights, the jump in the heading angle can be seen when the threat is detected and the new trajectory is calculated.

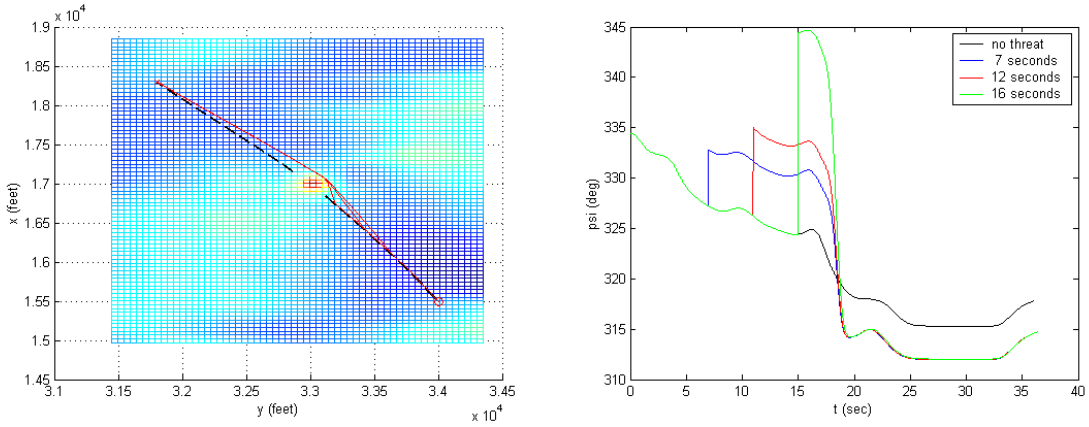

Figure 3.12: Trajectories found with a pop-up threat using local tangent plane equations of motion.

3.5 Waypoints

Two different cases of flying between waypoints are presented in this section. In each case, two waypoints are included in the flight scenarios. The first case concerns a flight over a flat plane. In this case, because there is a constant terrain, the local tangent plane equations of motion will reduce to the simplified equations of motion. The second case concerns flight over real terrain. For this case, the trajectory uses the local tangent plane equations of motion.

The first, shown in Figure 3.13, consists of a flight on a flat plain with two waypoints. The start position for the flight is at point (100, 100) with an initial heading of 0.44 radians; the first waypoint is at (600, 400); the second waypoint is at (900, 1900); the final position is (600, 1600). Here the initial position and the two waypoints are

marked with red circles while the final position is marked with a red x. The heading angle for this flight is depicted in the plot on the right.

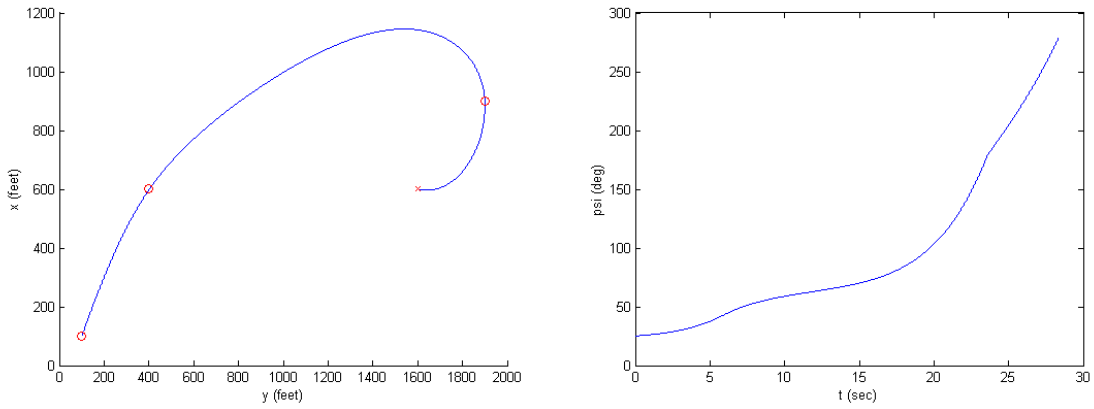

Figure 3.13: Trajectory on a flat plain with two waypoints.

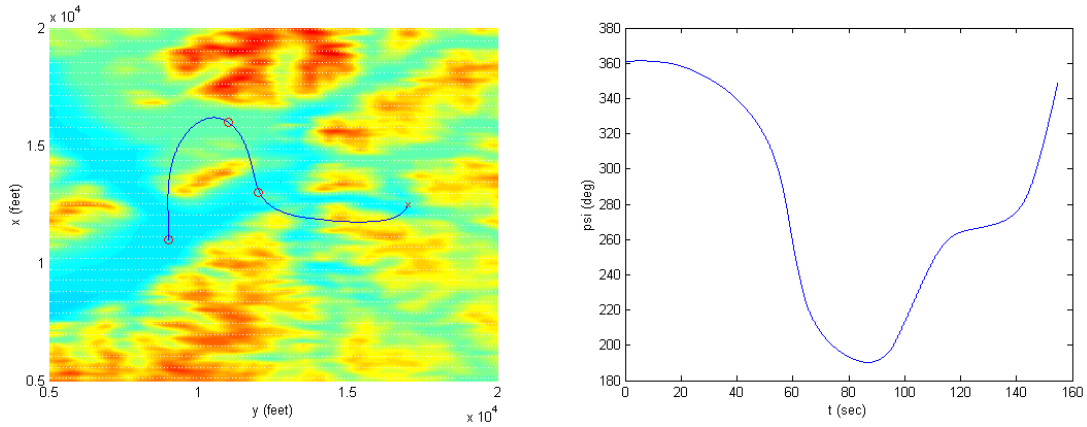

Figure 3.14: Trajectory on real terrain with two waypoints.

The second waypoint case involves flight over real terrain and is depicted in Figure 3.14. In this case, the initial position is (11000, 9000), the end position is (12500, 17000), and the initial heading angle is 6.3 radians. The two waypoints are located at (16000, 11000) and (13000, 12000). As before, the initial position and two waypoints are

marked with red circles while the final position is marked with a red x. Again, the heading angle for this flight is depicted in the plot on the right.

CHAPTER 4

SINGLE VEHICLE 3D FORMULATION

4.1 Constant Velocity

The 3D equations of motion used are

$$\dot{x} = V\cos\gamma\cos\psi \tag{4.1}$$

$$\dot{y} = V\cos\gamma\sin\psi \tag{4.2}$$

$$\dot{z} = V\sin\gamma \tag{4.3}$$

Here, V is the constant vehicle velocity, γ represents the flight path angle and ψ is the heading angle. The cost equation used for this problem is

$$J = \int_0^{t_f} \{C_1 + C_2\}dt = \int_0^{t_f} A_4 dt \tag{4.4}$$

$$C_1 = 1 - K + Kf(x, y) \tag{4.5}$$

$$C_2 = W[z - (f(x, y) + h_c)]^2 \tag{4.6}$$

This cost equation has two distinct parts. The first, and dominant part, is C_1 shown in (4.5). This part controls the importance of minimizing terrain masking versus minimizing flight time. The second part is C_2 as seen in (4.6). Here, h_c, the ground clearance, is a constant provided by the operator and represents the desired flight height above the terrain. This part is used to keep the flight path near the desired ground clearance throughout the flight. W is a weighing parameter supplied by the user.

The Hamiltonian is

$$H = A_4 + \lambda_x V\cos\gamma\cos\psi + \lambda_y V\cos\gamma\sin\psi + \lambda_z V\sin\gamma = 0 \tag{4.7}$$

The optimality conditions for this problem are now

$$\begin{aligned} H_\psi &= 0 \\ H_\gamma &= 0 \end{aligned} \tag{4.8}$$

Expressions for the three costates can then be found to be

$$\lambda_x = \frac{-A_4 \cos\gamma\cos\psi}{V} \tag{4.9}$$

$$\lambda_y = \frac{-A_4 \cos\gamma\sin\psi}{V} \tag{4.10}$$

$$\lambda_z = \frac{-A_4 \sin\gamma}{V} \tag{4.11}$$

The differential equations for the costates can then be found using the equations

$$\begin{aligned} \dot{\lambda}_x &= -H_x \\ \dot{\lambda}_y &= -H_y \\ \dot{\lambda}_z &= -H_z \end{aligned} \tag{4.12}$$

and can be shown to be

$$\dot{\lambda}_x = -Kf_x + 2Wf_xB_1 \tag{4.13}$$

$$\dot{\lambda}_y = -Kf_y + 2Wf_yB_1 \tag{4.14}$$

$$\dot{\lambda}_z = -2WB_1 \tag{4.15}$$

where

$$B_1 = z - \left(f + h_c\right) \tag{4.16}$$

Next, the time derivative of equation (4.11) can be taken and set equal to equation (4.15). This can be solved to find the following differential equation for γ.

$$\dot{\gamma} = \frac{2VWB_1\cos\gamma + V\sin\gamma\left(f_x\cos\psi + f_y\sin\psi\right)\left(2WB_1 - K\right)}{A_4} \tag{4.17}$$

Then the time derivative of either (4.9) or (4.10) can be calculated and set equal to the corresponding costate differential equations shown in (4.13) or (4.14), respectively. This equation can be solved to find a differential equation for ψ.

$$\dot{\psi} = \frac{\left(f_x \sin\psi - f_y \cos\psi\right)\left(2WVB_1 - KV\right)}{A_4 \cos\gamma} \tag{4.18}$$

This results in a system of five differential equations – x, y, z, ψ, and γ – with two unknown initial conditions – ψ and γ.

4.1.1 Legendre-Clebsch Necessary Condition

The Hamiltonian equation is

$$H = A_4 + \lambda_x V \cos\gamma\cos\psi + \lambda_y V \cos\gamma\sin\psi + \lambda_z V \sin\gamma \tag{4.19}$$

and the costates are represented by

$$\begin{aligned} \lambda_x &= \frac{-A_4 \cos\gamma\cos\psi}{V} \\ \lambda_y &= \frac{-A_4 \cos\gamma\sin\psi}{V} \\ \lambda_z &= \frac{-A_4 \sin\gamma}{V} \end{aligned} \tag{4.20}$$

There are two controls for this section expressed as

$$u = \begin{bmatrix} \psi \\ \gamma \end{bmatrix} \tag{4.21}$$

This results in a 2x2 matrix for the second partial derivative of the Hamiltonian such that

$$H_{uu} = V\begin{bmatrix} -\lambda_x \cos\gamma\cos\psi - \lambda_y \cos\gamma\sin\psi & \lambda_x \sin\gamma\sin\psi - \lambda_y \sin\gamma\cos\psi \\ \lambda_x \sin\gamma\sin\psi - \lambda_y \sin\gamma\cos\psi & -\lambda_x \cos\gamma\cos\psi - \lambda_y \cos\gamma\sin\psi - \lambda_z \sin\gamma \end{bmatrix} \tag{4.22}$$

Substituting in the costates from (4.21) will result in

$$H_{uu} = V\begin{bmatrix} A_4(\cos\gamma)^2 & 0 \\ 0 & A_4 \end{bmatrix} \tag{4.23}$$

Therefore, this matrix will be nonnegative definite.

4.1.2 Weierstrass Test

Substituting the optimal costates from (4.20) into the Hamiltonian in (4.19) for any potential control results in the following equation.

$$H(u) = A_4\left[1 - \left(\cos\psi\cos\psi^o + \sin\psi\sin\psi^o\right)\cos\gamma\cos\gamma^o - \sin\gamma\sin\gamma^o\right] \tag{4.24}$$

In Appendix B, it is proven that this simplifies to

$$H(u) = A_4(1 - N) \geq 0 \tag{4.25}$$

where

$$N \leq 1 \tag{4.26}$$

Therefore, this condition is always satisfied.

4.2 Velocity as a State

This next section investigates including the velocity of the vehicle as a fourth state. The new equations of motion will now consist of the equations in (4.1-3) and also

$$\dot{V} = \frac{T - D}{m} - g\sin\gamma \tag{4.27}$$

In this equation, m is the mass of the vehicle, g is gravity, and T is the thrust of the vehicle, which, for optimal results should be held constant at its maximum value. In addition, D is the drag and is represented by

$$D = \left(C_{Do} + \frac{C_L^2}{e\pi AR}\right)\frac{1}{2}\rho V^2 S \tag{4.28}$$

Here, C_{Do} is the nominal drag coefficient, AR is the aspect ratio, e is the efficiency factor, ρ is the density of air, S is the wing area and C_L is the lift coefficient that is approximated by

$$C_L = \frac{L}{\frac{1}{2}\rho V^2 S} = \frac{mg}{\frac{1}{2}\rho V^2 S} \tag{4.29}$$

These substitutions result in the following velocity differential equation

$$\dot{V} = \frac{T}{m} - g\sin\gamma - B_2 V^2 - \frac{B_3}{V^2} \tag{4.30}$$

with

$$\begin{aligned} B_2 &= \frac{C_{Do}\rho S}{2m} \\ B_3 &= \frac{(mg)^2}{\frac{1}{2}\rho S m e \pi AR} \end{aligned} \tag{4.31}$$

The same process as outlined earlier is used to reduce the order of the problem. The new costate differential equation is found to be

$$\dot{\lambda}_V = \frac{A_4}{V} - \frac{\lambda_V}{V}\left(\frac{T}{m} - g\sin\gamma + B_2 V^2 - \frac{3B_3}{V^2}\right) \tag{4.32}$$

Next the new differential equations for the flight path angle and the heading angle are

$$\dot{\psi} = \frac{(f_x \sin\psi - f_y \cos\psi)(2WVB_1 - KV)}{\cos\gamma\left[A_4 - \lambda_V\left(B_2 V^2 + \frac{B_3}{V_2} - \frac{T}{m}\right)\right]} \tag{4.33}$$

and

$$\dot{\gamma} = \frac{G_1 + G_2}{V\left[-A_4 + \lambda_V \cos\gamma\left(B_2 V^2 + \frac{B_3}{V^2} - \frac{T}{m}\right)\right]} \tag{4.34}$$

with

$$G_1 = -2WB_1V^2\cos\gamma + V^2\sin\gamma(K - 2WB_1)(f_x\cos\psi + f_y\sin\psi)$$
$$G_2 = g\cos\gamma\left[-A_4 + 2\lambda_V\left(\frac{B_3}{V^2} - B_2V^2\right)\right] \tag{4.35}$$

This process now results in a system of seven differential equations with three unknown initial conditions to be determined.

4.2.1 Legendre-Clebsch Necessary Condition

The Hamiltonian equation is

$$H = A_4 + \lambda_x V\cos\gamma\cos\psi + \lambda_y V\cos\gamma\sin\psi + \lambda_z V\sin\gamma + \lambda_V\dot{V} \tag{4.36}$$

and the costates are represented by

$$\lambda_x = \frac{\cos\gamma\cos\psi}{V}\left[-A_4 + \lambda_V\left(B_2V^2 + \frac{B_3}{V^2} - \frac{T}{m}\right)\right]$$
$$\lambda_y = \frac{\cos\gamma\sin\psi}{V}\left[-A_4 + \lambda_V\left(B_2V^2 + \frac{B_3}{V^2} - \frac{T}{m}\right)\right] \tag{4.37}$$
$$\lambda_z = \frac{\sin\gamma}{V}\left[-A_4 + \lambda_V\left(B_2V^2 + \frac{B_3}{V^2} - \frac{T}{m}\right)\right] + \frac{\lambda_V g}{V}$$

Again, there are two controls which can be expressed as

$$u = \begin{bmatrix}\psi \\ \gamma\end{bmatrix} \tag{4.38}$$

Taking the second derivative of the Hamiltonian and substituting in the costates from (4.37) result in

$$H_{uu} = \begin{bmatrix}(A_4 - \lambda_v H_1)(\cos\gamma)^2 & 0 \\ 0 & A_4 - \lambda_v H_1\end{bmatrix}$$
$$H_1 = \left(B_2V^2 + \frac{B_3}{V^2} - \frac{T}{m}\right) \tag{4.39}$$

This matrix will be nonnegative definite as long as the following inequality is satisfied for all time

$$A_4 - \lambda_v H_1 \geq 0 \tag{4.40}$$

4.2.2 Weierstrass Test

Substituting the optimal costates from (4.37) into the Hamiltonian in (4.36) for any potential control results in the following equation.

$$\begin{aligned} H(u) &= \left(A_4 - \lambda_V H_1\right)\left(1 - N\right) \geq 0 \\ N &= 1 - \left(\cos\psi \cos\psi^o + \sin\psi \sin\psi^o\right)\cos\gamma \cos\gamma^o - \sin\gamma \sin\gamma^o \end{aligned} \tag{4.41}$$

where

$$N \leq 1 \tag{4.42}$$

as shown in Appendix B. Therefore, this condition is satisfied when

$$A_4 - \lambda_V H_1 \geq 0 \tag{4.43}$$

which is the same condition as in (4.40).

CHAPTER 5

SINGLE VEHICLE 3D RESULTS

In this chapter are presented results using the 3D equations of motion, both with a constant velocity and with a varying velocity. First, three sets of results are presented for both the terrain masking and minimum time optimization options. In these cases, the terrains used are flat planes with a progressively steeper hill. In addition, the initial altitude for these tests is very close to the desired flight altitude. The next set of results is for a case where the initial altitude is significantly different than the desired flight altitude. As before, the terrain used is a flat plane with a single hill and both terrain masking and minimum time flights are considered. The final set of results uses real terrain.

Figures 5.1 – 5.6 depict the results using $K = 0$ – the minimum time case – over progressively steeper hills. Results for each hill steepness are presented in two views, one 3D view on the left and one overhead view on the right. The results in Figure 5.1

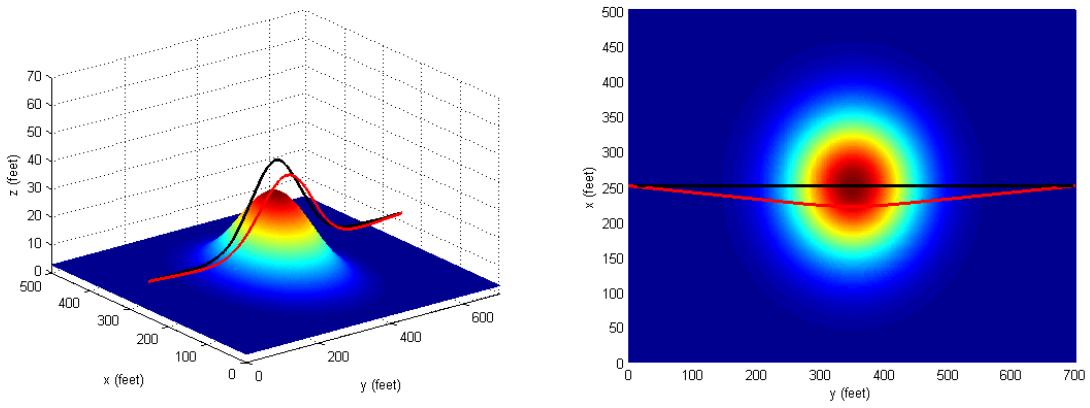

Figure 5.1: Results for $K = 0$ with a hill height of 30 feet.

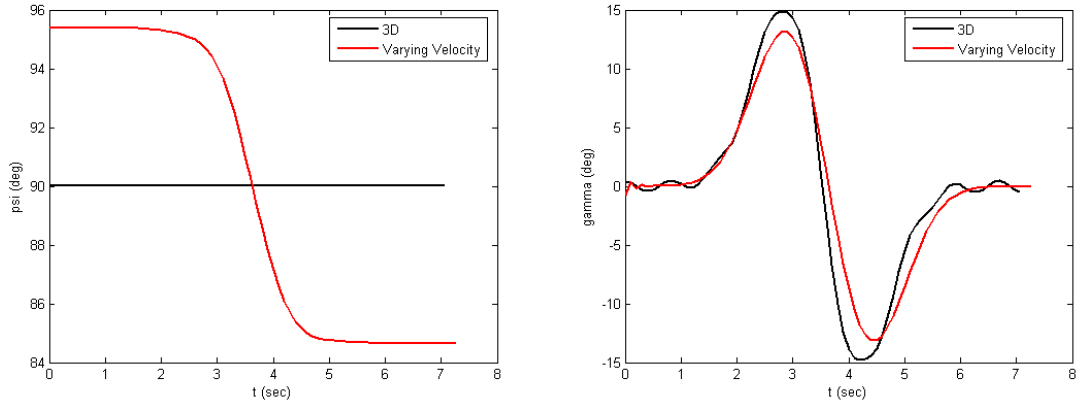

Figure 5.2: Controls for $K = 0$ with a hill height of 30 feet.

and Figure 5.2 are for the least steep hill with a height of 30 feet. Figure 5.3 and Figure 5.4 depict the results for a terrain with a hill height of 40 feet. The steepest hill, in Figure 5.5 and Figure 5.6, has a height of 50 feet. The first plots in each set contain the 3D and overhead views of the trajectories. The second set of plots contains the heading angle –

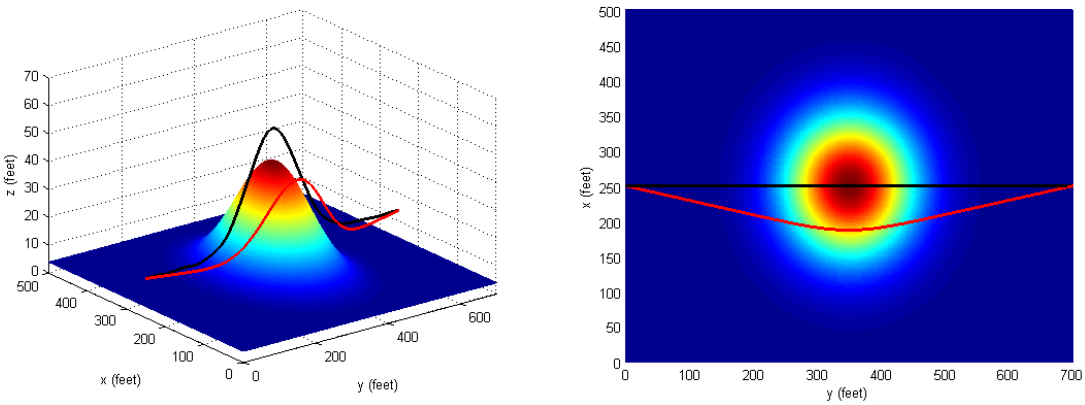

Figure 5.3: Results for $K = 0$ with a hill height of 40 feet.

on the left – and the flight path angle – on the left. The black line in each plot depicts the trajectory for the constant velocity case while the red line depicts the trajectory for the varying velocity case.

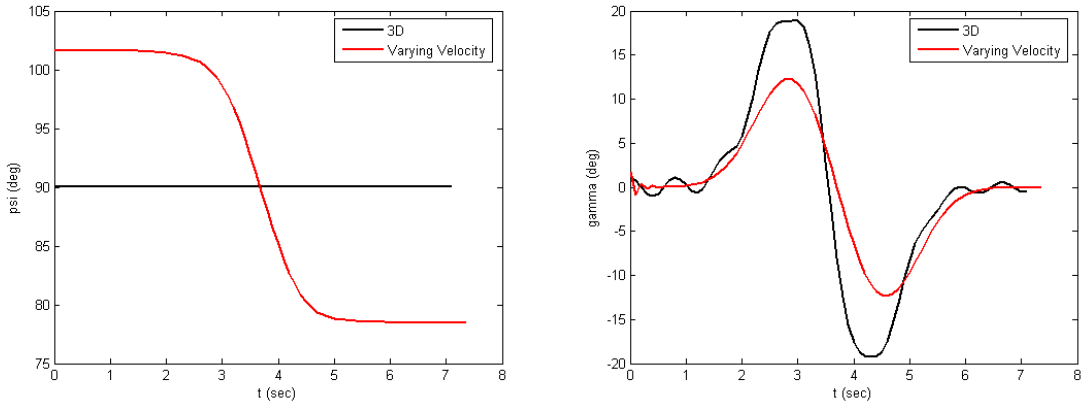

Figure 5.4: Controls for $K = 0$ with a hill height of 40 feet.

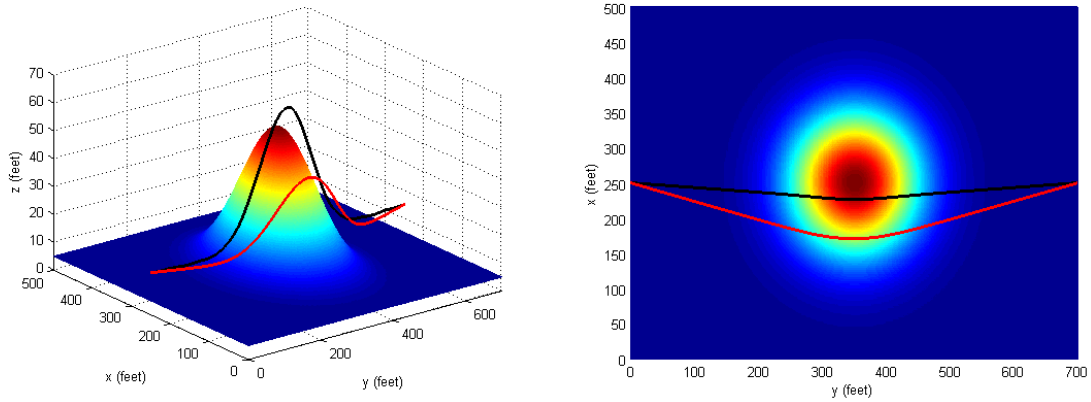

Figure 5.5: Results for $K = 0$ with a hill height of 50 feet.

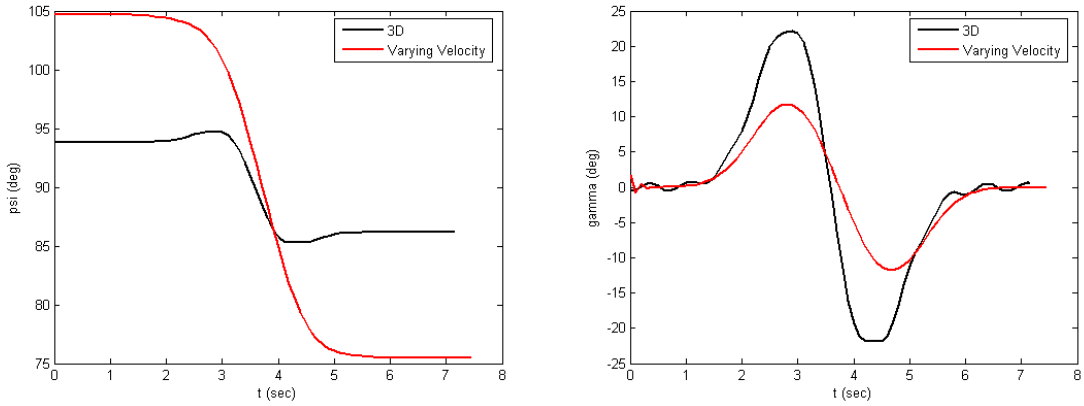

Figure 5.6: Controls for $K = 0$ with a hill height of 50 feet.

In the first two cases, it can be seen that the results for the constant velocity case goes directly over the hill. In the third case, the constant velocity trajectory tends to veer slightly around the hill. In this case, the hill is steep enough that it is quicker to fly slightly around the hill instead of directly over it. For each of the three cases, the trajectories for the varying velocity formulation always veer to some degree around the hill, more than the trajectories using a constant velocity formulation.

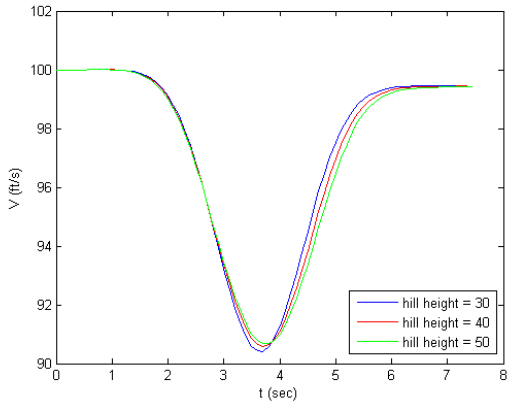

Figure 5.7: Velocity profiles from the three cases for $K = 0$.

Figure 5.7 shows the velocities from the varying velocity trajectories from the three minimum time cases. The blue line corresponds to the result over the 30-foot hill, the red line is for the result with the 40-foot hill and the green line represents the result for the 50-foot hill. In each case, the velocity decreases going over the hill, but, because as the hill height increases, the optimal trajectory veers more around the hill, the minimum velocity and velocity profile are almost the same for each case.

In the last chapter, an inequality was derived that must be satisfied in order for the second order variation tests to be satisfied for the varying velocity formulation.

$$W = A_4 - \lambda_V H_1 \geq 0 \tag{5.1}$$

This function, W, must be positive at all times along the trajectory. The plots for this function for each of the three minimum time cases can be seen in Figure 5.8. It can be seen here that the second order variation conditions are always satisfied.

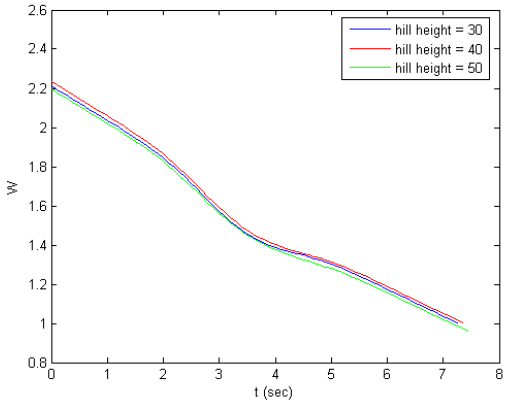

Figure 5.8: Second variation inequality for $K = 0$.

Figures 5.9 – 5.14 similarly show the results for three progressively steeper hills with $K = 1$ – the terrain masking case. Here it can be seen that the trajectories for both

the constant velocities and the varying velocity formulations are almost identical. In all three cases, the optimal trajectories go around the hill.

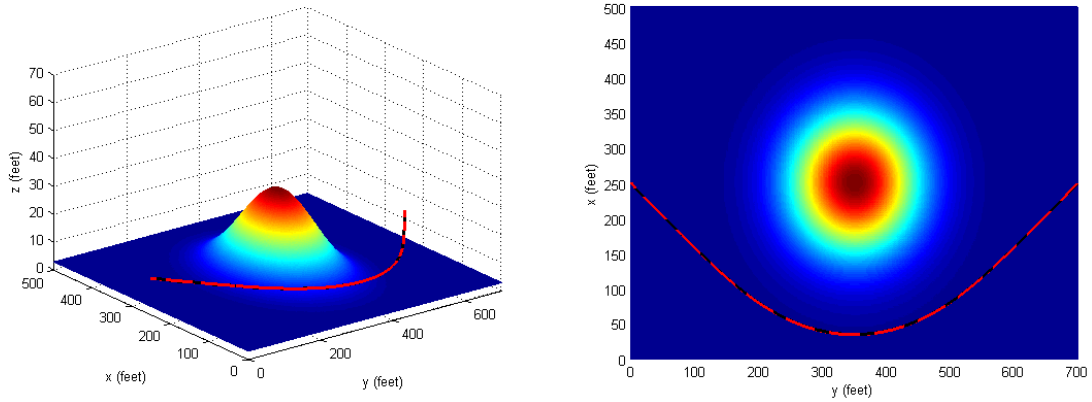

Figure 5.9: Results for $K = 1$ with a hill height of 30 feet.

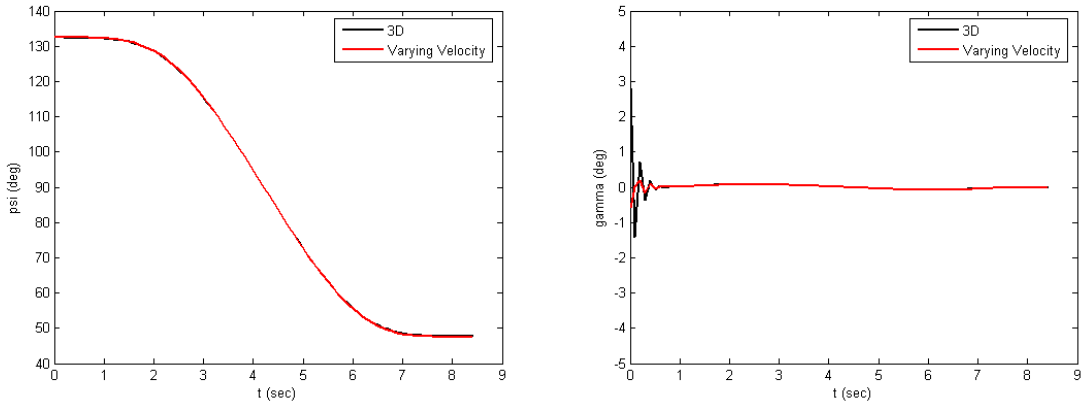

Figure 5.10: Controls for $K = 1$ with a hill height of 30 feet.

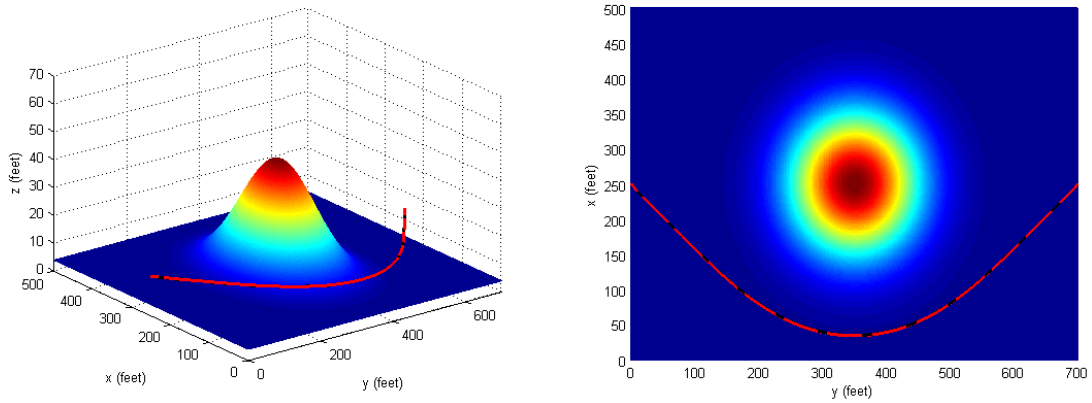

Figure 5.11: Results for $K = 1$ with a hill height of 40 feet.

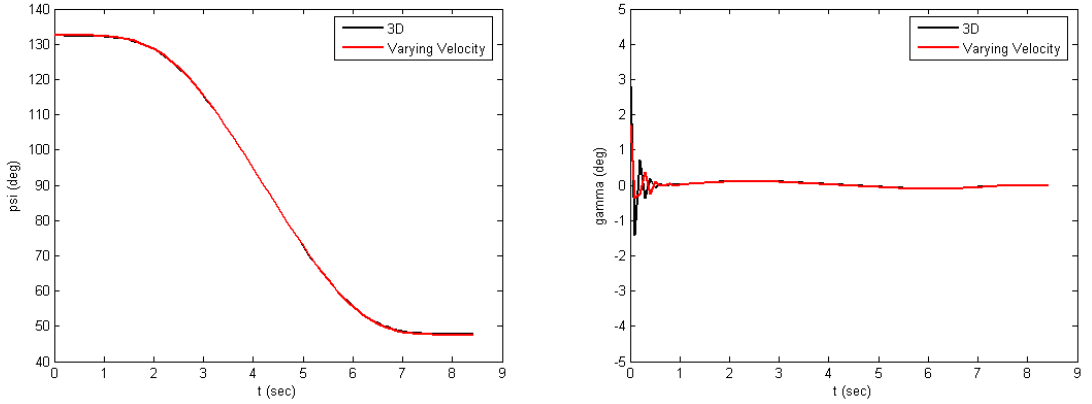

Figure 5.12: Controls for $K = 1$ with a hill height of 40 feet.

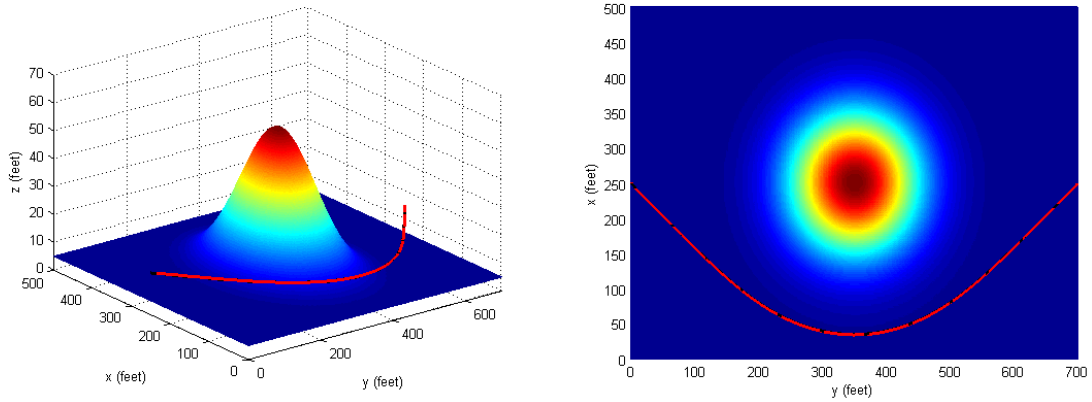

Figure 5.13: Results for $K = 1$ with a hill height of 50 feet.

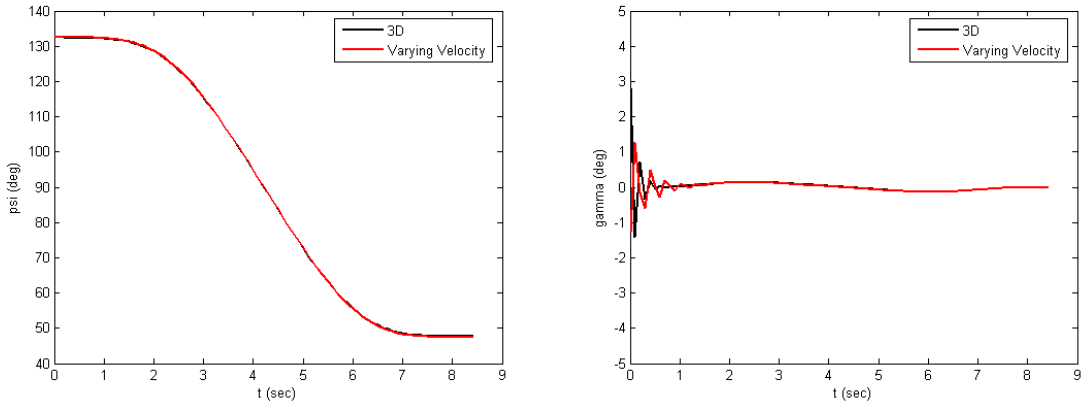

Figure 5.14: Controls for $K = 1$ with a hill height of 50 feet.

Velocity profiles for these cases can be seen in Figure 5.15. In each case, it can be seen that there is a slight fluctuation in the velocity at the beginning as the altitude settles, then it smoothly increases slightly throughout the flight. Figure 5.16 contains the plots of the function for the second variation tests for the three terrain masking varying velocity cases. As before, it can be seen that these tests are always satisfied.

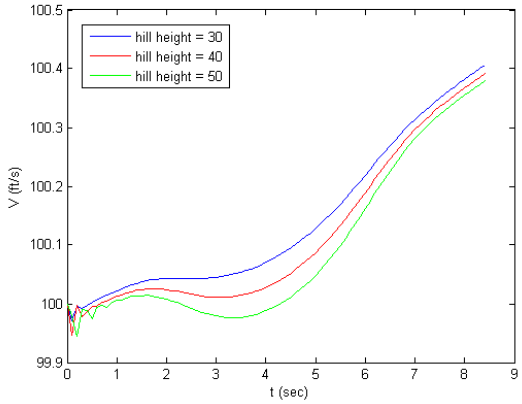

Figure 5.15: Velocity profiles from three cases of $K = 1$.

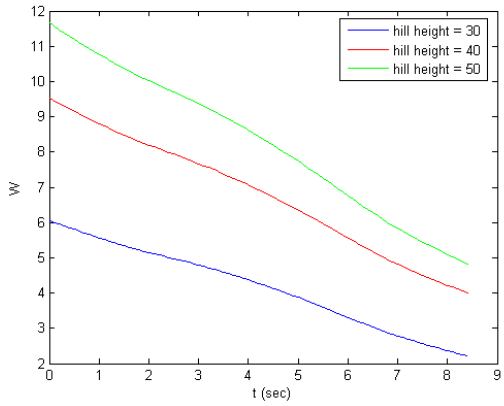

Figure 5.16: Second variation inequality for $K = 1$.

The final trajectories presented involve a flight over real terrain. Figure 5.17 shows the optimal results for $K = 0$ with the corresponding controls in Figure 5.18. Figure 5.19 depicts the results for $K = 1$ and those controls are shown in Figure 5.20. Both are overhead views of the terrain and trajectories. The red sections indicate hills while the blue parts are valleys. In both plots, the constant velocity trajectory is shown with black and the varying velocity path is in red. The initial position is marked with a red circle on the left of the plots while the destination is marked with a red star on the right.

In Figure 5.17, the minimum time case, there is a significant difference in the two trajectories. This is because for the case with the varying velocity, the vehicle loses speed going uphill – increasing the flight time – and gains speed going downhill – decreasing the flight time. Therefore, the flight time is minimized by lessening the amount of uphills flown. Instead, the trajectory for the minimum time case with the varying velocity is quite similar to the terrain masking trajectories, which are depicted in Figure 5.19. It can be seen that the optimal trajectories for the terrain masking case are very similar to each other, whether considering a constant or varying velocity flight.

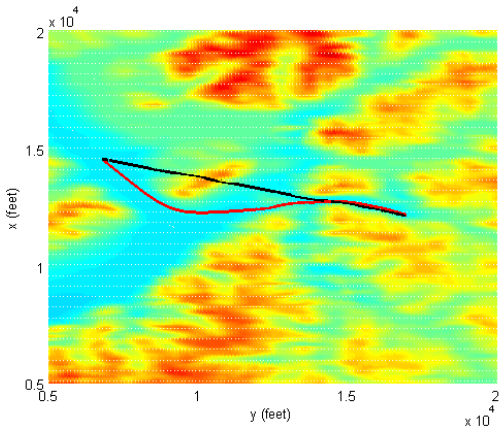

Figure 5.17: Optimal trajectories for $K = 0$.

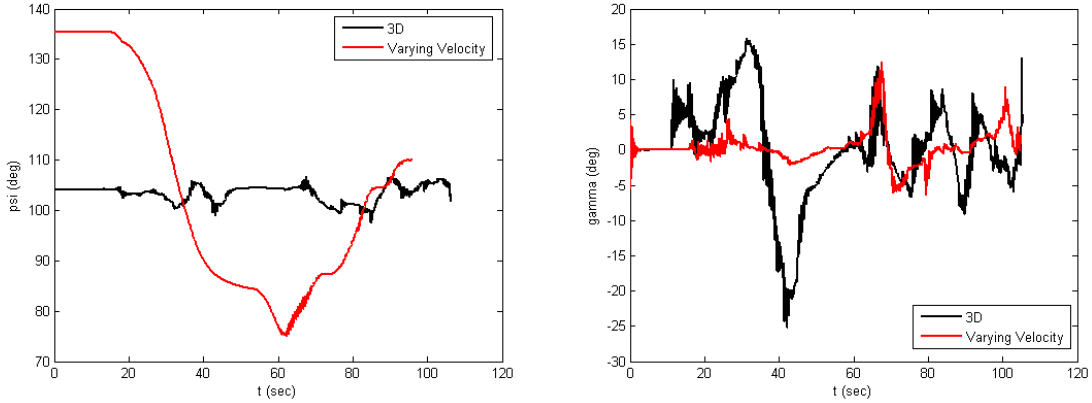

Figure 5.18: Controls for $K = 0$.

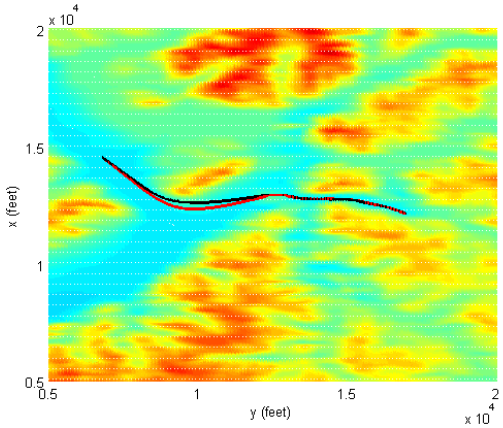

Figure 5.19: Optimal trajectories for $K = 1$.

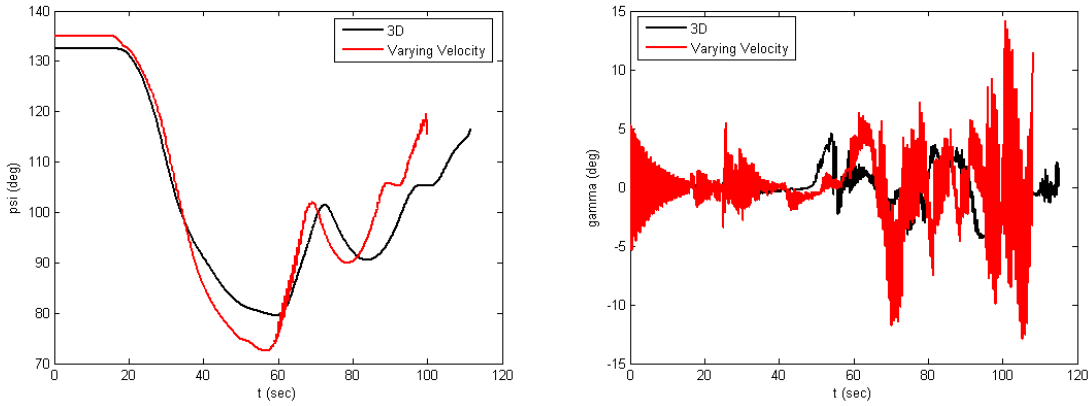

Figure 5.20: Controls for $K = 1$.

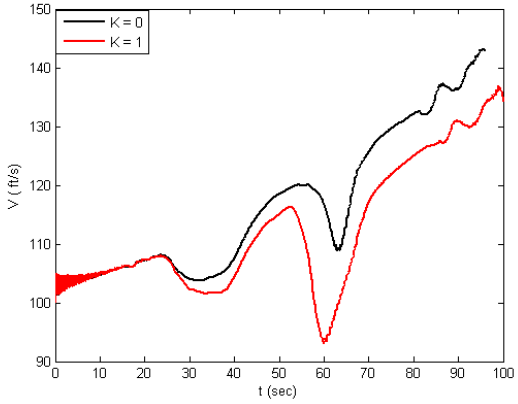

Figure 5.21: Velocities for flights over real terrain.

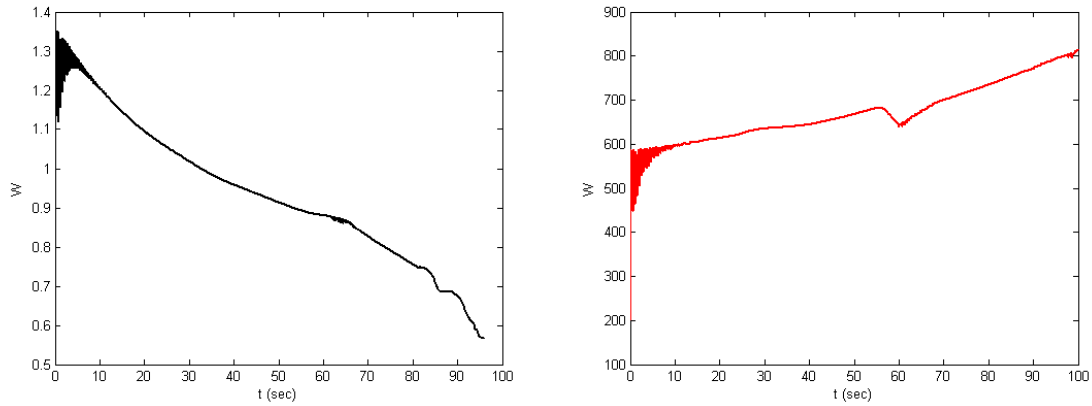

Figure 5.22: Second variation inequality for flights over real terrain.

The velocities for the varying velocity trajectories from Figures 5.17 and 5.19 are depicted in Figure 5.21. In this plot, the velocity from the minimum time formulation is depicted be the black line while the red line represents the velocity from the terrain masking formulation. The plots of the function from the second variation analysis inequality are depicted in Figure 5.22. The plot on the left shows the function from the minimum time case while the plot on the right shows the function for the terrain masking case. It can be seen that both functions are positive at all time.

CHAPTER 6

SIMULATOR RESULTS AND COMPARISONS

This chapter more closely examines the formulations and results from the previous chapters concerning single vehicle optimal paths. First a direct comparison of the results for all four formulations – for both minimum time and terrain masking flights – will be made. Next the trajectories will be implemented in a full six degree-of-freedom flight simulator for a fixed wing UAV. Then results from a simple flight test will be examined. Finally, comparisons will be made between the pseudo-3D cases from Chapters 2 and 3 with similar results found using GESOP (Graphical Environment for Simulation and Optimization).

6.1 Trajectory Comparison

This section examines the results from the previous chapters. For a given terrain, a flat plane with a single hill, the optimal trajectories found to navigate it for both minimum time and terrain masking flight are compared. The formulations considered include the simplified and local tangent plane equations of motion for the pseudo-3D case as well as the constant velocity and varying velocity 3D equations of motion. This is repeated for three different hill steepnesses.

Figures 6.1 – 6.3 contain the results for the minimum time, $K = 0$, case. Each figure portrays the results from a different hill height. The top two plots are a 3D view and an overhead view of the trajectories from the pseudo-3D case while the bottom two plots depict the paths for the 3D cases. For these cases, the trajectories from using the

simplified equations of motion and from using the local tangent plane equations of motion are the same and are represented by the black line. In the bottom two plots, the

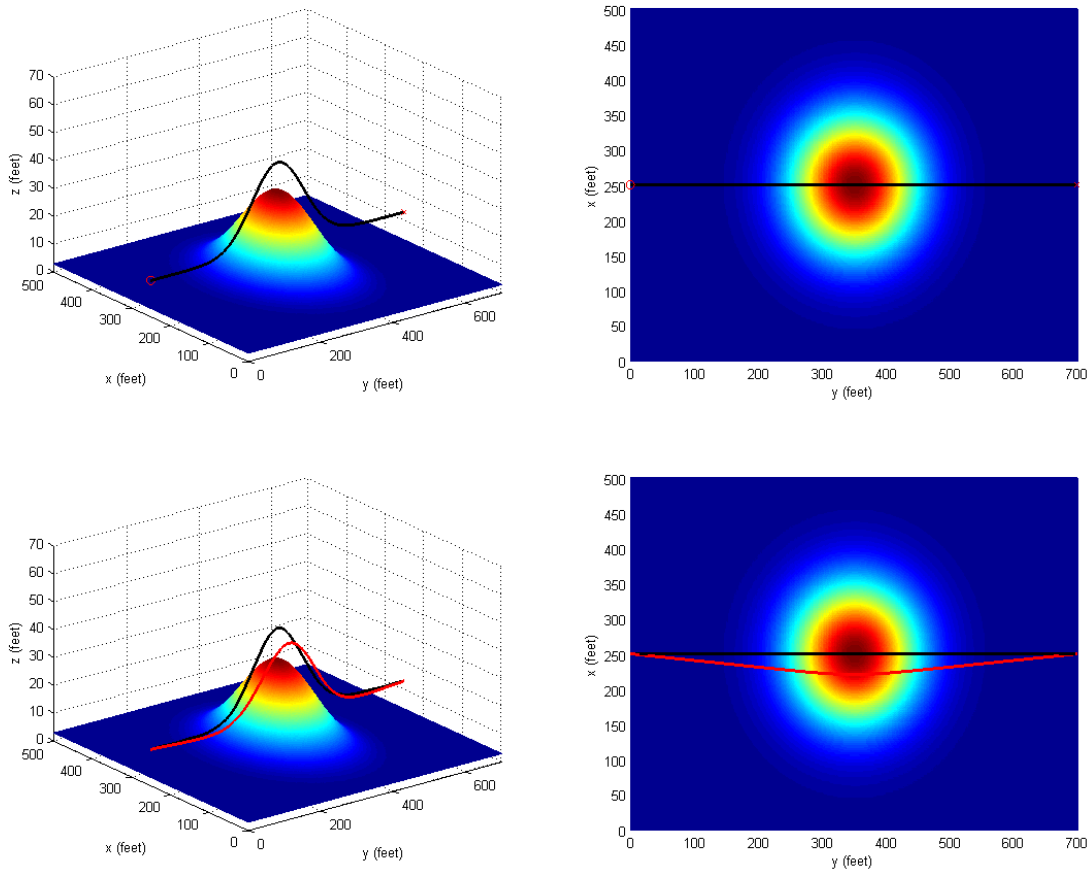

Figure 6.1: Trajectories for $K = 0$ and hill height = 30.

black line represents the simplified the constant velocity 3D equations of motion. The red line is for the varying velocity 3D equations of motion. The plots for the 3D equations of motion trajectories are the same as depicted in Chapter 5, and are repeated here for convenience. In the first two cases, with hill heights of 30 and 40 feet, the constant velocity 3D trajectories are the same as the pseudo-3D formulations; however,

in the steepest hill, the 3D trajectory begins to veer around the hill. In all three cases, the varying velocity trajectory veers around the hill to some extent.

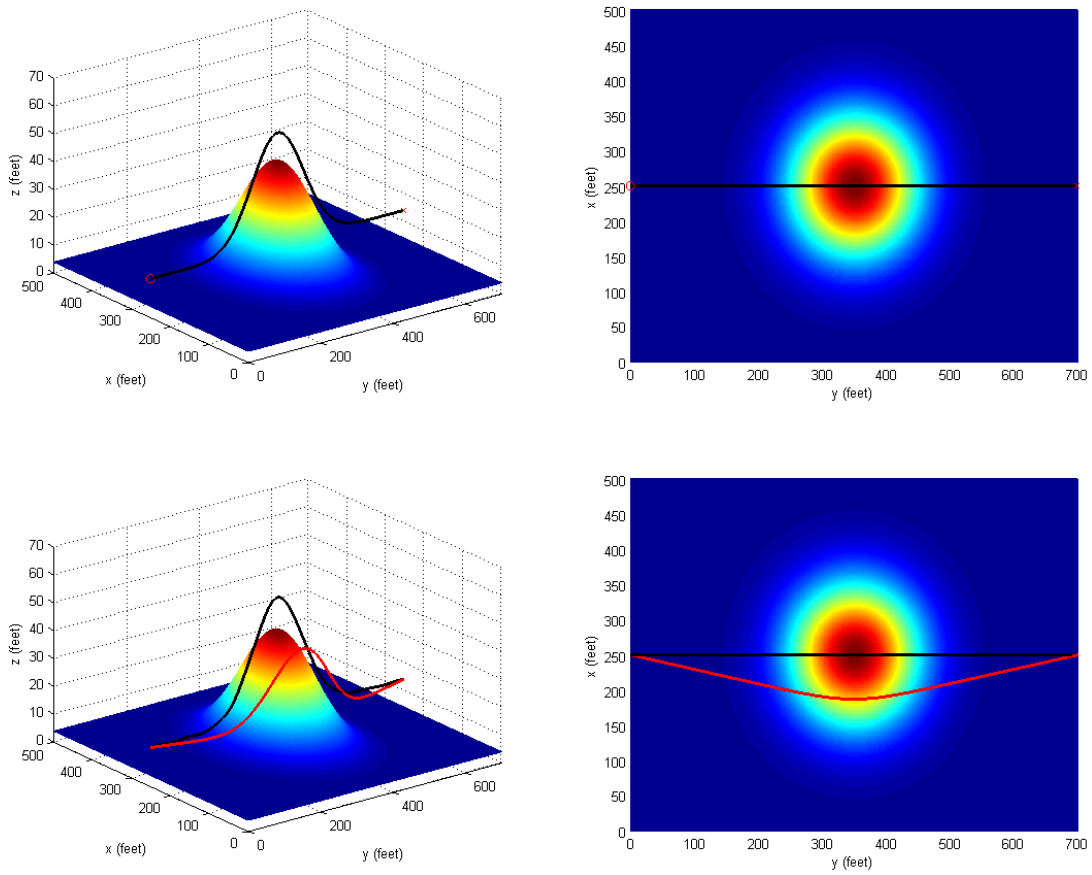

Figure 6.2: Trajectories for $K = 0$ and hill height = 40.

Some details from the various cases portrayed in these figures are tabulated below in Table 6.1. Here, the time for the flight and the cost of the flight can be compared for each set of equations of motion investigated. In this table, it can be seen that the flight time doesn't change with the simplified equations of motion, while the time increases for the local tangent plane and 3D equations of motion. This is because the time needed to

fly vertically is ignored in the simplified equations of motion. This time is better accounted for with the local tangent plane equations of motion, but these final times are still slightly less than the final times with the 3D equations of motion, especially when the hill steepness is greater. The final times for the varying velocity cases are significantly greater due to the loss in velocity during the flights.

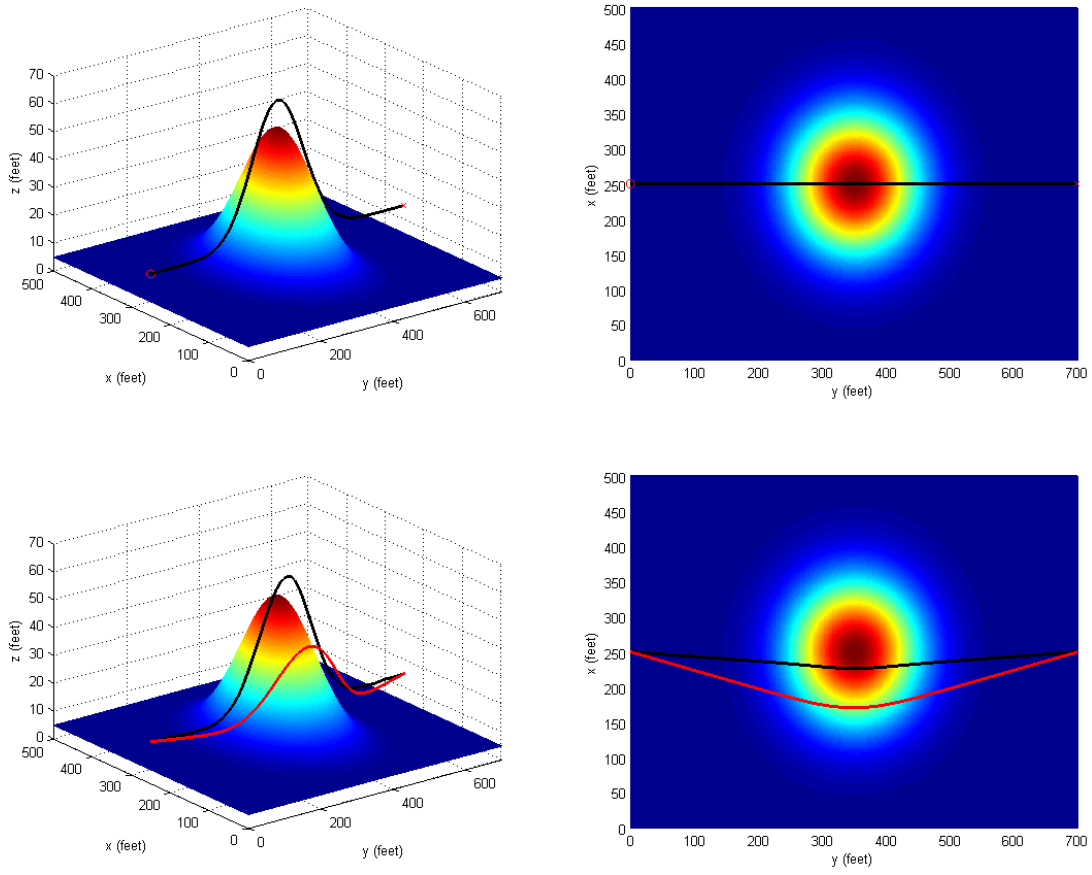

Figure 6.3: Trajectories for $K = 0$ and hill height = 50.

Table 6.1: Trajectory data for $K = 0$ flights

	Hill Height = 30		Hill Height = 40		Hill Height = 50	
	tf	cost	tf	cost	tf	cost
simplified	7	7	7	7	7	7
local tangent plane	7.06	7.06	7.1	7.1	7.15	7.15
3D	7.06	7.063	7.11	7.116	7.16	7.165
varying velocity	7.27	7.289	7.37	7.371	7.45	7.451

Figures 6.4 – 6.6 contain the plots for the results for $K = 1$. These plots are for cases parallel to those shown in Figures 6.1 – 6.3. The same three hill heights are displayed with the four sets of trajectories depicted. As in the earlier plots, the top plots

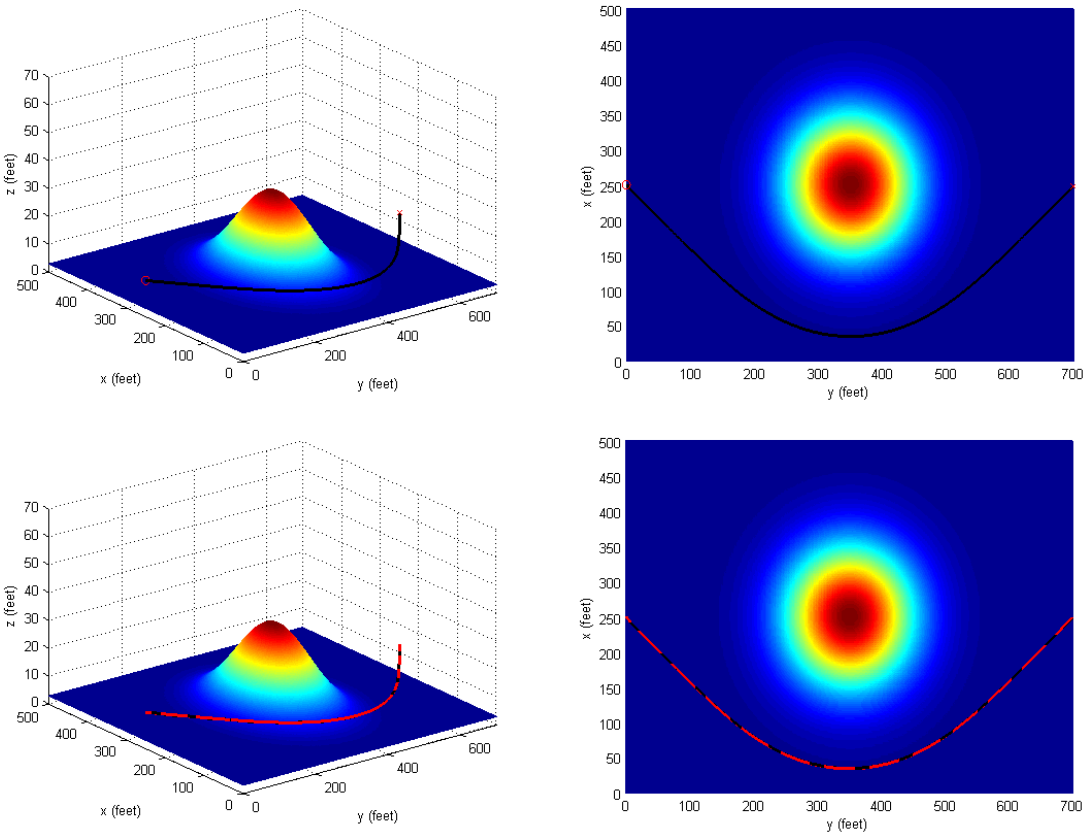

Figure 6.4: Trajectories for $K = 1$ and hill height = 30.

show the trajectories from using the simplified and local tangent plane equations of motion. The bottom two plots depict the results from Chapter 5 for the trajectories using the 3D constant velocity and varying velocity equations of motion. In each of the four cases, for each of the three hill steepnesses, the trajectories appear the same. The trajectory always curves around the given hill.

Table 6.2 contains the final time and cost information for the trajectories from each set of equations of motion and for each hill height for the $K = 1$ formulation. It can be seen here that there is very little difference in these results regardless of the equations of motion used or the hill steepness.

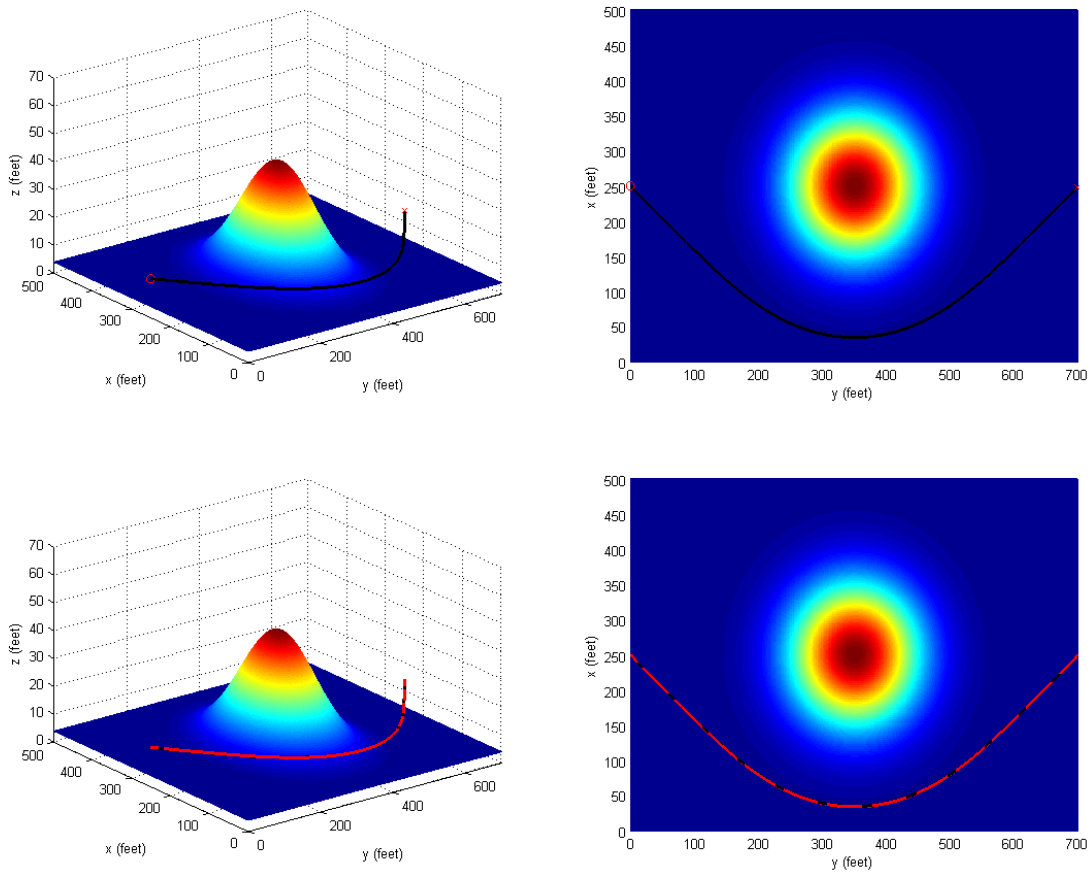

Figure 6.5: Trajectories for $K = 1$ and hill height = 40.

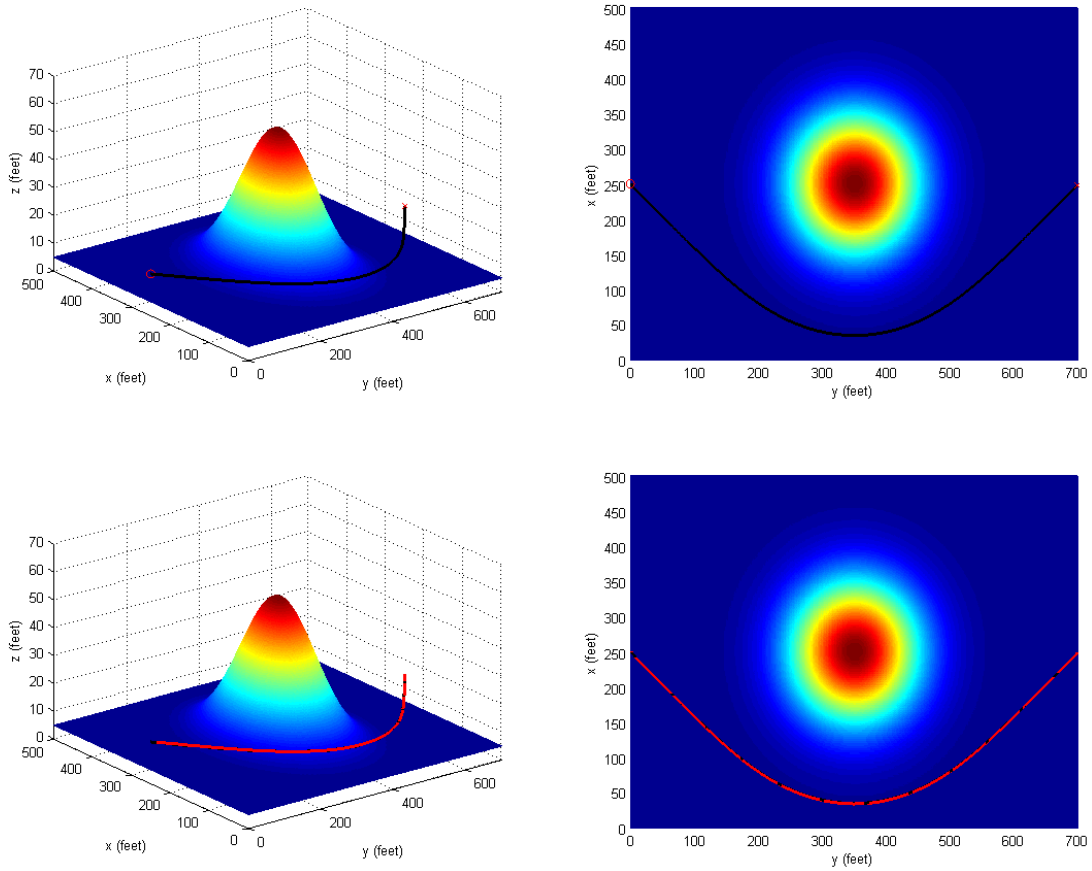

Figure 6.6: Trajectories for $K = 1$ and hill height = 50.

Table 6.2: Trajectory data for $K = 1$ flights

	Hill Height = 30		Hill Height = 40		Hill Height = 50	
	tf	cost	tf	cost	tf	cost
simplified	8.42	26.349	8.42	35.1314	8.42	43.9143
local tangent plane	8.42	26.348	8.42	35.1305	8.42	43.9132
3D	8.42	26.349	8.42	35.132	8.42	43.914
varying velocity	8.41	26.306	8.42	35.108	8.42	43.88

6.2 SIMULATOR IMPLEMENTATION

Some of the results from the last section were then implanted on a 6 degree-of-freedom flight simulator. This simulator is for a small fixed wing aircraft that is being built for flight research at Georgia Tech. The results from each of the four single vehicle formulations for a single hill height are implemented on the simulator and the results are compared. This is completed for both the minimum time and terrain masking cases.

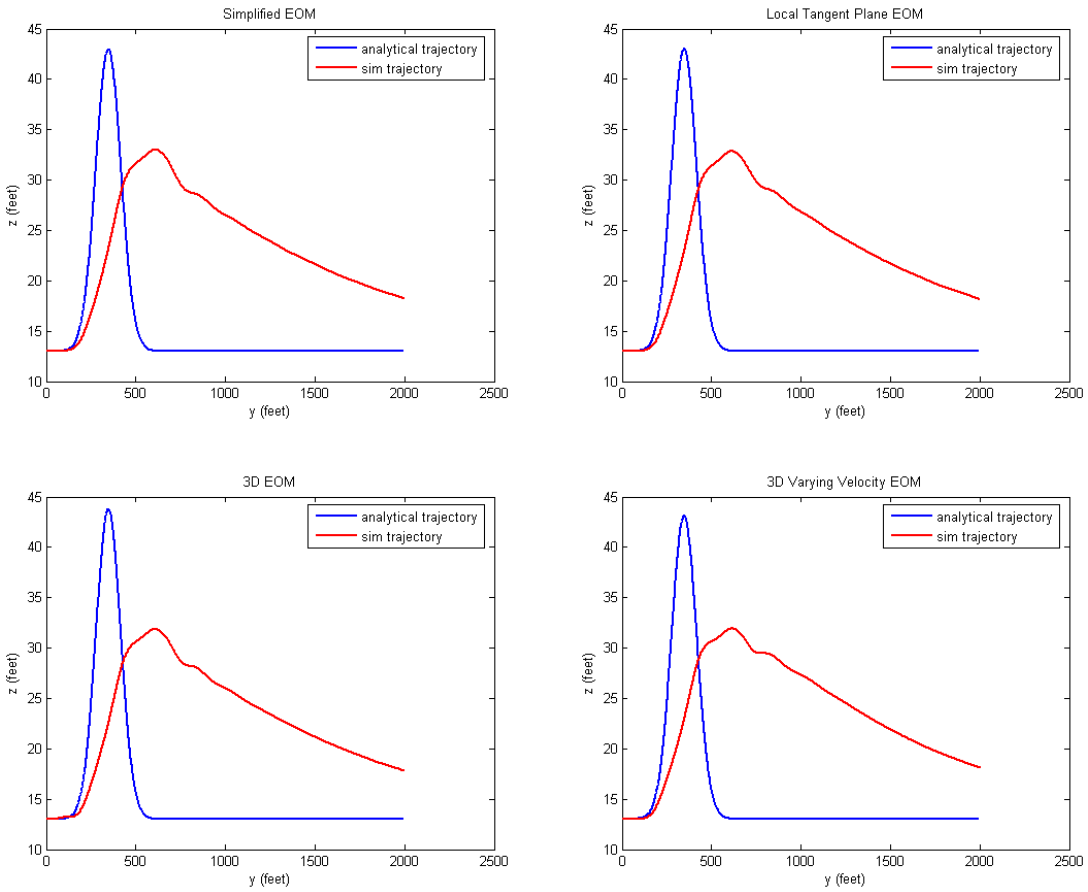

Figure 6.7: Simulator comparisons for $K = 0$.

In Figure 6.7, the results for the minimum time cases for each set of equations of motion are shown, along with the corresponding simulator results. In these plots, the

blue line represents the analytical trajectory found while the red line shows the corresponding simulator result. In each case, it can be seen that there are some problems following the trajectories. The limit on the rate of change of the flight path angle is reached in each case, meaning that the simulator is slow to start climbing the hill and especially in going over the hill.

Figure 6.8 depicts the results for the terrain masking cases for each of the equations of motion. In each case, the overhead views of the trajectories are shown. As with the minimum time cases, there are some problems in following the trajectories. In this case the heading angle rate of change limit is reached, causing the simulator to lag in turning.

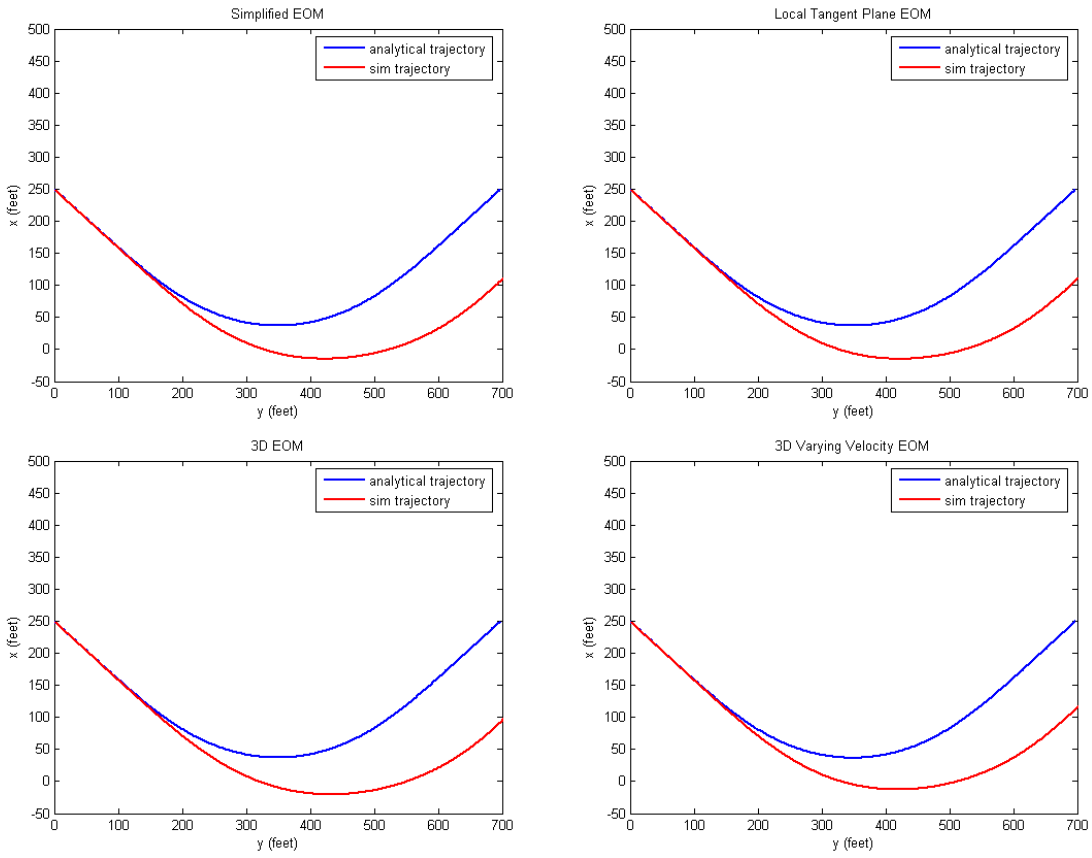

Figure 6.8: Simulator comparisons for $K = 1$.

6.3 FLIGHT DATA

This section examines a few flight test made using some analytical trajectories found. In this case, the trajectories were flown on the GTmax experimental helicopter. The trajectories are terrain masking flights using the local tangent plane equations of motion.

Figures 6.9 and 6.10 depict the results for the two terrain sets used here. In Figure 6.9, a terrain with five hills was considered while a terrain with three hills was used for the results in Figure 6.10. In both plots, the blue line represents the analytical trajectory while the red line indicates the actual flown trajectory. In both cases, there is a

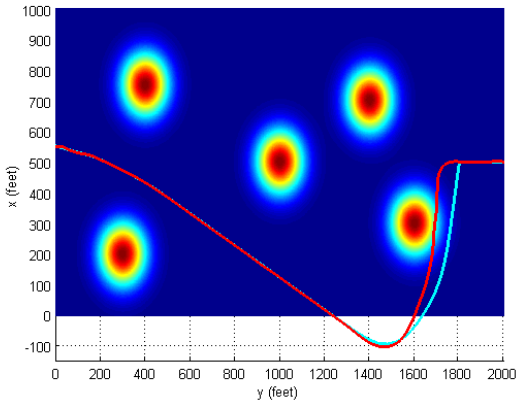

Figure 6.9: Flight data for 5 hill terrain.

slight difference at the beginning of the flight – towards the right of the plot – then the flight trajectory follows the analytical path closely. This difference is due to the fact that the helicopter was not oriented in the same heading as ψ^o. Therefore, the helicopter had to turn to start following the trajectory, which causes the slight difference.

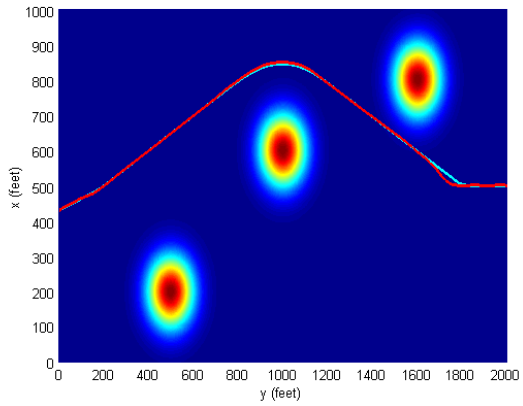

Figure 6.10: Flight data for 3 hill terrain.

6.4 GESOP

Several test cases from the previous chapter were also compared to results found using GESOP. GESOP (Graphical Environment for Simulation and Optimization) is a graphical optimization program that includes four different optimization programs using different methods such as collocation or multiple shooting. It was developed at the Institute for Flight Mechanics and Control at the University of Stuttgart and allows the implementation of every kind of optimization model. The optimization can be performed by using program interface modules – available in Ada95, C or Fortran – that contain the optimization model, which are then compiled and used by the program. The solutions can be shown in the program itself with Quick View or can be exported for further processing.

This program allows the optimization of a full six degree-of-freedom UAV model with the full dynamics included. For the first approach the model of a preliminary system GA Tech UAV model was used. When experimental values for this UAV are available, changes to the program can be made.

Two different test cases were examined, and the answers compared with the solutions generated by the analytical method outlined above. The first consists of flights with moving targets and threats at a constant altitude. The second case examined deals with pop-up threats.

First is the situation when the target must rendezvous with a moving target while avoiding two moving threats. The results from this can be seen in Figure 6.11. The blue line is the 3DoF GESOP result, the black line is the 6DoF GESOP result, the red line is the 3DoF analytical result and the green line is a modified 6 DoF GESOP result. The top

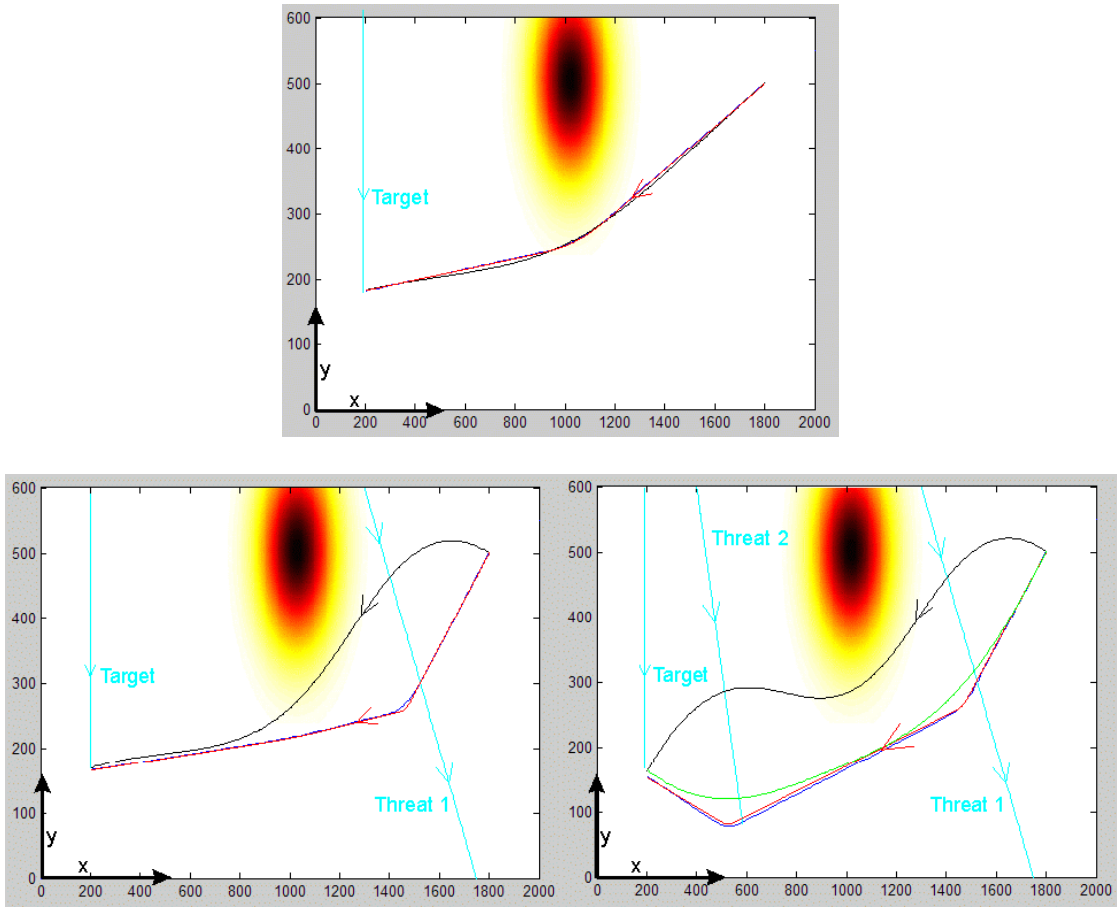

Figure 6.11: GESOP flights with a moving target and moving threats.

plot is when there are no threats yet present. The three solutions are pretty much the same, but the 6DoF-solution doesn‘t fly the turn as sharply as the 3DoF solutions. Next, in the bottom left plot, one moving threat is added. The two 3DoF solutions pass it in front while the 6DoF solution finds it more optimal to pass behind. Finally, the bottom right plot shows the results of the case when a second moving threat is included. Again, the 3DoF solutions pass in front of the threats while the original 6DoF result passes behind the threats. But in a simulation containing threats with their velocity reduced by 10% (green) the 6DoF simulation also passes in front. But there it can be seen that the turning rate especially at the second threat is much lower than for the unresticted 3DoF-simulations, so that a flight in front of the threats for the normal 6DoF would cause a significantly longer path taking longer than crossing behind.

Figure 6.12 shows a comparison between the 6 DoF GESOP results and the 3 DoF analytical results from above with a popup threat, with a terrain masking optimization. In this plot the black dashed line shows the original result without a popup

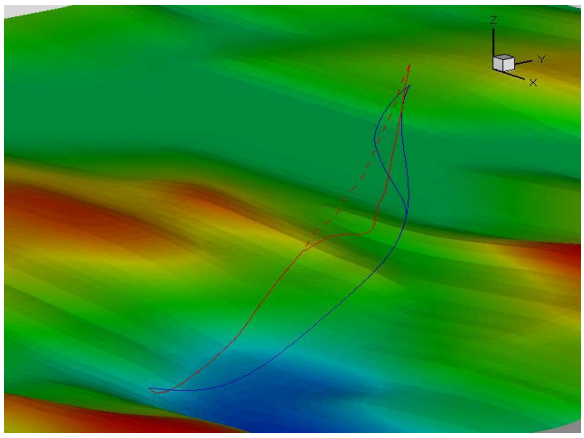

Figure 6.12: Flight with popup threats showing both
6 DoF GESOP and 3 DoF analytical solutions.

threat for the analytical result; the red line is then the corresponding result when the popup threat is included. The blue lines are the results using both full throttle and a reduced throttle using the 6 DoF GESOP.

Overall, it can be seen that a 6 DoF optimization with a full dynamics model over real terrain is available and working. It was found that the 6 DoF results were very similar to the 3 DoF results for tests at constant altitudes and unambiguous cases. However, the 6 DoF results can show significant differences for flights over discrete terrain due to full dynamics and ambiguous cases. An ambiguous case is where there are two solutions that don‘t differ very much in the cost function, but differ very much in the path, like taking the left or the right side for going around a symmetrical hill.

CHAPTER 7

MULTIPLE VEHICLES

This chapter examines the problem of finding optimal trajectories for multiple vehicles simultaneously. Two different situations are considered. The first is the case when there are two vehicles operating independently in the same area. They must each have a trajectory from their starting position to their ending position while avoiding flying too close to the other vehicles. The second case is formation flight. The vehicles must fly a set distance from the other vehicles and travel from the starting location to the ending location.

As in Chapter 2, the pseudo 3D equations of motion are used, both the simplified set and the local tangent plane equations of motion. First, the reduced order optimal equations are derived for both sets of equations of motion for the case of controlling two vehicles. Next, these equations are expanded to include the simultaneous control of an unspecified number of vehicles (n-vehicles).

7.1 Simplified Equations of Motion

For this formulation, the simplified equations of motion are used, as described above in equations (1.3) and (1.4).

$$\dot{x}_i = V_i \cos\psi_i \tag{7.1}$$

$$\dot{y}_i = V_i \sin\psi_i \tag{7.2}$$

Here, with i equal to one, (7.1) and (7.2) depict the equations of motion for vehicle 1 with a velocity, V_1, and a heading angle ψ_1. With i equal to two, (7.1) and (7.2) depict the

equations of motion for vehicle 2 with a velocity of V_2 and a heading angle of ψ_2. The variables x_1 and x_2 represent the positions with respect to the northward x-axis of vehicle 1 and 2, respectively, while y_1 and y_2 are the positions with respect to the eastward y-axis of vehicle 1 and 2, respectively. For this problem, the initial and final positions for each vehicle are specified.

The cost equation used for this problem is

$$J = \int_0^{t_{f1}} [J_{11} + J_2]dt + \int_0^{t_{f2}} [J_{12} + J_2]dt \tag{7.3}$$

Since the final time for each vehicle can be different, the cost equation is composed of two integrals covering the time for the flight of each vehicle. In this problem, the cost equation for each vehicle is broken into two parts. The first part is

$$J_{1i} = (1-K) + Kf_i(x_i, y_i) \tag{7.4}$$

and represents the cost for either minimum time versus terrain masking, depending on K. As before, if $K = 0$, the problem is optimized solely with respect to minimum time while if $K = 1$, the problem is optimized purely with respect to terrain masking. The second part of the cost will change, depending on whether vehicle avoidance or formation flight is desired. It will be either

$$J_2 = \frac{W}{d} \tag{7.5}$$

for collision avoidance flight or

$$J_2 = W(d - d_c)^2 \tag{7.6}$$

for formation flight with

$$d = (x_1 - x_2)^2 + (y_1 - y_2)^2 \tag{7.7}$$

In these equations, W is a weighing parameter and d is a measure of the square of the distance between the two vehicles. It can be seen that d will create a singularity in J at collision. The altitudes of each of the vehicles are represented by the sum of $f_1(x_1, y_1)$ and $f_2(x_2, y_2)$ -- the terrain height at each respective vehicle position -- and a constant ground clearance.

The Hamiltonian equation for this system can be written as

$$H = A_4 + \lambda_{x1} V_1 \cos\psi_1 + \lambda_{y1} V_1 \sin\psi_1 + \lambda_{x2} V_2 \cos\psi_2 + \lambda_{y2} V_2 \sin\psi_2$$
$$A_4 = \sum_{\substack{i=1 \\ t \le t_{fi}}}^{2} \left(J_{1i} + J_2 \right) \tag{7.8}$$

The costate variables for the four states are given by λ_{xi} and λ_{yi}.

The optimality conditions for this problem are

$$H_{\psi i} = 0 \tag{7.9}$$

where $H_{\psi 1}$ represents the partial derivative of the Hamiltonian with respect to ψ_1 while $H_{\psi 2}$ represents the partial derivative of the Hamiltonian equation with respect to ψ_2 . Evaluating equation (7.8) results in the following two relationships.

$$\lambda_{yi} = \lambda_{xi} \frac{\sin\psi_i}{\cos\psi_i} \tag{7.10}$$

Since the Hamiltonian equation is not explicitly dependent on time, it will equal zero at all times. Using this fact and equations (7.8) and (7.9), the following two algebraic expressions for costates are found

$$\lambda_{y2} = \frac{-\sin\psi_2}{V_2} \left(\frac{A_4 \cos\psi_1 + \lambda_{x1} V_1}{\cos\psi_1} \right) \tag{7.11}$$

$$\lambda_{x2} = \frac{-\cos\psi_2}{V_2} \left(\frac{A_4 \cos\psi_1 + \lambda_{x1} V_1}{\cos\psi_1} \right) \tag{7.12}$$

Differential equations for the costates can be found by taking the partial derivatives of the Hamiltonian equation as shown below.

$$\begin{aligned} \dot{\lambda}_{xi} &= -H_{xi} \\ \dot{\lambda}_{yi} &= -H_{yi} \end{aligned} \tag{7.13}$$

This results in the following four differential equations.

$$\dot{\lambda}_{x1} = -Kf_{1x} + B_1 \tag{7.14}$$

$$\dot{\lambda}_{y1} = -Kf_{1y} + B_2 \tag{7.15}$$

$$\dot{\lambda}_{x2} = -Kf_{2x} - B_1 \tag{7.16}$$

$$\dot{\lambda}_{y2} = -Kf_{2y} - B_2 \tag{7.17}$$

with either

$$\begin{aligned} B_1 &= \frac{2W(x_1 - x_2)}{d^2} \\ B_2 &= \frac{2W(y_1 - y_2)}{d^2} \end{aligned} \tag{7.18}$$

for aircraft avoidance or

$$\begin{aligned} B_1 &= 4W(d - d_c)(x_1 - x_2) \\ B_2 &= 4W(d - d_c)(y_1 - y_2) \end{aligned} \tag{7.19}$$

The time derivative of equation (7.10) is taken and set equal to its counterpart in equation (7.15), with *i* equal to one in both cases. Rearranging this expression will result in a differential equation for ψ_1.

$$\dot{\psi}_1 = \frac{\cos\psi_1\left[(Kf_{1x} - B_1)\sin\psi_1 - (Kf_{1y} - B_2)\cos\psi_1\right]}{\lambda_{x1}} \tag{7.20}$$

Next, this is repeated for either equations (7.11) and (7.16) or equations (7.12) and (7.17), to determine a differential equation for ψ_2.

$$\dot{\psi}_2 = \frac{V_2 \cos\psi_1 \left[\left(Kf_{2y} + B_2 \right) \cos\psi_2 - \left(Kf_{2x} + B_1 \right) \sin\psi_2 \right]}{A_4 \cos\psi_1 + V_1 \lambda_{x1}} \tag{7.21}$$

This results in a system with seven differential equations – the four state equations, the two heading equations and the costate λ_{x1} – with three unknown initial values.

7.1.1 Legendre-Clebsch Necessary Conditions

For this formulation, the Hamiltonian equation is

$$H = A_4 + \lambda_{x1} V_1 \cos\psi_1 + \lambda_{y1} V_1 \sin\psi_1 + \lambda_{x2} V_2 \cos\psi_2 + \lambda_{y2} V_2 \sin\psi_2 \tag{7.22}$$

and the costates are represented by

$$\begin{aligned} \lambda_{y1} &= \lambda_{x1} \frac{\sin\psi_1}{\cos\psi_1} \\ \lambda_{y2} &= \frac{-\sin\psi_2}{V_2} \left(\frac{A_4 \cos\psi_1 + \lambda_{x1} V_1}{\cos\psi_1} \right) \\ \lambda_{x2} &= \frac{-\cos\psi_2}{V_2} \left(\frac{A_4 \cos\psi_1 + \lambda_{x1} V_1}{\cos\psi_1} \right) \end{aligned} \tag{7.23}$$

There are two controls here, represented by the vector

$$u = \begin{bmatrix} \psi_1 \\ \psi_2 \end{bmatrix} \tag{7.24}$$

This will result in the following matrix for the partial derivative of the Hamiltonian

$$H_{uu} = \begin{bmatrix} V_1 \left(-\lambda_{x1} \cos\psi_1 - \lambda_{y1} \sin\psi_1 \right) & 0 \\ 0 & V_2 \left(-\lambda_{x2} \cos\psi_2 - \lambda_{y2} \sin\psi_2 \right) \end{bmatrix} \tag{7.25}$$

Substituting in the costate equations from (7.23) will result in the following matrix.

$$H_{uu} = \begin{bmatrix} \dfrac{-\lambda_{x1} V_1}{\cos\psi_1} & 0 \\ 0 & \dfrac{-\lambda_{x2} V_2}{\cos\psi_2} \end{bmatrix} \tag{7.26}$$

In order to satisfy the condition, the following equations must be met.

$$\frac{-\lambda_{xi} V_i}{\cos\psi_i} \geq 0 \tag{7.27}$$

7.1.2 Weierstrass Test

Substituting the optimal costate equations into the Hamiltonian equation will result in the following expression for the variational Hamiltonian.

$$H(\psi_1, \psi_2) = A_4\left[1 - \cos\left(\psi_2^o - \psi_2\right)\right] + \frac{\lambda_{x1} V_1}{\cos\psi_1^o}\left[\cos\left(\psi_1^o - \psi_1\right) - \cos\left(\psi_2^o - \psi_2\right)\right] \tag{7.28}$$

This must satisfy

$$H(\psi_1, \psi_2) \geq 0 \tag{7.29}$$

In Appendix B.2, it is proven that this condition will be satisfied if the following inequalities are true.

$$\left|A_4 \cos\psi_1^o\right| \geq \left|\lambda_{x1} V_1\right| \tag{7.30}$$

$$sign(\lambda_{x1}) = -sign(\cos\psi_1) \tag{7.31}$$

7.2 Local Tangent Plane Equations of Motion

For this section the equations of motion used were seen above in equations (1.1) and (1.2) and are repeated here.

$$\dot{x}_i = \frac{V_i \cos\psi_i}{A_{1i}} + \frac{V_i f_{ix} f_{iy} \sin\psi_i}{A_{1i} A_{2i}} \tag{7.32}$$

$$\dot{y}_i = \frac{-V_i A_{1i} \sin\psi_i}{A_{2i}} \tag{7.33}$$

where

$$A_{1i} = \sqrt{1 + f_{ix}^2}$$
$$A_{2i} = \sqrt{1 + f_{ix}^2 + f_{iy}^2} \tag{7.34}$$

This process used is the same as above. The cost equation used is the same as in the previous section and can be seen in equations (7.3) – (7.7). The Hamiltonian equation is found to be

$$H = A_4 + \lambda_{xi}\left(\frac{V_i \cos\psi_i}{A_{1i}} + \frac{V_i f_{ix} f_{iy} \sin\psi_i}{A_{1i} A_{2i}}\right) + \lambda_{yi}\left(\frac{-V_i A_{1i} \sin\psi_i}{A_{2i}}\right) \tag{7.35}$$

where A_4 is defined in equation (7.8).

As before, equations were found for the costates using the Hamiltonian equation and the optimality equation seen in (7.9). These were found to be, as a function of λ_{x1},

$$\lambda_{y1} = \lambda_{x1}\left(\frac{-A_{21}\sin\psi_1 + f_{1x} f_{1y} \cos\psi_1}{A_{11}^2 \cos\psi_1}\right) \tag{7.36}$$

$$\lambda_{x2} = \frac{-A_{12}\cos\psi_2}{V_2}\left(\frac{A_4 A_{11}\cos\psi_i + V_1\lambda_{x1}}{A_{11}\cos\psi_1}\right) \tag{7.37}$$

$$\lambda_{y2} = \frac{\left(A_4 A_{11}\cos\psi_i + V_1\lambda_{x1}\right)\left(-f_{2x} f_{2y}\cos\psi_2 + A_{22}\sin\psi_2\right)}{V_1 A_{11}\cos\psi_1 A_{12}} \tag{7.38}$$

The differential equations for the costates were found through evaluating equation (7.13). This resulted in

$$\dot{\lambda}_{x1} = -Kf_{1x} + B_1 - \frac{V_1}{A_{11}^3 A_{21}^3}\left(L_1\cos\psi_1 + L_2\sin\psi_1 + L_3\frac{\sin^2\psi_1}{\cos\psi_1}\right) \tag{7.39}$$

$$\dot{\lambda}_{y1} = -Kf_{1y} + B_2 - \frac{V_1}{A_{11}^3 A_{21}^3}\left(L_4\cos\psi_1 + L_5\sin\psi_1 + L_6\frac{\sin^2\psi_1}{\cos\psi_1}\right) \tag{7.40}$$

$$\dot{\lambda}_{x2} = -Kf_{2x} - B_1 - \frac{V_2}{A_{12}^3 A_{22}^3}\left(L_1\cos\psi_2 + L_2\sin\psi_2 + L_3\frac{\sin^2\psi_2}{\cos\psi_2}\right) \tag{7.41}$$

$$\dot{\lambda}_{y2} = -Kf_{2y} - B_2 - \frac{V_2}{A_{12}^3 A_{22}^3}\left(L_4 \cos\psi_2 + L_5 \sin\psi_2 + L_6 \frac{\sin^2\psi_2}{\cos\psi_2} \right) \quad (7.42)$$

where

$$\begin{aligned} L_1 &= -A_{2i}^3 f_{ix} f_{ixx} \lambda_{xi} \\ L_2 &= \left[A_{1i}^2 A_{2i}^2 \left(f_{iy} f_{ixx} + f_{ix} f_{ixy} \right) - A_{1i}^2 f_{ix} f_{iy} \left(f_{ix} f_{ixx} + f_{iy} f_{ixy} \right) - A_{2i}^2 f_{ix}^2 f_{iy} f_{ixx} \right] \lambda_{xi} \\ L_3 &= \left(- A_{1i}^4 f_{iy} f_{ixy} + A_{1i}^2 f_{ix} f_{iy}^2 f_{ixx} \right) \lambda_{yi} \end{aligned} \quad (7.43)$$

$$\begin{aligned} L_4 &= -A_{2i}^3 f_{ix} f_{ixy} \lambda_{xi} \\ L_5 &= \left[A_{1i}^2 A_{2i}^2 \left(f_{iy} f_{ixy} + f_{ix} f_{iyy} \right) - A_{1i}^2 f_{ix} f_{iy} \left(f_{ix} f_{ixy} + f_{iy} f_{iyy} \right) - A_{2i}^2 f_{ix}^2 f_{iy} f_{ixy} \right] \lambda_{xi} \\ L_6 &= \left(- A_{1i}^4 f_{iy} f_{iyy} + A_{1i}^2 f_{ix} f_{iy}^2 f_{ixy} \right) \lambda_{yi} \end{aligned} \quad (7.44)$$

B_1 and B_2 are defined in equations (7.18) and (7.19). Using the technique described above, differential equations for the two heading angles are then found. These can be represented as

$$\dot{\psi}_1 = \frac{A_{11}^3 A_{21} \cos\psi_1 \left(P_1 \sin\psi_1 + P_2 \cos\psi_1 \right) + \lambda_{x1} V_1 f_{1y} P_3}{A_{11}^3 A_{21}^2 \lambda_{x1}} \quad (7.45)$$

$$\dot{\psi}_2 = \frac{V_2 \left[A_{11} A_{12}^2 A_{22} \cos\psi_1 T_1 + \left(A_4 A_{11} \cos\psi_1 + V_1 \lambda_{x1} \right) T_2 \right]}{A_{12}^3 A_{22}^2 \left(A_4 A_{11} \cos\psi_1 + V_1 \lambda_{x1} \right)} \quad (7.46)$$

with

$$\begin{aligned} P_1 &= A_{21} \left(Kf_{1x} - D_1 \right) \\ P_2 &= A_{11}^2 \left(Kf_{1y} - D_2 \right) - f_{1x} f_{1y} \left(Kf_{1x} - D_1 \right) \\ P_3 &= f_{1x} f_{1y} f_{1xx} \sin\psi_1 - A_{11}^2 f_{1xy} \sin\psi_1 + A_{21} f_{1xx} \cos\psi_1 \end{aligned} \quad (7.47)$$

$$\begin{aligned} T_1 &= \left(Kf_{2x} + D_1 \right) \left(f_{2x} f_{2y} \cos\psi_2 - A_{22} \sin\psi_2 \right) - \left(Kf_{2y} + D_2 \right) A_{12}^2 \cos\psi_2 \\ T_2 &= f_{2y} \left(f_{2x} f_{2y} f_{2xx} - A_{12}^2 f_{2xy} \right) \sin\psi_2 + A_{22} f_{2y} f_{2xx} \cos\psi_2 \end{aligned} \quad (7.48)$$

Again, this process results in a system with seven differential equations – the four state equations, the two heading equations and the costate λ_{x1} – with three unknown initial values.

7.2.1 Legendre-Clebsch Necessary Conditions

The Hamiltonian equation for the local tangent plane formulation is

$$H = A_4 + \lambda_{xi}\left(\frac{V_i \cos\psi_i}{A_{1i}} + \frac{V_i f_{ix} f_{iy} \sin\psi_i}{A_{1i} A_{2i}}\right) + \lambda_{yi}\left(\frac{-V_i A_{1i} \sin\psi_i}{A_{2i}}\right) \tag{7.49}$$

and the algebraic expressions for the costates are

$$\begin{aligned}
\lambda_{y1} &= \lambda_{x1}\left(\frac{-A_{21}\sin\psi_1 + f_{1x} f_{1y}\cos\psi_1}{A_{11}^2 \cos\psi_1}\right) \\
\lambda_{x2} &= \frac{-A_{12}\cos\psi_2}{V_2}\left(\frac{A_4 A_{11}\cos\psi_i + V_1\lambda_{x1}}{A_{11}\cos\psi_1}\right) \\
\lambda_{y2} &= \frac{\left(A_4 A_{11}\cos\psi_i + V_1\lambda_{x1}\right)\left(-f_{2x} f_{2y}\cos\psi_2 + A_{22}\sin\psi_2\right)}{V_1 A_{11}\cos\psi_1 A_{12}}
\end{aligned} \tag{7.50}$$

This results in the following matrix for the second partial derivative of the Hamiltonian

$$H_{uu} = \begin{bmatrix} \dfrac{-\lambda_{x1} V_1}{A_{11}\cos\psi_1} & 0 \\ 0 & \dfrac{-\lambda_{x2} V_2}{A_{12}\cos\psi_2} \end{bmatrix} \tag{7.51}$$

In order to satisfy the condition, the following equations must be met.

$$\frac{-\lambda_{xi} V_i}{A_{1i}\cos\psi_i} \geq 0 \tag{7.52}$$

7.2.2 Weierstrass Test

The variational Hamiltonian is again found by substituting the optimal algebraic costate equations into the Hamiltonian equation.

$$H(\psi_1, \psi_2) = A_4 A_1\left[1 - \cos\left(\psi_2^o - \psi_2\right)\right] + \frac{\lambda_{x1} V_1}{\cos\psi_1^o}\left[\cos\left(\psi_1^o - \psi_1\right) - \cos\left(\psi_2^o - \psi_2\right)\right] \tag{7.53}$$

This must satisfy

$$H(\psi_1, \psi_2) \geq 0 \tag{7.54}$$

In Appendix B.2, it is proven that this condition will be satisfied if the following inequalities are true.

$$\left| A_4 A_1 \cos\psi_1^o \right| \geq \left| \lambda_{x1} V_1 \right| \tag{7.55}$$

$$sign(\lambda_{x1}) = -sign(\cos\psi_1) \tag{7.56}$$

7.3 Simplified Equations of Motion – n-Vehicles

For this section, the same process as above is repeated here, but now presented for a n-number of vehicles. First, the simplified equations of motion are used, as described above.

$$\dot{x}_i = V_i \cos\psi_i \tag{7.57}$$

$$\dot{y}_i = V_i \sin\psi_i \tag{7.58}$$

Again, *i* is used to represent each of the n-vehicles. The cost equation, in this case, is represented as

$$J = \sum_{i=1}^{n} \left[\int_0^{t_{fi}} (J_{1i} + J_2) dt \right] \tag{7.59}$$

with

$$J_{1i} = 1 - K + K f_i(x_i, y_i) \tag{7.60}$$

As before, the second part of the cost will be

$$J_2 = W \sum_{i=1}^{n-1} \sum_{j=i+1}^{n} \frac{1}{d_{ij}} \tag{7.61}$$

for collision avoidance flight while, for formation flight, it will be

$$J_2 = W\sum_{i=1}^{n-1}\sum_{j=i+1}^{n}\left(d_{ij} - d_{cij}\right)^2 \tag{7.62}$$

In these equations,

$$d_{ij} = \left(x_i - x_j\right)^2 + \left(y_i - y_j\right)^2 \tag{7.63}$$

Here, the weighing parameter, W_{ij}, can be changed depending on the two vehicles – vehicles i and j – it represents.

The costate differential equations are then represented by the following two equations.

$$\dot{\lambda}_{xi} = -Kf_{ixi} + \sum_{j=i+1}^{n} Bx_{ij} - \sum_{j=1}^{i-1} Bx_{ji} \tag{7.64}$$

$$\dot{\lambda}_{yi} = -Kf_{iyi} + \sum_{j=i+1}^{n} By_{ij} - \sum_{j=1}^{i-1} By_{ji} \tag{7.65}$$

with

$$\begin{aligned} Bx_{ij} &= \frac{2W\left(x_i - x_j\right)}{d_{ij}^2} \\ By_{ij} &= \frac{2W\left(y_i - y_j\right)}{d_{ij}^2} \end{aligned} \tag{7.66}$$

for aircraft avoidance flight or

$$\begin{aligned} Bx_{ij} &= 4W\left(d_{ij} - d_{cij}\right)\left(x_i - x_j\right) \\ By_{ij} &= 4W\left(d_{ij} - d_{cij}\right)\left(y_i - y_j\right) \end{aligned} \tag{7.67}$$

for formation flight. The resulting differential equations for the heading angles are shown in the next two equations, the first of which is applicable for the first n-1 vehicles while the second is for the n^{th} vehicle.

$$\dot{\psi}_j = \frac{\left(\cos^2\psi_j\right)\dot{\lambda}_{y_j} - \left(\cos\psi_j \sin\psi_j\right)\dot{\lambda}_{x_j}}{\lambda_{x_j}} \tag{7.68}$$

$$\dot{\psi}_n = \frac{V_n \prod_{i=1}^{n-1} \cos\psi_i \left[\sin\psi_n \dot{\lambda}_{x_n} - \cos\psi_n \dot{\lambda}_{y_n} \right]}{A_4 \prod_{i=1}^{n-1} \cos\psi_i + \sum_{i=1}^{n-1} \left(\lambda_{x_i} V_i \prod_{\substack{j=1 \\ j\neq i}}^{n-1} \cos\psi_j \right)} \tag{7.69}$$

This process results in a system of 4n-1 differential equations to be solved with 2n-1 unknown initial conditions.

7.3.1 Legendre-Clebsch Necessary Conditions

Similar to the procedure for the two-vehicle problem, the following inequalities are found that must be true in order to satisfy this condition

$$\frac{-\lambda_{xi} V_i}{\cos\psi_i} \geq 0 \tag{7.70}$$

7.3.2 Weierstrass Test

As outlined in the two-vehicle section, the following inequalities must be met to satisfy this condition.

$$\left| A_4 \prod_{i=1}^{n-1} \cos\psi_i^o \right| \geq \left| \sum_{i=1}^{n-1} \left(\lambda_{xi} V_i \prod_{\substack{j=1 \\ j\neq i}}^{n-1} \cos\psi_j^o \right) \right| \tag{7.71}$$

$$sign(\lambda_{xi}) = -sign(\cos\psi_i) \tag{7.72}$$

Equation (7.72) must be met for i=1:n-1.

7.4 Local Tangent Plane Equations of Motion – n-Vehicles

This process is now repeated for a n-number of vehicles using the local tangent plane equations of motion shown above.

$$\dot{x}_i = \frac{V_i \cos\psi_i}{A_{1i}} + \frac{V_i f_{ix_i} f_{iy_i} \sin\psi_i}{A_{1i} A_{2i}} \tag{7.73}$$

$$\dot{y}_i = \frac{-V_i A_{1i} \sin\psi_i}{A_{2i}} \tag{7.74}$$

where

$$\begin{aligned} A_{1i} &= \sqrt{1 + f_{ix_i}^2} \\ A_{2i} &= \sqrt{1 + f_{ix_i}^2 + f_{iy_i}^2} \end{aligned} \tag{7.75}$$

The differential equations for the n-costates are depicted as

$$\dot{\lambda}_{x_i} = D_7 - \frac{\lambda_{x_i} V_i}{A_{1i}^3 A_{2i}^3 \cos\psi_i} \left(D_1 \sin^2\psi_i + D_2 \cos^2\psi_i + D_3 \sin\psi_i \cos\psi_i \right) \tag{7.76}$$

$$\dot{\lambda}_{y_i} = D_8 - \frac{\lambda_{x_i} V_i}{A_{1i}^3 A_{2i}^3 \cos\psi_i} \left(D_4 \sin^2\psi_i + D_5 \cos^2\psi_i + D_6 \sin\psi_i \cos\psi_i \right) \tag{7.77}$$

with

$$D_1 = A_2 \left(f_x f_{xx} f_y^2 - A_1^2 f_y f_{xy} \right)_i \tag{7.78}$$

$$D_2 = \left(- A_2^3 f_x f_{xx} \right)_i \tag{7.79}$$

$$D_3 = A_2^2 \left(A_1^2 f_x f_{xy} - f_x^2 f_{xx} f_y + f_{xx} f_y \right)_i \tag{7.80}$$

$$D_4 = A_2 \left(f_x f_{xy} f_y^2 - A_1^2 f_y f_{yy} \right)_i \tag{7.81}$$

$$D_5 = \left(- A_2^3 f_x f_{xy} \right)_i \tag{7.82}$$

$$D_6 = A_2^2 \left(A_1^2 f_x f_{yy} - f_x^2 f_{xy} f_y + f_{xy} f_y \right)_i \tag{7.83}$$

$$D_7 = -Kf_{ix_i} + \sum_{j=i+1}^{n} Bx_{ij} - \sum_{j=1}^{i-1} Bx_{ji} \tag{7.84}$$

$$D_8 = -Kf_{iy_i} + \sum_{j=i+1}^{n} By_{ij} - \sum_{j=1}^{i-1} By_{ji} \tag{7.85}$$

The heading differential equations are

$$\dot{\psi}_j = \left[\frac{A_1^3 A_2 \cos\psi \left(P_1 \sin\psi + P_2 \cos\psi \right) + \lambda_x V f_y P_3}{A_1^3 A_2^2 \lambda_x} \right]_j \tag{7.86}$$

$$\begin{aligned}
P_{1j} &= A_{2j} \left(Kf_{jx_j} - \sum_{j=i+1}^{n} Bx_{ij} + \sum_{j=1}^{i-1} Bx_{ji} \right) \\
P_{2j} &= A_{1j}^2 \left(Kf_{jy_j} - \sum_{j=i+1}^{n} By_{ij} + \sum_{j=1}^{i-1} By_{ji} \right) - f_{jx_j} f_{jy_j} \left(Kf_{jx_j} - \sum_{j=i+1}^{n} Bx_{ij} + \sum_{j=1}^{i-1} Bx_{ji} \right) \\
P_{3j} &= \left(f_x f_y f_{xx} \sin\psi - A_1^2 f_{xy} \sin\psi + A_2 f_{xx} \cos\psi \right)_j
\end{aligned} \tag{7.87}$$

and

$$\dot{\psi}_n = \frac{V_n \left[A_{1n}^2 A_{2n} T_1 T_4 + T_2 T_3 \right]}{A_{1n}^3 A_{2n}^2 T_3} \tag{7.88}$$

$$\begin{aligned}
T_1 &= \left(Kf_{nx_n} + \sum_{j=1}^{n-1} Bx_{jn} \right) \left(f_x f_y \cos\psi - A_2 \sin\psi \right)_n - \left(Kf_{ny_n} + \sum_{j=1}^{n-1} By_{jn} \right) A_{1n}^2 \cos\psi_n \\
T_2 &= \left[f_y \left(f_x f_y f_{xx} - A_1^2 f_{xy} \right) \sin\psi + A_2 f_y f_{xx} \cos\psi \right]_n \\
T_3 &= A_4 \prod_{i=1}^{n-1} A_{1i} \cos\psi_i + \sum_{i=1}^{n-1} \left(\lambda_{x_i} V_i \prod_{\substack{j=1 \\ j \neq i}}^{n-1} A_{1j} \cos\psi_j \right) \\
T_4 &= \prod_{i=1}^{n-1} A_{1i} \cos\psi_i
\end{aligned} \tag{7.89}$$

As stated before, this results in a system of 4n-1 differential equations to be solved with 2n-1 unknown initial conditions.

7.4.1 Legendre-Clebsch Necessary Conditions

Similar to the procedure for the two-vehicle problem, the following inequalities are found that must be true in order to satisfy this condition

$$\frac{-\lambda_{xi} V_i}{A_{1i} \cos\psi_i} \geq 0 \tag{7.90}$$

7.4.2 Weierstrass Test

As outlined in the two-vehicle section, the following inequalities must be met to satisfy this condition.

$$\left| A_4 \prod_{i=1}^{n-1} \left(A_{1i} \cos\psi_i^o \right) \right| \geq \left| \sum_{i=1}^{n-1} \left(\lambda_{xi} V_i \prod_{\substack{j=1 \\ j \neq i}}^{n-1} \cos\psi_j^o \right) \right| \tag{7.91}$$

$$sign(\lambda_{xi}) = -sign(\cos\psi_i) \tag{7.92}$$

As before, equation (7.92) must be met for i=1:n-1.

CHAPTER 8

MULTIPE VEHICLE RESULTS

This chapter examines results found using the equations for the control of multiple vehicles derived in the last chapter. Results will be presented for the cases when 2, 3 and 4 vehicles are to be controlled simultaneously in a variety of situations. These include the simple case of vehicle avoidance, a case of a faster vehicle passing slower vehicles and finally the case of formation flight.

8.1 2-Vehicle Results

In this section, three different sets of results are shown for two-vehicle control. The first two cases are different situations using the aircraft avoidance formulation. The third case examines a formation flight situation.

The first set of trajectories presented considers a case of aircraft avoidance. Here, two vehicles are operating in the same area and must avoid each other. The terrain used is a flat plain; in this case the local tangent plane equations of motion will reduce to the simplified equations of motion. In addition, the minimum time and terrain masking variations will be identical. Two different sets of trajectories are shown for this case. The first is a nominal case when no correction for multiple vehicles is made. The second is using the equations from Chapter 7 that account for other vehicles in the area. In these plots, the blue line represents vehicle 1 while the green line represents vehicle 2. The starting positions and ending positions are marked with red circles and xs, respectively. The red star marks the position when the two vehicles are at their closest point.

First, in Figure 8.1, the nominal results are shown for this situation. Here are the optimal trajectories for two vehicles flying alone in the area, using the equations of motion from Chapter 2. As expected, these trajectories are straight lines. Figure 8.2 depicts the distance between the two vehicles at all times. It can be seen that, if allowed to fly these trajectories, the two aircraft would collide.

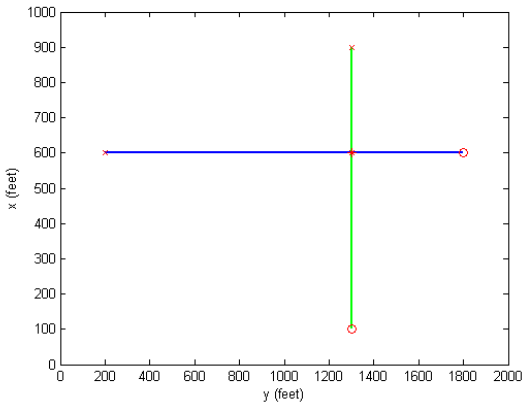

Figure 8.1: Nominal trajectories with no correction for multiple vehicles.

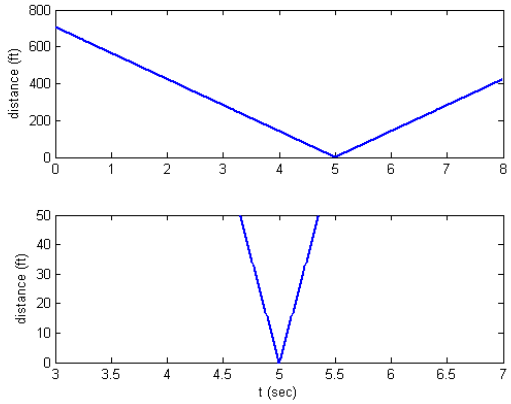

Figure 8.2: Distance between the two vehicles at all time.

Figure 8.3 depicts the trajectories found for the two vehicles when the correction is made for multiple vehicles in the area, as in the equations in Chapter 7. Figure 8.4

depicts the distance between the two vehicles throughout the flights. In this case, the minimum distance between the vehicles is about 247 feet. The heading angles for the two vehicles are depicted in Figure 8.5.

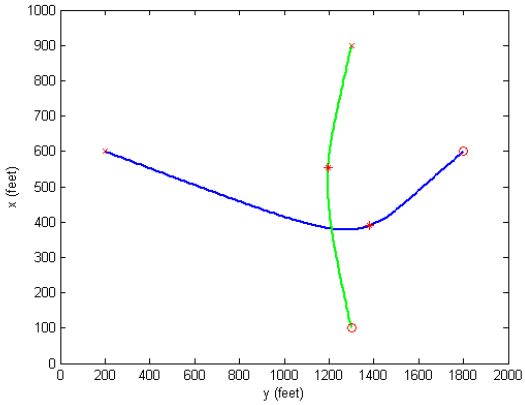

Figure 8.3: Trajectories for two vehicles with aircraft avoidance formulation.

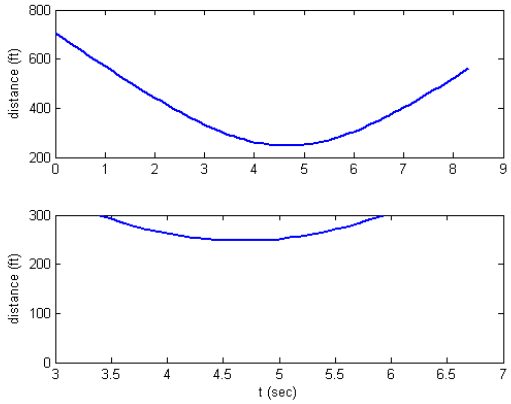

Figure 8.4: Distance between the two vehicles at all time.

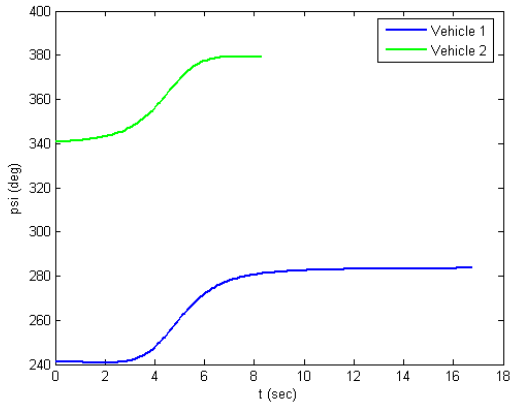

Figure 8.5: Controls for aircraft avoidance flight.

The results from the second variation analysis can be seen in Figure 8.5. In the last chapter it was shown that, in order for the Legendre-Clebsch condition to be satisfied, the following inequalities must be satisfied.

$$\frac{-\lambda_{xi} V_i}{A_{1i} \cos\psi_i} \geq 0 \tag{8.1}$$

In addition, the following equations must be satisfied at all times in order for the Weierstrass test to hold.

$$W = \left| A_4 A_1 \cos\psi_1^o \right| - \left| \lambda_{x1} V_1 \right| \geq 0 \tag{8.2}$$

$$sign(\lambda_{x1}) = -sign(\cos\psi_1) \tag{8.3}$$

Figure 8.6 depicts the plots of the Legendre-Clebsch function with respect to time, which is always positive. Figure 8.7 depicts the plots for the two inequalities for the Weiertrass test. On the right is the inequality from the Weierstrass tess – which is positive at all time – and on the left is the sign functions.

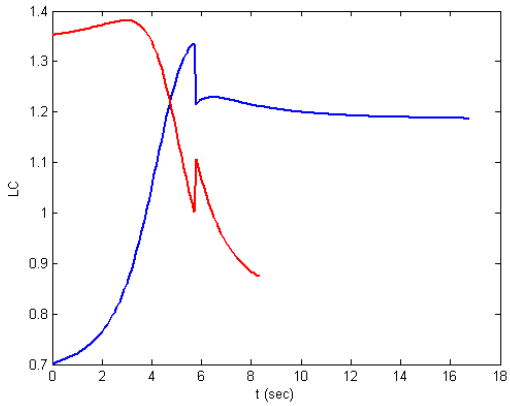

Figure 8.6: Results from Legendre-Clebsch test.

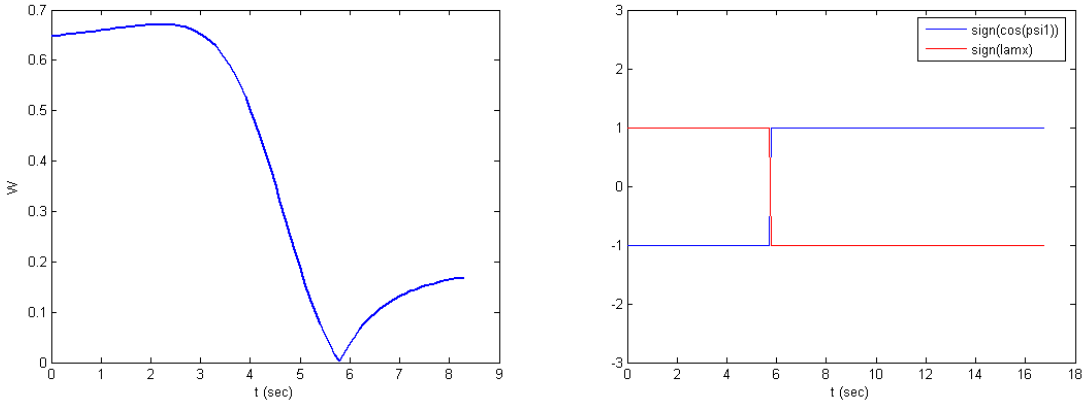

Figure 8.7: Results from Weierstrass test.

The second case examined for this formulation is a situation when a faster vehicle must pass a slower vehicle. These trajectories are shown in Figure 8.8. In this case, the starting positions, (500, 100) and (500, 0), and ending positions, (500, 1700) and (500, 1900), for both vehicles are in a line with each other. Here, the faster vehicle starts behind the slower vehicle, so they would collide if a straight line trajectory were flown by each of the vehicles. It can be seen that each vehicles path curves slightly away from the trajectory of the other vehicle. Figure 8.9 shows the distance between the two vehicles.

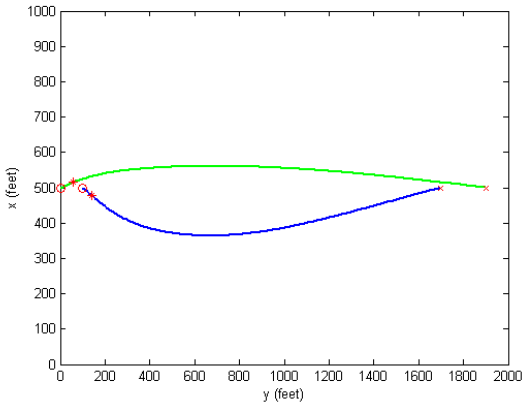

Figure 8.8: Optimal trajectories for passing.

The closest position during the flight is just after the start of the flight as the aircraft are curving away from each other and is about 93 feet. The heading angles for each vehicle is depicted in Figure 8.10.

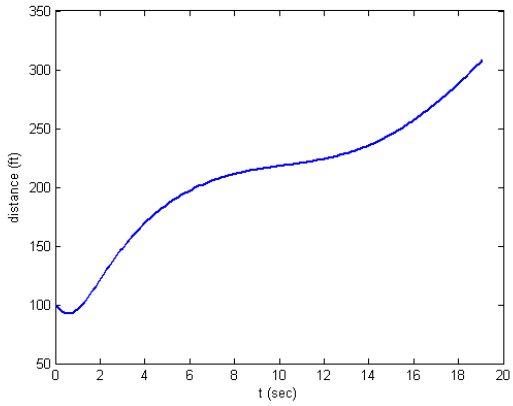

Figure 8.9: Distance between the two vehicles at all time.

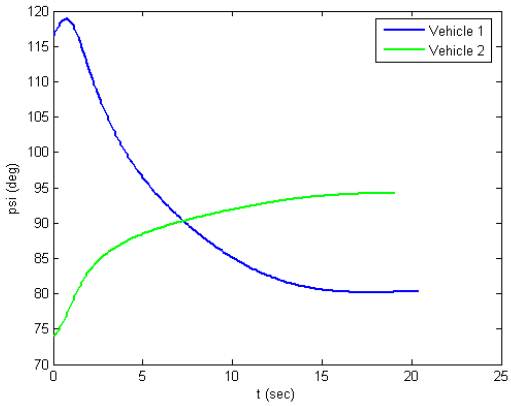

Figure 8.10: Controls for passing.

Figures 8.11 and 8.12 contain the three plots for the analysis of the second variation tests whose inequalities are given in (8.1) - (8.3). The inequality from the Legendre-Clebsch test can be seen plotted in Figure 8.11 while the functions needed for the Weierstrass test can be seen in Figure 8.12. It can be seen that they are all satisfied for all time.

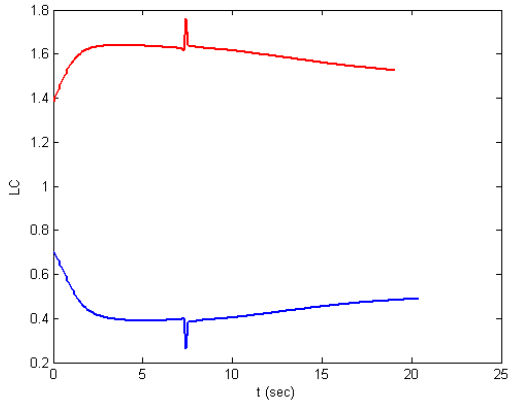

Figure 8.11: Results from Legendre-Clebsch test.

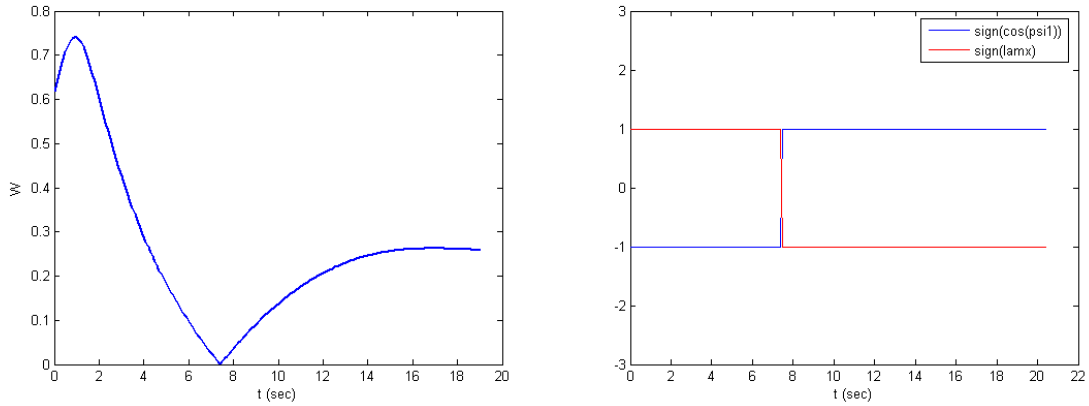

Figure 8.12: Results from Weierstrass test.

The final result shown considers the case of formation flight. For this situation, the terrain of a flat plain with a single hill was used and the terrain masking formulation was used. The trajectories for the two vehicles can be seen in Figure 8.13. The plot on the left shows the 3D view of the terrain and trajectories while the plot on the right contains an overhead view. It can be seen that the vehicles stay parallel to each other throughout the flight around the hill. The plot of the heading angles for this flight can be seen in Figure 8.14. Figures 8.15 and 8.16 depict the plots for the second variation analysis, a described earlier, which are all satisfied.

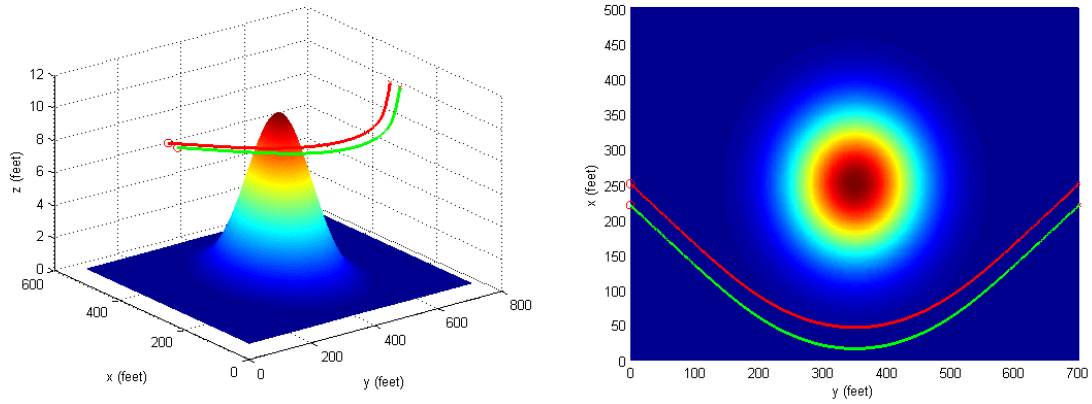

Figure 8.13: Trajectories for two vehicles in formation flight.

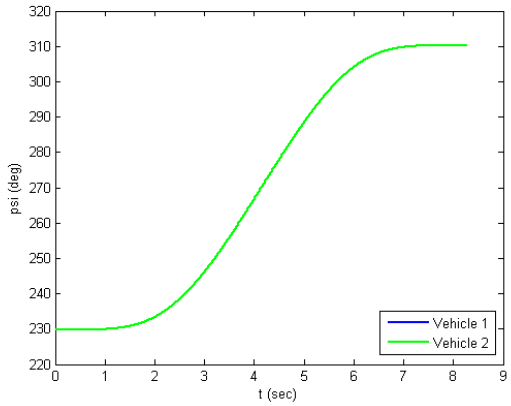

Figure 8.14: Controls for formation flight.

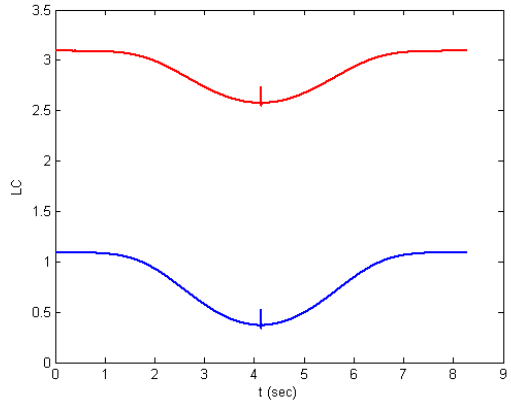

Figure 8.15: Results from Legendre-Clebsch test.

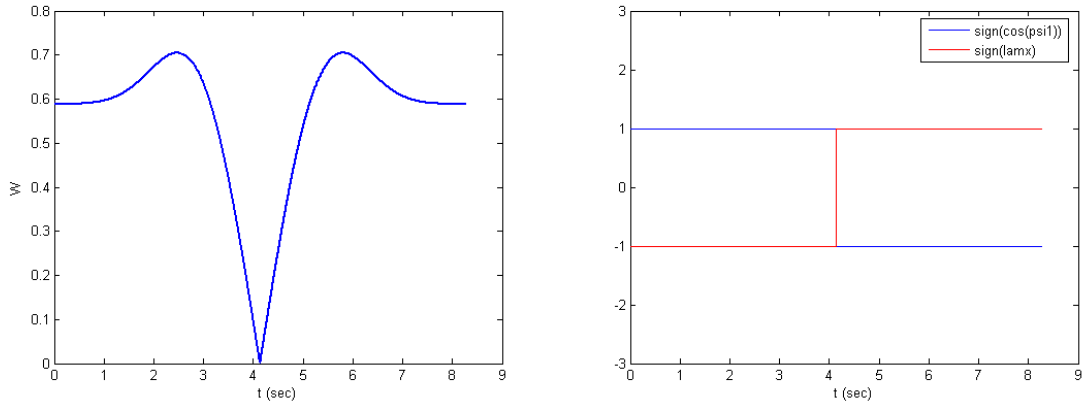

Figure 8.16: Results from Weierstrass test.

8.2 3-Vehicle Results

This section presents the results for two cases with 3 vehicles. The first represents the case of aircraft avoidance in a given area on a flat plane. The second examines terrain masking formation flight.

Figure 8.17 depicts the trajectories for the aircraft avoidance flight. The blue line represents vehicle 1, the green line represents vehicle 2 and the red line represents vehicle 3. The starting and ending positions for each of these flights are depicted by red circles and xs, respectively. Figure 8.18 depicts the positions of the vehicles with respect to each

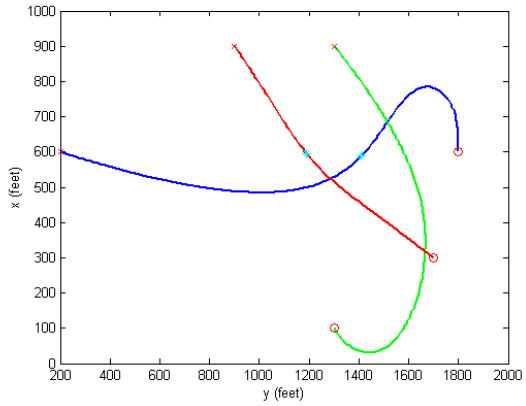

Figure 8.17: Trajectories for aircraft avoidance.

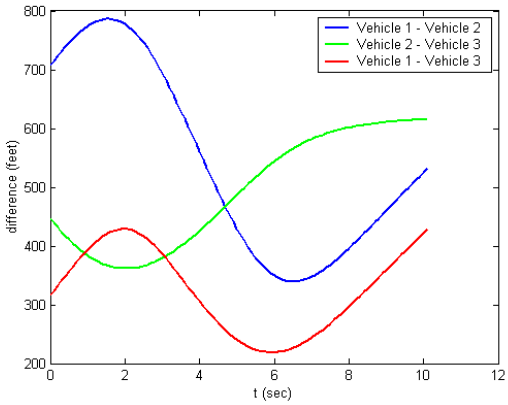

Figure 8.18: Distances between vehicles at all times.

other for the entire time of the flight. It can be seen that the closest point between the vehicles is about 219 feet between vehicles one and two; this point in marked in Figure 8.17 with light blue stars. The heading angles for these flights are plotted in Figure 8.19.

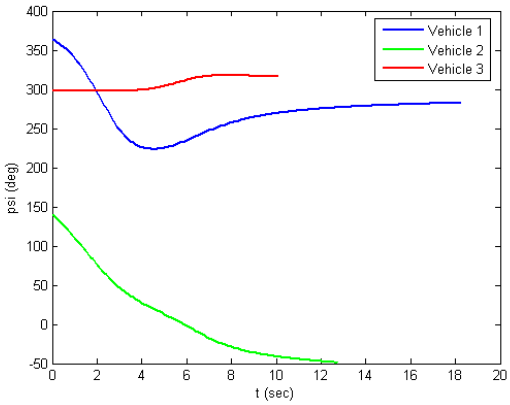

Figure 8.19: Controls for aircraft avoidance flight.

The results from the second variation analysis for this problem are depicted in Figures 8.20 and 8.21. In Chapter 7, the necessary equations to meet the second variation tests are stated as follows for three vehicles.

$$\frac{-\lambda_{xi} V_i}{A_{1i} \cos\psi_i} \geq 0 \tag{8.4}$$

$$W = \left| A_4 A_{11} A_{12} \cos\psi_1^o \cos\psi_2^0 \right| - \left| \lambda_{x1} V_1 \cos\psi_2^0 + \lambda_{x2} V_2 \cos\psi_1^0 \right| \geq 0 \tag{8.5}$$

$$\begin{aligned} sign(\lambda_{x1}) &= -sign(\cos\psi_1) \\ sign(\lambda_{x2}) &= -sign(\cos\psi_2) \end{aligned} \tag{8.6}$$

The inequalities in (8.4) are necessary for the Legendre-Clebsch condition while (8.5) and (8.6) must be satisfied for the Weierstrass test. The plots of the functions stated in the inequalities in (8.4) and (8.5) can be seen in Figure 8.20. The plot on the left represents the Legendre-Clebsh inequalities and the plot on the right contains the

Weierstrass inequality. The plots of the signs on the variables in (8.6) are in Figure 8.21. In all cases, it can be seen that the requirements are satisfied.

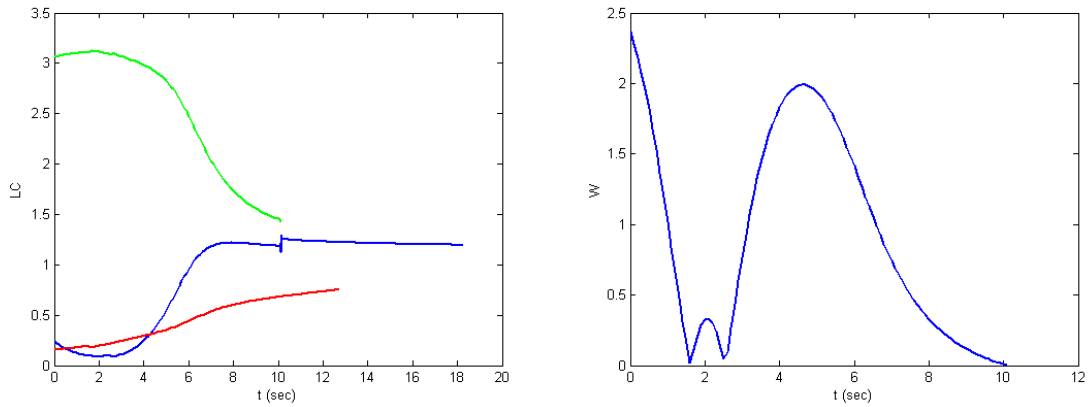

Figure 8.20: Inequalities from second variation tests.

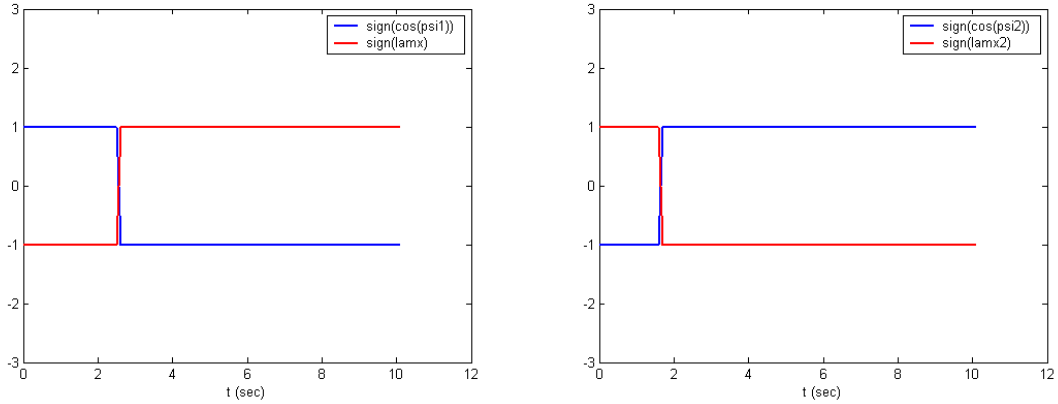

Figure 8.21: Plots of signs of variables for Weierstrass test.

The second case presented consists of a formation flight. These trajectories can be seen in Figure 8.22. The 3D view can be seen in the plot on the left while the over head view is in the plot on the right. Here, the three vehicles remain in a triangle formation throughout the entire flight. The controls for these flights can be seen in Figure 8.23.

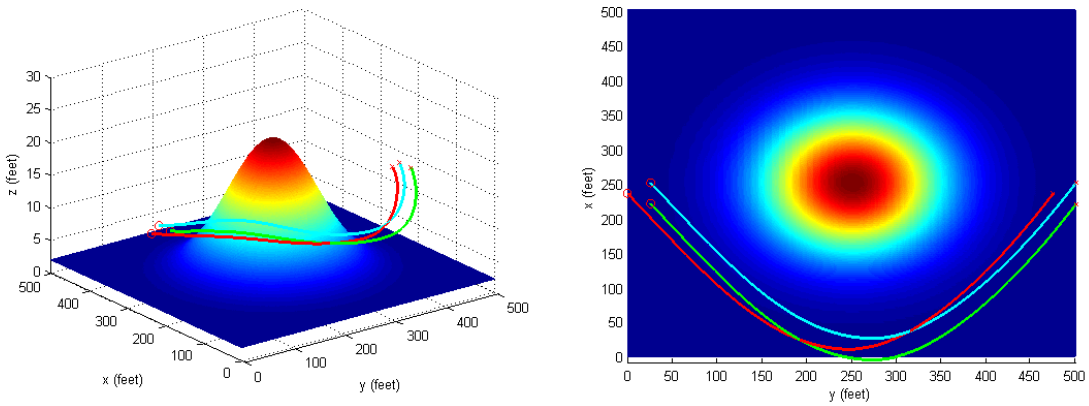

Figure 8.22: Trajectories for formation flight of three vehicles.

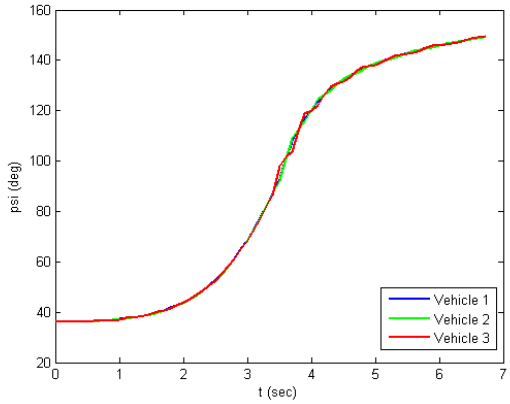

Figure 8.23: Controls for formation flight.

The analysis of the second variation tests are depicted in Figures 8.24 and 8.25. In Figure 8.24, the functions from the inequalities from equations 8.4 and 8.5 for the Legendre-Clebsch condition (on the left) and the Weierstrass test (on the right) are plotted. In each case, it can be seen that the functions are positive at all time. The signs of the variables for the Weierstrass test, from equation 8.6, can be seen in Figure 8.25.

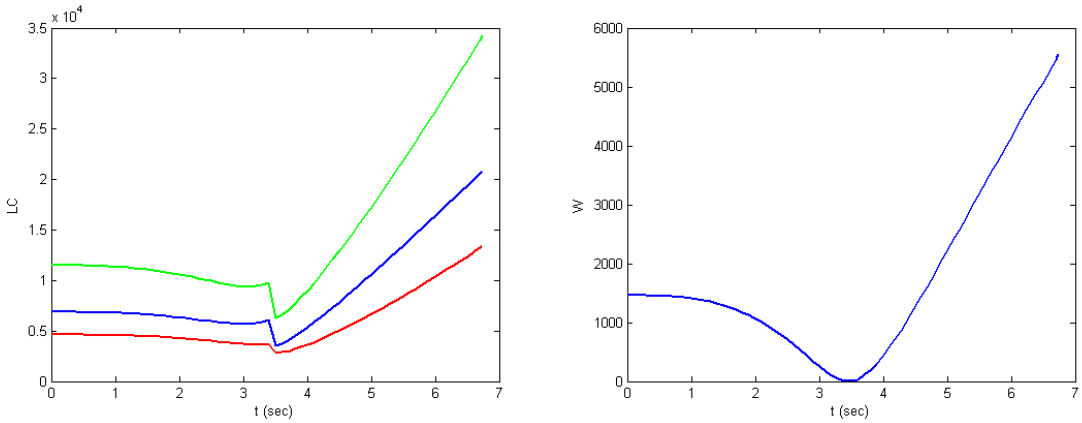

Figure 8.24: Inequalities from second variation tests.

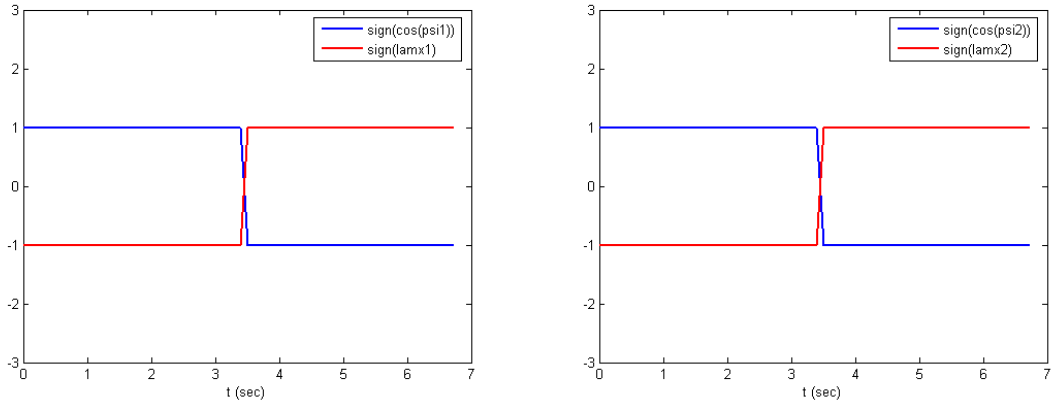

Figure 8.25: Plots of signs of variables for Weierstrass test.

8.3 4-Vehicle Results

As with the 3-vehicle case, two sets of results will be presented here for the coordinated flight of four vehicles – one for aircraft avoidance and one for formation flight. Figure 8.26 shows the trajectories for the aircraft avoidance flight of four vehicles. The blue, green, red and magenta lines represent vehicles one, two, three and four respectively. Figure 8.27 contains the plots of the distance between each set of vehicles at all time. It can be seen that the minimum distance is 186 feet between vehicles two

and four; this point is marked on Figure 8.26 with a red star. The heading angles for each of these vehicles for this flight can be seen in Figure 8.28.

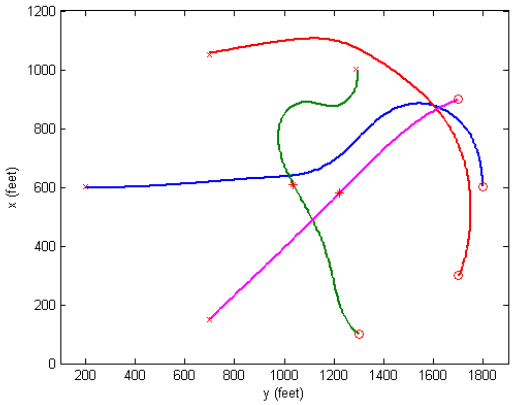

Figure 8.26: Trajectories for aircraft avoidance flight of four vehicles.

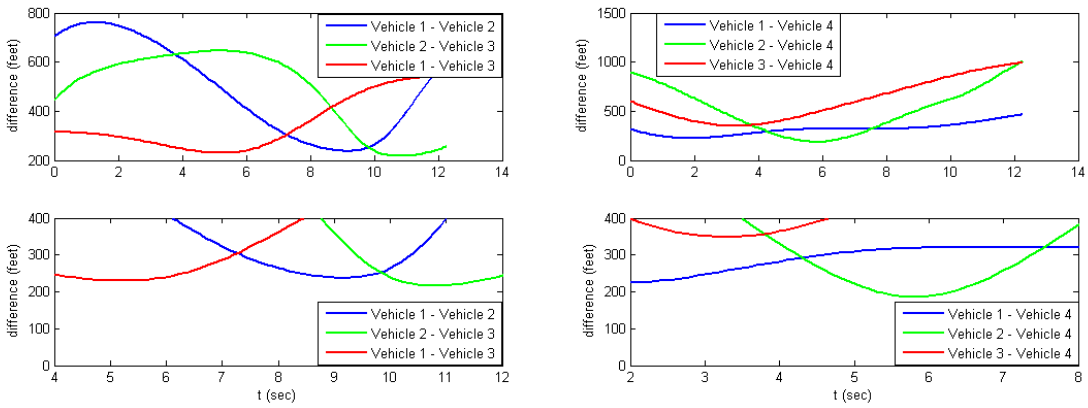

Figure 8.27: Distances between each set of vehicles.

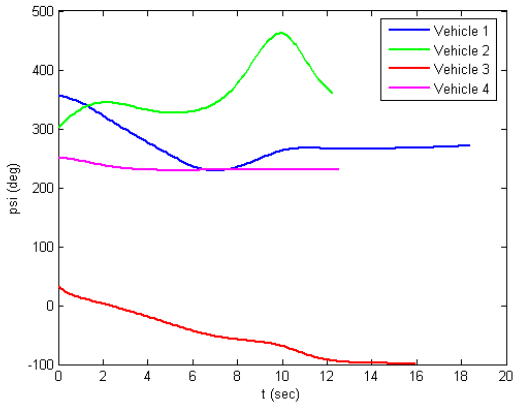

Figure 8.28: Controls for aircraft avoidance flight.

The analysis of the second variation is portrayed in Figures 8.29 and 8.30. For this formulation, the equations that must be satisfied are as follows.

$$\frac{-\lambda_{xi} V_i}{A_{1i} \cos\psi_i} \geq 0 \tag{8.7}$$

$$W = \left| A_4 \prod_{i=1}^{3} \left(A_{1i} \cos\psi_i^o \right) \right| - \left| \sum_{i=1}^{3} \left(\lambda_{xi} V_i \prod_{\substack{j=1 \\ j \neq i}}^{3} \cos\psi_j^o \right) \right| \geq 0 \tag{8.8}$$

$$sign(\lambda_{xi}) = -sign(\cos\psi_i); \quad i = 1:3 \tag{8.9}$$

The inequalities in (8.7) is necessary for the Legendre-Clebsch conditions to be satisfied while the inequality in (8.8) and the equations in (8.9) are required for the Weierstrass test to be satisfied. These inequalities are depicted in Figure 8.29 and the signs of the variables from (8.9) are shown in Figure 8.30. It can be seen that all these equations are satisfied for all time.

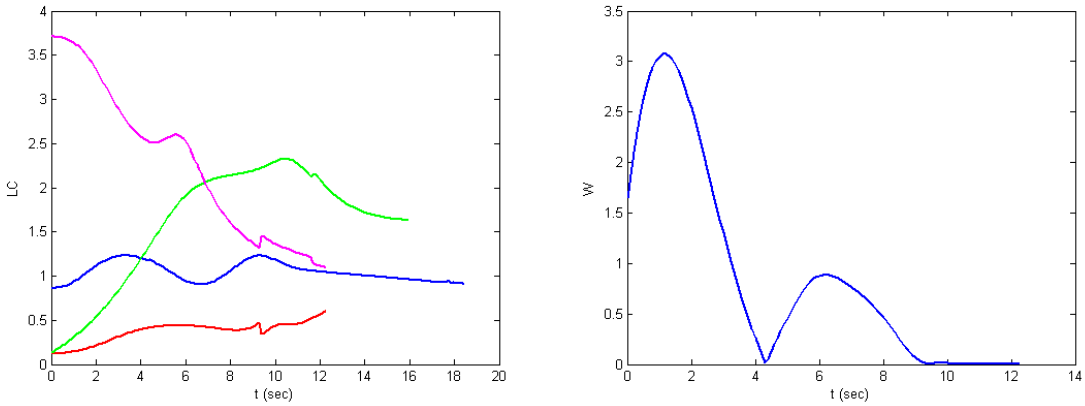

Figure 8.29: Inequalities from second variation tests.

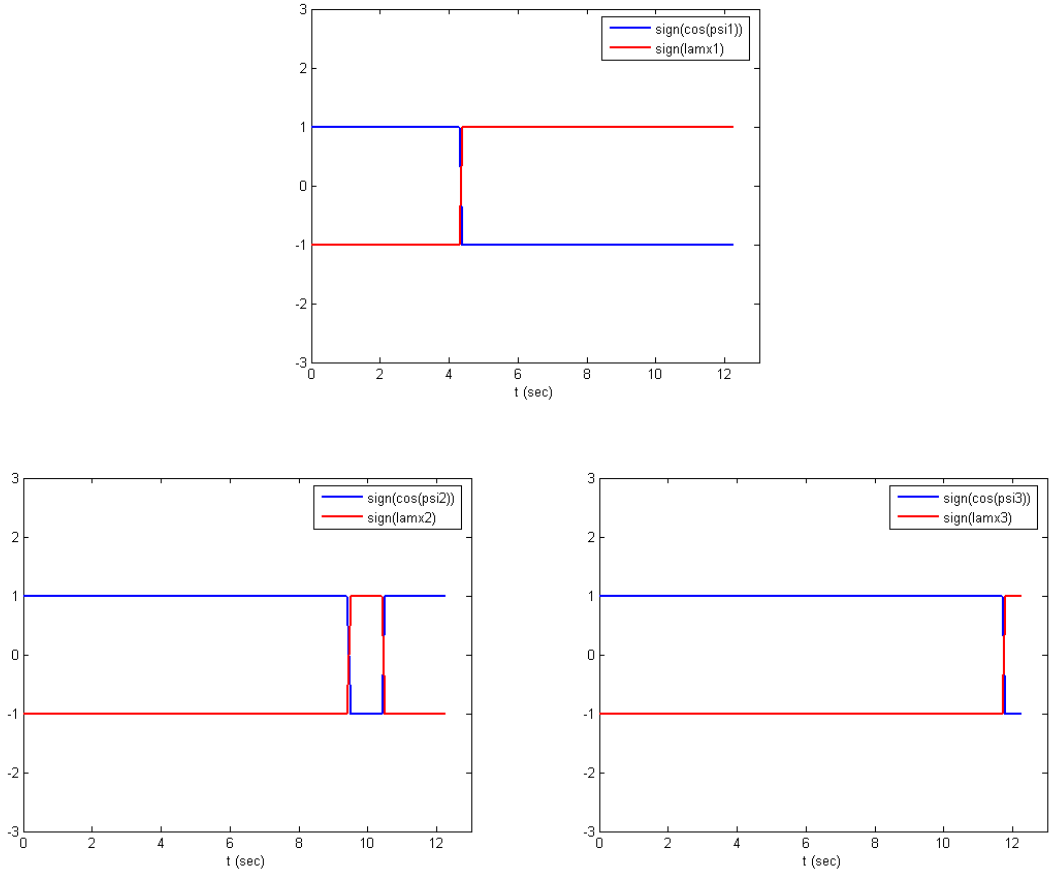

Figure 8.30: Plots of signs of variables for Weierstrass test.

The last set of trajectories depicted is for the case of formation flight of four vehicles. This can be seen in Figure 8.31. In this case, the four aircraft remain in a square formation for the entire flight around the hill. The heading angles for these flights can be seen in Figure 8.32. The corresponding second variation analysis is depicted in Figures 8.33 and 8.34. The inequalities from the functions in (8.7) and (8.8) are shown in Figure 8.33 with the Legendre-Clebsch inequality on the left and the Weierstrass test inequality on the right. The signs of the variables necessary for the Weierstrass test, as

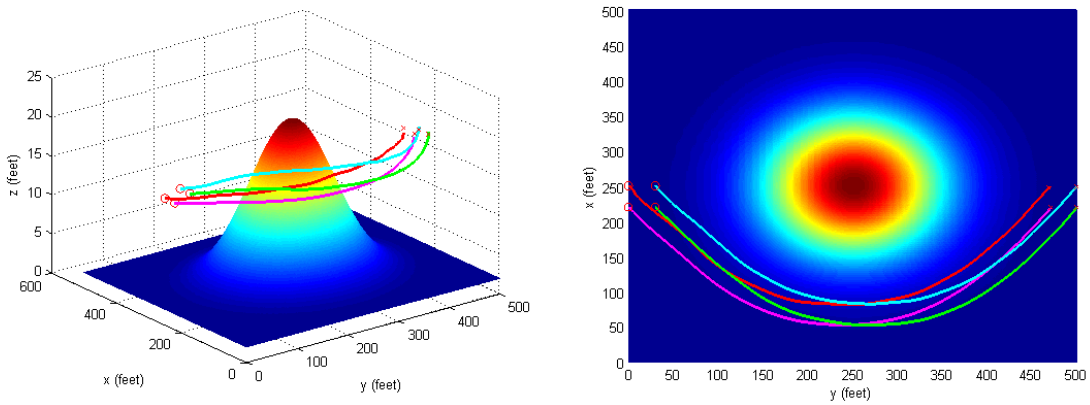

Figure 8:31: Trajectories of formation flight of four vehicles.

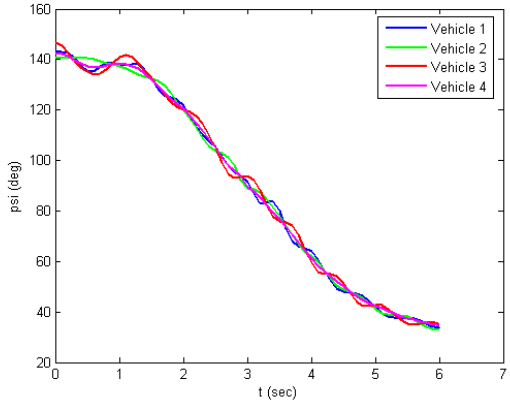

Figure 8.32: Controls for formation flight.

represented in equation (8.9) are shown in Figure 8.34. It can be seen that all the conditions are satisfied for all time.

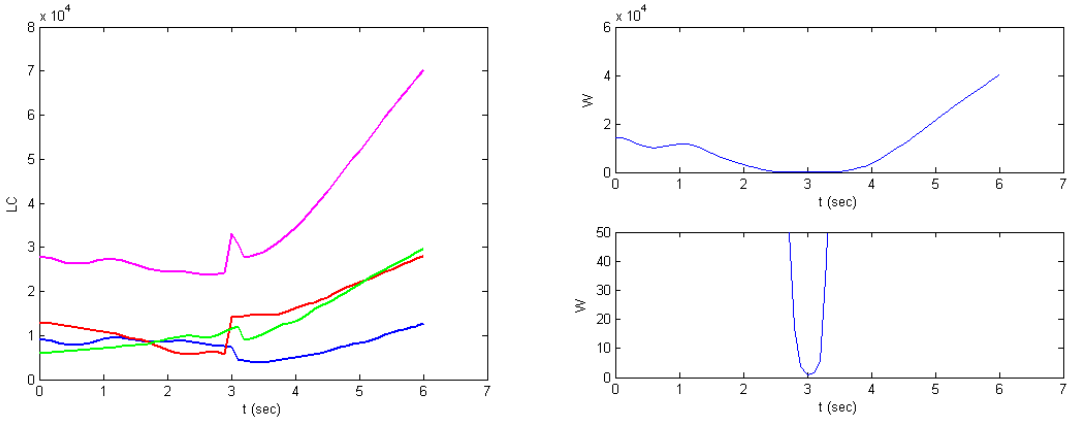

Figure 8.33: Inequalities from second variation tests.

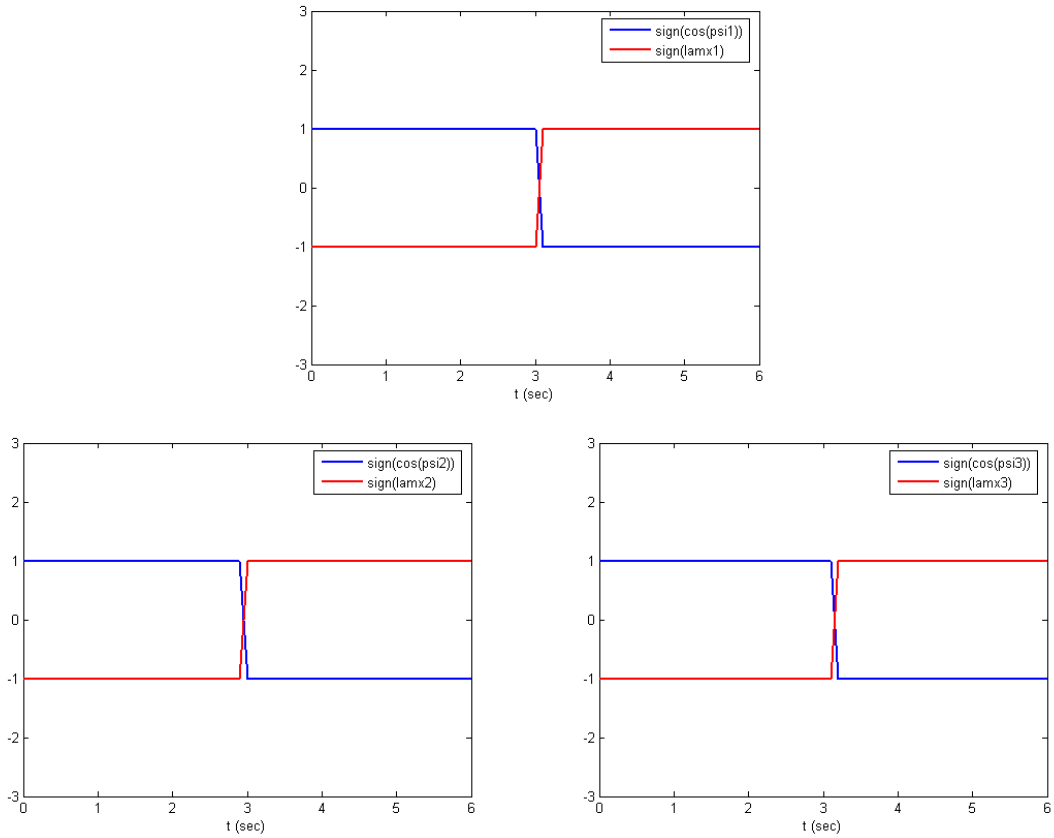

Figure 8.34: Plots of signs of variables for Weierstrass test.

CHAPTER 9

MULTIPLE VEHICLE 3D EQUATIONS OF MOTION

This section incorporates the 3D constant velocity equations of motion detailed in Chapter 4 with the multiple vehicle formulation detailed in Chapter 7. As shown earlier, using the 3D equations of motion provide a more realistic solution to the terrain following problem. First the reduced order formulation for the problem will be derived in detail for the two-vehicle problem, then the n-vehicle equations will be derived.

9.1 Two-vehicle formulation

For this formulation, the 3D equations of motion are used, as described before in equations (4.1) to (4.3).

$$\dot{x}_i = V_i \cos\gamma_i \cos\psi_i \tag{9.1}$$

$$\dot{y}_i = V_i \cos\gamma_i \sin\psi_i \tag{9.2}$$

$$\dot{z}_i = V_i \sin\gamma_i \tag{9.3}$$

Here, with *i* equal to one, these equations depict the equations of motion for vehicle 1 while with *i* equal to two, they represent the equations of motion for vehicle 2.

The cost equation used for this problem is

$$J = \int_0^{t_{f1}} \left(C_{11} + C_{21} + C_3\right) dt + \int_0^{t_{f2}} \left(C_{12} + C_{22} + C_3\right) dt \tag{9.4}$$

with a separate integral for each vehicle, as discussed in Chapter 7. There are three distinct portions of the cost equation for each vehicle. First

$$C_{1i} = 1 - K + Kf_i\left(x_i, y_i\right) \tag{9.5}$$

controls the amount of optimality with respect to terrain masking or minimum time as described in earlier chapters. The second part is

$$C_{2i} = W_{1i} Z_i^2 \tag{9.6}$$

with

$$Z_i = z_i - \left[f_i(x_i, y_i) + h_{ci} \right] \tag{9.7}$$

This section is for maintaining flight near the desired constant altitude as discussed in Chapter 4. The third part of the cost, as in Chapter 7, is determined by either

$$C_3 = \frac{W_2}{d} \tag{9.8}$$

for aircraft avoidance or

$$C_3 = W_2 (d - d_c)^2 \tag{9.9}$$

for formation flight. In both these equations,

$$d = (x_1 - x_2)^2 + (y_1 - y_2)^2 \tag{9.10}$$

W_1 and W_2 are weighing parameters supplied by the user.

The Hamiltonian equation for this system can be written as

$$\begin{aligned} H &= A_4 + \sum_{i=1}^{2} \left[\lambda_{xi} V_i \cos\gamma_i \cos\psi_i + \lambda_{yi} V_i \cos\gamma_i \sin\psi_i + \lambda_{zi} V_i \sin\gamma_i \right] \\ A_4 &= \sum_{\substack{i=1 \\ t \le t_{fi}}}^{2} (C_{1i} + C_{2i} + C_3) \end{aligned} \tag{9.11}$$

The costate variables for the six states are given by λ_{xi}, λ_{yi} and λ_{zi}. There are now four optimality conditions for the problem, which can be written as

$$\begin{aligned} H_{\psi i} &= 0 \\ H_{\gamma i} &= 0 \end{aligned} \tag{9.12}$$

Evaluating the equations in (9.12) results in the following four relationships.

$$\lambda_{yi} = \lambda_{xi} \frac{\sin\psi_i}{\cos\psi_i}$$
$$\lambda_{zi} = \lambda_{xi} \frac{\sin\gamma_i}{\cos\psi_i \cos\gamma_i} \tag{9.13}$$

As before, since the Hamiltonian equation is not explicitly dependent on time, it will equal zero at all times. Using this fact and the equations in (9.11) and (9.13), the following five algebraic expressions are found for the costates

$$\lambda_{y1} = \lambda_{x1} \frac{\sin\psi_1}{\cos\psi_1} \tag{9.14}$$

$$\lambda_{z1} = \lambda_{x1} \frac{\sin\gamma_1}{\cos\psi_1 \cos\gamma_1} \tag{9.15}$$

$$\lambda_{x2} = \frac{-\cos\gamma_2 \cos\psi_2}{V_2} \left(\frac{A_4 \cos\gamma_1 \cos\psi_1 + \lambda_{x1} V_1}{\cos\psi_1 \cos\gamma_1} \right) \tag{9.16}$$

$$\lambda_{y2} = \frac{-\cos\gamma_2 \sin\psi_2}{V_2} \left(\frac{A_4 \cos\gamma_1 \cos\psi_1 + \lambda_{x1} V_1}{\cos\gamma_1 \cos\psi_1} \right) \tag{9.17}$$

$$\lambda_{z2} = \frac{-\sin\gamma_2}{V_2} \left(\frac{A_4 \cos\gamma_1 \cos\psi_1 + \lambda_{x1} V_1}{\cos\gamma_1 \cos\psi_1} \right) \tag{9.18}$$

Differential equations for the costates can be found by taking the partial derivatives of the Hamiltonian equation as shown below.

$$\dot{\lambda}_{xi} = -H_{xi}$$
$$\dot{\lambda}_{yi} = -H_{yi} \tag{9.19}$$
$$\dot{\lambda}_{zi} = -H_{zi}$$

This results in the following six differential equations.

$$\dot{\lambda}_{x1} = -Kf_{1x1} + B_x + 2W_{11} Z_1 f_{1x1} \tag{9.20}$$

$$\dot{\lambda}_{y1} = -Kf_{1y1} + B_y + 2W_{11} Z_1 f_{1y1} \tag{9.21}$$

$$\dot{\lambda}_{z1} = B_z + 2W_{11}Z_1 \tag{9.22}$$

$$\dot{\lambda}_{x2} = -Kf_{2x2} - B_x + 2W_{12}Z_2 f_{2x2} \tag{9.23}$$

$$\dot{\lambda}_{y2} = -Kf_{2y2} - B_y + 2W_{12}Z_2 f_{2y2} \tag{9.24}$$

$$\dot{\lambda}_{z2} = -B_z - 2W_{12}Z_2 \tag{9.25}$$

with

$$\begin{aligned} B_x &= \frac{2W_2(x_1 - x_2)}{d^2} \\ B_y &= \frac{2W_2(y_1 - y_2)}{d^2} \\ B_z &= \frac{2W_2(z_1 - z_2)}{d^2} \end{aligned} \tag{9.26}$$

for vehicle avoidance flight or

$$\begin{aligned} B_x &= 4W_2(d - d_c)(x_1 - x_2) \\ B_y &= 4W_2(d - d_c)(y_1 - y_2) \\ B_z &= 4W_2(d - d_c)(z_1 - z_2) \end{aligned} \tag{9.27}$$

for formation flight.

Next, the time derivative of equation (9.14) is taken and set equal to its counterpart in equation (9.21). Rearranging this expression will result in a differential equation for ψ_1.

$$\dot{\psi}_1 = \frac{\cos\psi_1\left[(2W_1Z_1 - K)\left(f_{1y1}\cos\psi_1 - f_{1x1}\sin\psi_1\right) - B_x\sin\psi_1 + B_y\cos\psi_1\right]}{\lambda_{x1}} \tag{9.28}$$

Then the time derivative is determined for equation (9.15) and set equal to its corresponding differential equation in (9.22) to derive the differential equation for the flight path angle of vehicle 1.

$$\dot{\gamma}_1 = \frac{\cos\psi_1 \cos\gamma_1 \left[\dot{\lambda}_{z1} \cos\gamma_1 - \sin\gamma_1 \left(\dot{\lambda}_{y1} \sin\psi_1 + \dot{\lambda}_{x1} \cos\psi_1\right)\right]}{\lambda_{x1}} \tag{9.29}$$

Next, this is repeated with equations (9.18) and (9.25) to find the differential equation for γ_2 then with either (9.16) and (9.24) or equations (9.17) and (9.25) to determine a differential equation for ψ_2.

$$\dot{\gamma}_2 = \frac{V_2 \cos\psi_1 \cos\gamma_1 \left[-\dot{\lambda}_{z2} \cos\gamma_2 + \sin\gamma_2 \left(\dot{\lambda}_{y2} \sin\psi_2 + \dot{\lambda}_{x2} \cos\psi_2\right)\right]}{A_4 \cos\gamma_1 \cos\psi_1 + V_1 \lambda_{x1}} \tag{9.30}$$

$$\dot{\psi}_2 = \frac{V_2 \cos\gamma_1 \cos\psi_1 \left[\dot{\lambda}_{x2} \sin\psi_2 - \dot{\lambda}_{y2} \cos\psi_2\right]}{\cos\gamma_2 \left(A_4 \cos\gamma_1 \cos\psi_1 + V_1 \lambda_{x1}\right)} \tag{9.31}$$

This yields a system with eleven differential equations – the six state equations, the two heading angle equations, two flight path angle equations, and the costate λ_{x1} – with five unknown initial values.

9.1.1 Legendre-Clebsch Necessary Conditions

For this formulation, the Hamiltonian equation is seen in equation (9.11) and the costates are in equations (9.14) – (9.18). There are four controls for this problem, represented by the vector

$$u = \begin{bmatrix} \psi_1 \\ \psi_2 \\ \gamma_1 \\ \gamma_2 \end{bmatrix} \tag{9.32}$$

Taking the second partial derivative of the Hamiltonian and substituting in the algebraic expressions for the costates will result in the following matrix

$$H_{uu} = \begin{bmatrix} \dfrac{-\lambda_{x1} V_1 \cos\gamma_1}{\cos\psi_1} & 0 & 0 & 0 \\ 0 & (\cos\gamma_1)^2 H_1 & 0 & 0 \\ 0 & 0 & \dfrac{-\lambda_{x1} V_1}{\cos\psi_1 \cos\gamma_1} & 0 \\ 0 & 0 & 0 & H_1 \end{bmatrix} \tag{9.33}$$

with

$$H_1 = \frac{A_4 \cos\gamma_1 \cos\psi_1 + \lambda_{x1} V_1}{\cos\gamma_1 \cos\psi_1} \tag{9.34}$$

Since $cos\gamma_1$ is always positive, this matrix will be nonnegative definite provided the following two inequalities are satisfied

$$\begin{aligned} &\frac{-\lambda_{x1} V_1}{\cos\psi_1 \cos\gamma_1} \geq 0 \\ &H_1 \geq 0 \end{aligned} \tag{9.35}$$

which is always positive, thus satisfying the condition.

9.1.2 Weierstrass Test

Substituting the optimal costate equations into the Hamiltonian equation will result in the following expression for the variational Hamiltonian.

$$\begin{aligned} &H(\psi_1, \psi_2) = A_4 \cos\psi_1^o \cos\gamma_1^o [1 - C_2] + \lambda_{x1} V [C_1 - C_2] \geq 0 \\ &C_i = \cos\gamma_i \cos\gamma_i^o \cos(\psi_i - \psi_i^o) + \sin\gamma_i \sin\gamma_i^o \end{aligned} \tag{9.36}$$

In Appendix B.2, it is proven that this condition will be satisfied if the following conditions are true.

$$\left| A_4 \cos\psi_1^o \cos\gamma_1^o \right| \geq \left| \lambda_{x1} V_1 \right| \tag{9.37}$$

$$sign(\lambda_{x1}) = -sign(\cos\psi_1) \tag{9.38}$$

9.2 n-vehicle formulation

This section repeats the derivation in the last section, with an expansion to n-vehicles, instead of just two vehicles. The equations of motion are still

$$\dot{x}_i = V_i \cos\gamma_i \cos\psi_i \tag{9.39}$$

$$\dot{y}_i = V_i \cos\gamma_i \sin\psi_i \tag{9.40}$$

$$\dot{z}_i = V_i \sin\gamma_i \tag{9.41}$$

Here, though, *i* can equal each number from 1 to n.

The cost equation used for this problem is now

$$J = \sum_{i=1}^{n}\left[\int_0^{t_{fi}} \left(C_{1i} + C_{2i} + C_3\right) dt\right] \tag{9.42}$$

with

$$C_{1i} = 1 - K + Kf_i\left(x_i, y_i\right) \tag{9.43}$$

$$C_{2i} = W_{1i} Z_i^2 \tag{9.44}$$

and

$$C_3 = W_2 \sum_{i=1}^{n-1}\sum_{j=i}^{n} \frac{1}{d_{ij}} \tag{9.45}$$

for aircraft avoidance or

$$C_3 = W_2 \sum_{i=1}^{n-1}\sum_{j=i}^{n} \left(d_{ij} - d_{cij}\right)^2 \tag{9.46}$$

for formation flight. In both these equations,

$$d_{ij} = \left(x_i - x_j\right)^2 + \left(y_i - y_j\right)^2 \tag{9.47}$$

The corresponding costate differential equations for this problem will be

$$\dot{\lambda}_{xi} = -Kf_{ixi} + \sum_{j=i+1}^{n} B_{xij} - \sum_{j=1}^{i-1} B_{xji} + 2W_{1i} Z_i f_{ixi} \tag{9.48}$$

$$\dot{\lambda}_{yi} = -Kf_{iyi} + \sum_{j=i+1}^{n} B_{yij} - \sum_{j=1}^{i-1} B_{yji} + 2W_{1i} Z_i f_{iyi} \tag{9.49}$$

$$\dot{\lambda}_{zi} = \sum_{j=i+1}^{n} B_{zij} - \sum_{j=1}^{i-1} B_{zji} + 2W_{1i} Z_i \tag{9.50}$$

with

$$\begin{aligned} B_{xij} &= \frac{2W_2\left(x_i - x_j\right)}{d_{ij}^2} \\ B_{yij} &= \frac{2W_2\left(y_i - y_j\right)}{d_{ij}^2} \\ B_{zij} &= \frac{2W_2\left(z_i - z_j\right)}{d_{ij}^2} \end{aligned} \tag{9.51}$$

for vehicle avoidance flight or

$$\begin{aligned} B_{xij} &= 4W_2\left(d_{ij} - d_{cij}\right)\left(x_i - x_j\right) \\ B_{yij} &= 4W_2\left(d_{ij} - d_{cij}\right)\left(y_i - y_j\right) \\ B_{zij} &= 4W_2\left(d_{ij} - d_{cij}\right)\left(z_i - z_j\right) \end{aligned} \tag{9.52}$$

for formation flight.

Next, the differential equations for the heading angles and flight path angles were derived in a similar manner as above. The first two equations are applicable to vehicle 1 through vehicle n-1. The last two equations are for vehicle n.

$$\underset{i=1:n-1}{\dot{\psi}_i} = \frac{\cos\psi_i\left[\dot{\lambda}_{yi}\cos\psi_i - \dot{\lambda}_{xi}\sin\psi_i\right]}{\lambda_{xi}} \tag{9.53}$$

$$\underset{i=1:n-1}{\dot{\gamma}_i} = \frac{\cos\psi_i\cos\gamma_i\left[\dot{\lambda}_{zi}\cos\gamma_i - \sin\gamma_i\left(\dot{\lambda}_{yi}\sin\psi_i + \dot{\lambda}_{xi}\cos\psi_i\right)\right]}{\lambda_{xi}} \tag{9.54}$$

$$\dot{\gamma}_n = \frac{V_n \prod_{i=1}^{n-1} (\cos\gamma_i \cos\psi_i)\left[-\dot{\lambda}_{zn}\cos\gamma_n + \sin\gamma_n\left(\dot{\lambda}_{yn}\sin\psi_n + \dot{\lambda}_{xn}\cos\psi_n\right)\right]}{A_4 \prod_{i=1}^{n-1}(\cos\gamma_i\cos\psi_i) + \sum_{i=i}^{n-1}\left[V_i\lambda_{xi}\prod_{\substack{j=1\\ j\neq i}}^{n-1}(\cos\gamma_j\cos\psi_j)\right]} \tag{9.55}$$

$$\dot{\psi}_n = \frac{V_n \prod_{i=1}^{n-1} (\cos\gamma_i \cos\psi_i)\left[\dot{\lambda}_{xn}\sin\psi_n - \dot{\lambda}_{yn}\cos\psi_n\right]}{\cos\gamma_n\left\{A_4 \prod_{i=1}^{n-1}(\cos\gamma_i\cos\psi_i) + \sum_{i=i}^{n-1}\left[V_i\lambda_{xi}\prod_{\substack{j=1\\ j\neq i}}^{n-1}(\cos\gamma_j\cos\psi_j)\right]\right\}} \tag{9.56}$$

This results in a system with 6n-1 differential equations – the 3n state equations, the n heading angle equations, n flight path angle equations, and the n-1 costates, λ_{xi} – with 3n-1 unknown initial values.

9.2.1 Legendre-Clebsch Necessary Conditions

For this formulation, the Hamiltonian equation is

$$H = A_4 + \sum_{i=1}^{n}\left[\lambda_{xi}V_i\cos\gamma_i\cos\psi_i + \lambda_{yi}V_i\cos\gamma_i\sin\psi_i + \lambda_{zi}V_i\sin\gamma_i\right] \tag{9.57}$$

and the costates are

$$\begin{aligned}\lambda_{yi} &= \lambda_{xi}\frac{\sin\psi_i}{\cos\psi_i}\\ \lambda_{zi} &= \lambda_{xi}\frac{\sin\gamma_i}{\cos\psi_i\cos\gamma_i}\end{aligned} \tag{9.58}$$

for i = 1:n-1 and for the nth vehicle they are

$$\lambda_{xn} = \frac{-\cos\gamma_n \cos\psi_n}{V_n} H_1$$
$$\lambda_{yn} = \frac{-\cos\gamma_n \sin\psi_n}{V_n} H_1 \tag{9.59}$$
$$\lambda_{zn} = \frac{-\cos\gamma_n \sin\psi_n}{V_n} H_1$$

with

$$H_1 = \frac{A_4 \prod_{i=1}^{n-1} (\cos\gamma_i \cos\psi_i) + \sum_{i=i}^{n-1} \left[V_i \lambda_{xi} \prod_{\substack{j=1 \\ j\neq i}}^{n-1} (\cos\gamma_j \cos\psi_j) \right]}{\prod_{i=1}^{n-1} (\cos\gamma_i \cos\psi_i)} \tag{9.60}$$

There are 2n controls for this problem, represented by the vector

$$u = \begin{bmatrix} \psi_1 \\ \vdots \\ \psi_n \\ \gamma_1 \\ \vdots \\ \gamma_n \end{bmatrix} \tag{9.61}$$

Taking the second partial derivative of the Hamiltonian and substituting in the algebraic expressions for the costates will result in the following matrix.

$$H_{uu} = \begin{bmatrix} \frac{-\lambda_{xi} V_i \cos\gamma_i}{\cos\psi_i} & 0 & 0 & 0 & 0 & 0 & 0 & 0 \\ 0 & \ddots & 0 & 0 & 0 & 0 & 0 & 0 \\ 0 & 0 & \frac{-\lambda_{xn-1} V_{n-1} \cos\gamma_{n-1}}{\cos\psi_{n-1}} & 0 & 0 & 0 & 0 & 0 \\ 0 & 0 & 0 & (\cos\gamma_n)^2 H_1 & 0 & 0 & 0 & 0 \\ 0 & 0 & 0 & 0 & \frac{-\lambda_{xi} V_i}{\cos\psi_i \cos\gamma_i} & 0 & 0 & 0 \\ 0 & 0 & 0 & 0 & 0 & \ddots & 0 & 0 \\ 0 & 0 & 0 & 0 & 0 & 0 & \frac{-\lambda_{xn-1} V_{n-1}}{\cos\psi_{n-1} \cos\gamma_{n-1}} & 0 \\ 0 & 0 & 0 & 0 & 0 & 0 & 0 & H_1 \end{bmatrix} \tag{9.62}$$

Similar to the two-vehicle formulation, the following inequalities must be satisfied.

$$\begin{aligned} &\frac{-\lambda_{xi} V_i}{\cos\psi_i \cos\gamma_i} \geq 0; \quad i = 1:n-1 \\ &H_1 \geq 0 \end{aligned} \tag{9.63}$$

9.2.2 Weierstrass Test

Substituting the optimal costate equations into the Hamiltonian equation will result in the following expression for the variational Hamiltonian.

$$\begin{aligned} &H(\psi_1, \psi_2) = A_4 \cos\psi_1^o \cos\gamma_1^o \left[1 - C\ \right] + \lambda_{x1} V \left[C_2 - C_1\right] \geq 0 \\ &C_1 = \cos\gamma_2 \cos\gamma_2^o \cos\left(\psi_2 - \psi_2^o\right) + \sin\gamma_2 \sin\gamma_2^o \\ &C_2 = \cos\gamma_1 \cos\gamma_1^o \cos\left(\psi_1 - \psi_1^o\right) + \sin\gamma_1 \sin\gamma_1^o \end{aligned} \tag{9.64}$$

In Appendix B.2, it is proven that this condition will be satisfied if the following conditions true.

$$\left|A_4 \cos\psi_1^o \cos\gamma_1^o\right| \geq \left|\lambda_{x1} V_1\right| \tag{9.65}$$

$$sign(\lambda_{xi}) = -sign(\cos\psi_i) \tag{9.66}$$

Equation (9.66) must be met for *i*=1:n-1.

CHAPTER 10

3D MULTIPLE VEHICLE RESULTS

This chapter contains some results for case of using the 3D equations for multiple vehicles. Depicted are three cases using the aircraft avoidance formulation and one case considering formation flight for two vehicles. The first case considers flight over a flat plane. The second case considers a minimum time flight over a terrain with a hill. The third situation portrayed involves a terrain masking flight over the same terrain with a hill. The final case portrays a formation flight terrain masking flight.

The first case presented is for a flight over a flat plane. In this case, the minimum time and terrain masking variations will be the same. Figure 10.1 first contains the results when no correction for multiple vehicles is made. In the plot on the left, the trajectories for this case can be seen. The plot on the right depicts the distance between the two vehicles during this flight. It can be seen here that the two vehicles would crash if allowed to fly these trajectories.

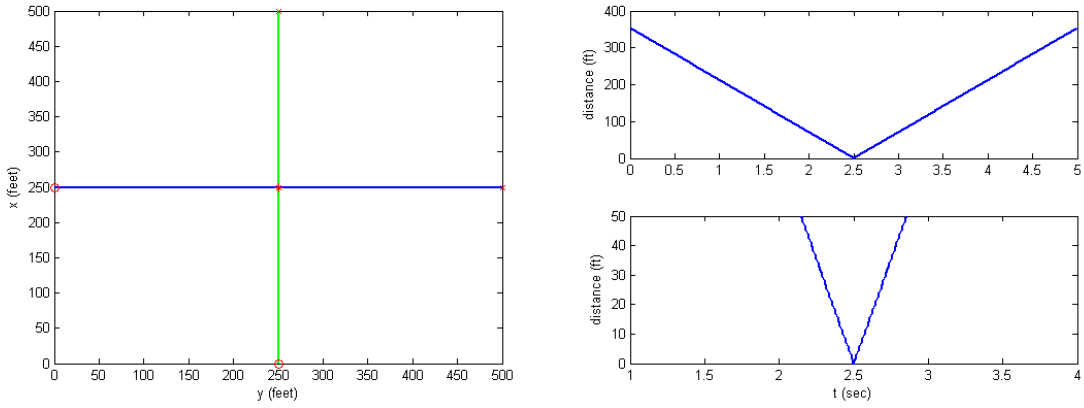

Figure 10.1: Results for two vehicles with no correction for multiple vehicles.

Figure 10.2 contains the results for this same situation, but with the addition of the multiple vehicle variation. Again, the plot on the left shows the trajectories while the plot on the right shows the distance between the two vehicles at all time. In this case, it can be seen that the minimum distance between the vehicles is about 75 feet. This point is represented on the plot on the left by the red stars. The controls for these flights can be seen in Figure 10.3. It can be seen that there is some mild oscillations in the flight path angles.

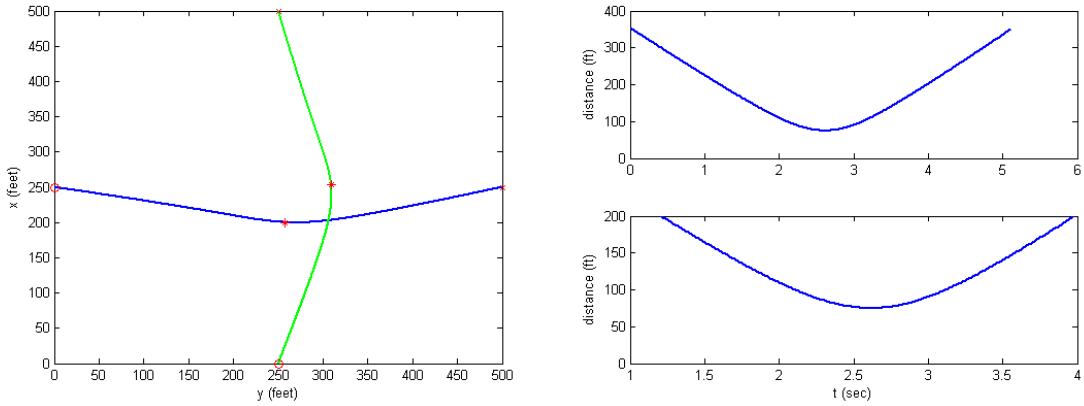

Figure 10.2: Results for two vehicles with correction for multiple vehicles.

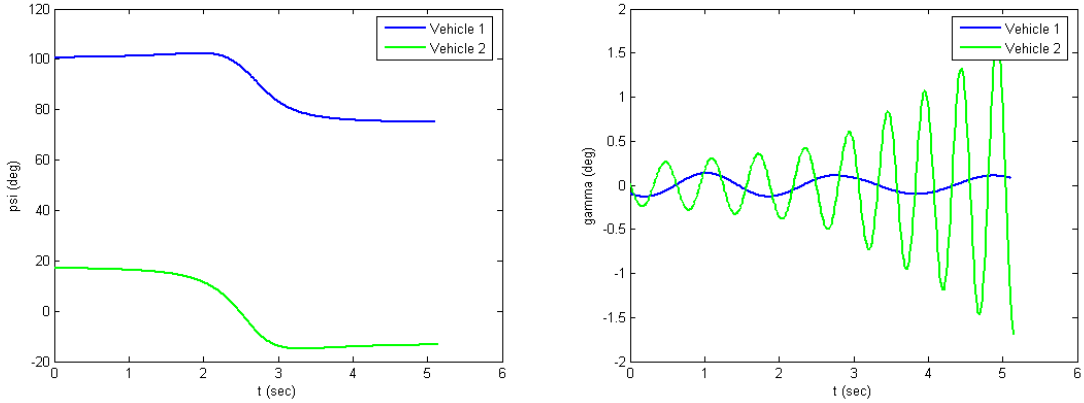

Figure 10.3: Controls for aircraft avoidance flight.

The results from the second variation tests are depicted in Figure 10.4 and Figure 10.5. It was shown in Chapter 9 that the inequalities in (10.1) must be satisfied for the Legendre-Clebsch condition and the equations in (10.2) and (10.3) must be true to satisfy the Weierstrass test.

$$\begin{aligned} &\frac{-\lambda_{x1} V_1}{\cos\psi_1 \cos\gamma_1} \geq 0 \\ &\frac{A_4 \cos\gamma_1 \cos\psi_1 + \lambda_{x1} V_1}{\cos\gamma_1 \cos\psi_1} \geq 0 \end{aligned} \tag{10.1}$$

$$W = \left| A_4 \cos\psi_1^o \cos\gamma_1^o \right| - \left| \lambda_{x1} V_1 \right| \geq 0 \tag{10.2}$$

$$sign(\lambda_{x1}) = -sign[\cos(\psi_1)] \tag{10.3}$$

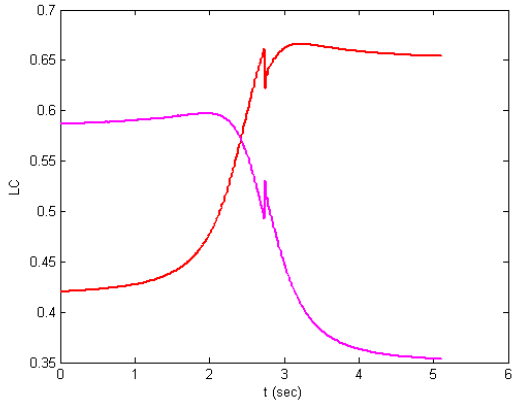

Figure 10.4: Inequalities from Legendre-Clebsch condition.

The functions from the Legendre-Clebsch condition are plotted in Figure 10.4 while the functions from the Weierstrass test can be seen in Figure 10.5. The plot on the left contains the plot of the function from the inequality in (10.1). The plot on the right contains the results of the signs. It can be seen that both of these conditions are satisfied at all times.

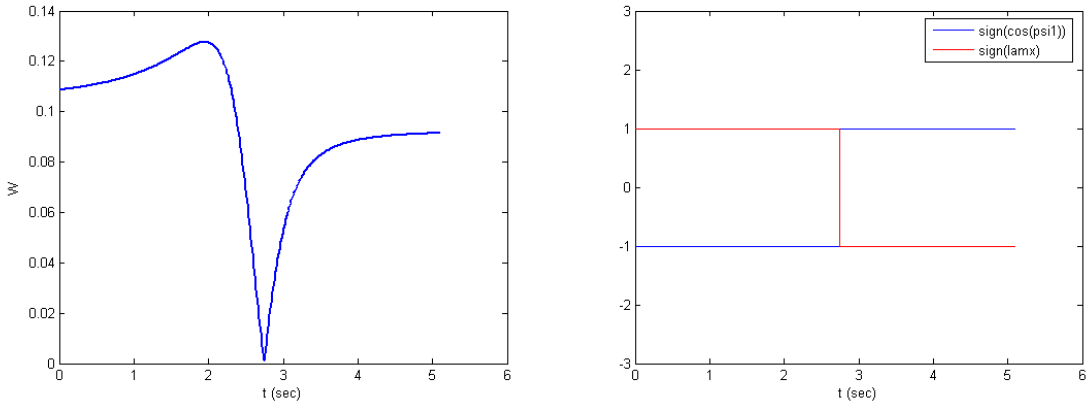

Figure 10.5: Results from Weierstrass test.

The second case is presented in Figure 10.6. This considers the case of a minimum time flight over a terrain of a flat plain with a single hill. The 3D view of the trajectories can be seen on the left while the overhead view of the trajectories can be seen on the right. For this situation, it can be seen that one vehicle flies straight over the hill while the other vehicle flies around the hill. The distance between the vehicles can be seen in Figure 10.7. The minimum distance is about 125 feet and is marked along the trajectories by the blue stars. The controls for this case can be seen plotted in Figure

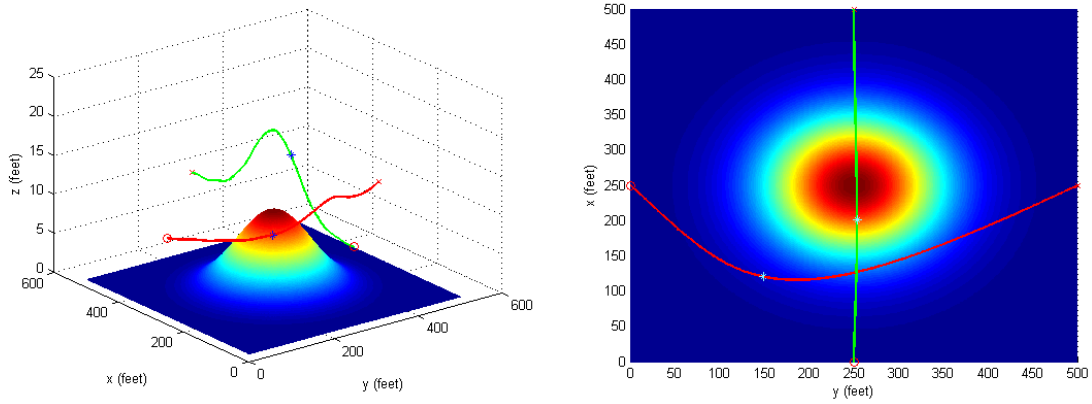

Figure 10.6: Trajectories for $K = 0$.

10.8. The results from the second variation analysis can be seen plotted in Figure 10.9 – the Legendre-Clebsch condition – and in Figure 10.10 – the Weierstrass test.

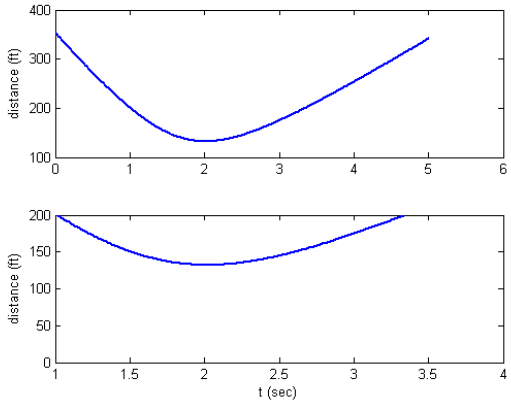

Figure 10.7: Distance between vehicles for all time.

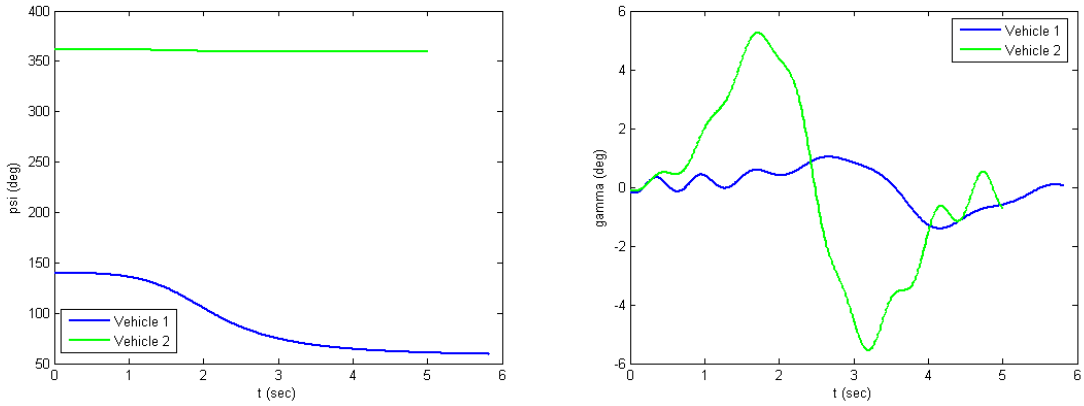

Figure 10.8: Controls for aircraft avoidance $K = 0$ flight.

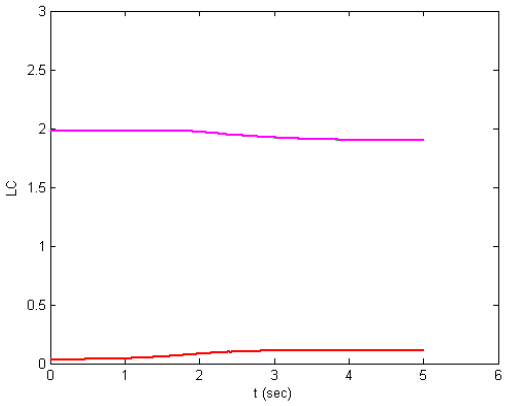

Figure 10.9: Inequalities from Legendre-Clebsch condition.

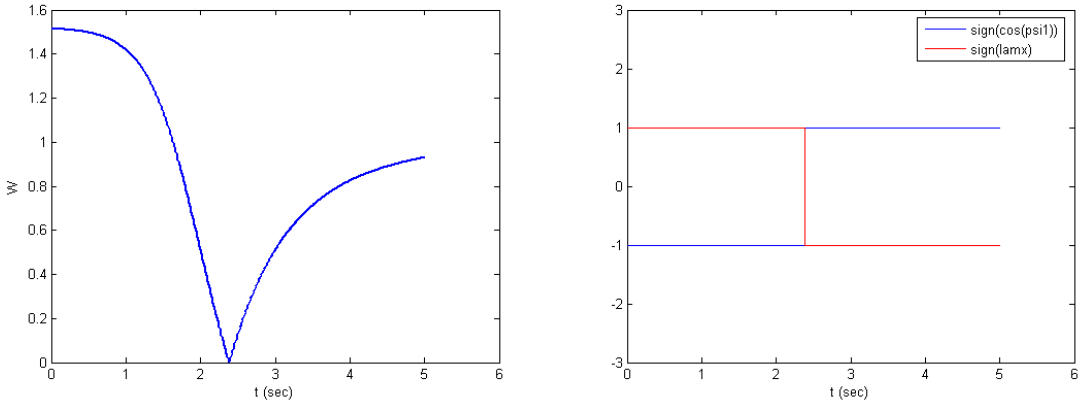

Figure 10.10: Results from Weierstrass test.

The next set of results considers the terrain masking case. This situation also uses the flat plane with a single hill as in the previous results. The plot of these trajectories can be seen in Figure 10.11. In this formulation, both of the vehicles circle the hill in a counter-clockwise fashion. This distance between the vehicles is plotted in Figure 10.12. The closest distance between the vehicles is 292 feet is this point is shown in Figure 10.11 by the blue star. The controls for these flights are shown in Figure 10.13. In checking the second variation, the results from the Legendre-Clebsch condition are

plotted in Figure 10.14 while the results from the Weierstrass test are plotted in Figure 10.15.

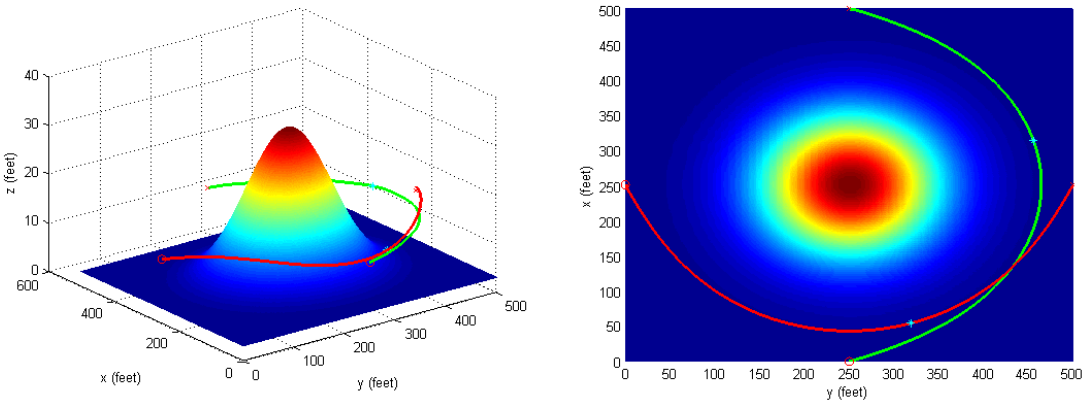

Figure 10.11: Trajectories for $K = 1$.

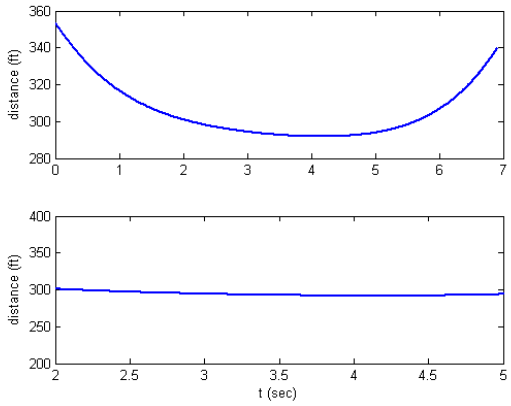

Figure 10.12: Distance between vehicles for all time.

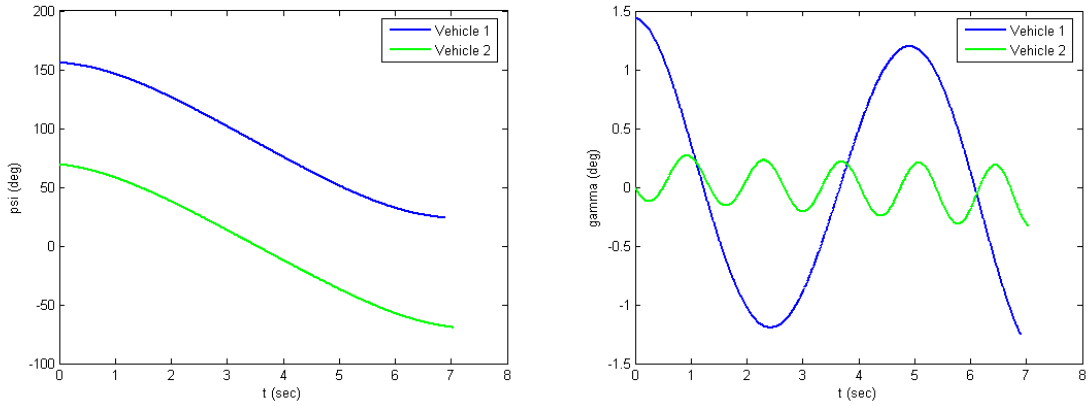

Figure 10.13: Controls for aircraft avoidance $K = 1$ flights.

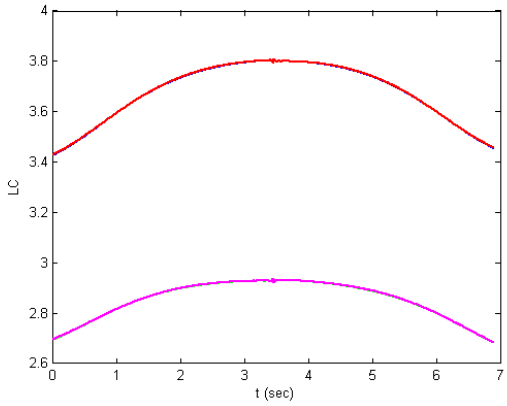

Figure 10.14: Results from Legendre-Clebsch condition.

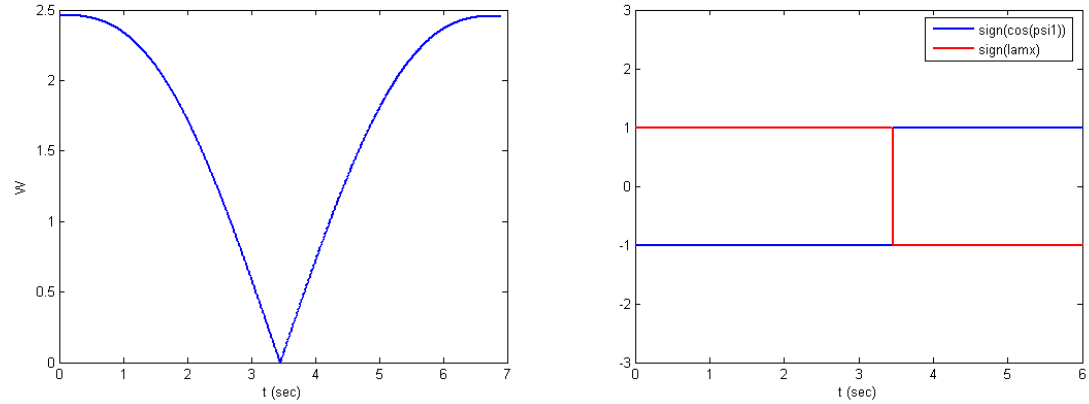

Figure 10.15: Results from Weierstrass test.

The final result depicts a case of formation flight for the two vehicles. The plots of these trajectories can be seen in Figure 10.16 and the corresponding controls can be seen in Figure 10.17. In this plot, it can be seen that the vehicles circle the hill with parallel paths. The results from the second variation analysis can be seen in Figure 10.18 and Figure 10.19. The inequalities from the Legendre-Clebsch condition are plotted in Figure 10.18 and the functions from the Weierstrass test are depicted in Figure 10.19.

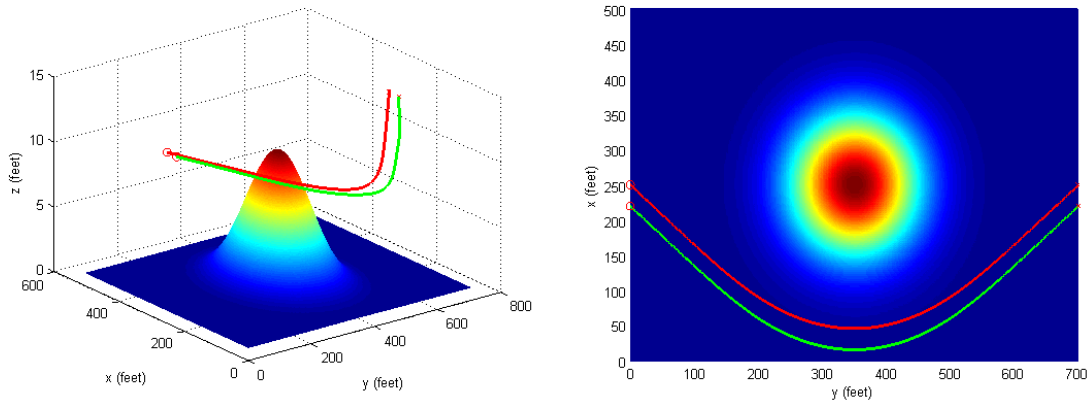

Figure 10.16: Trajectories for formation flight.

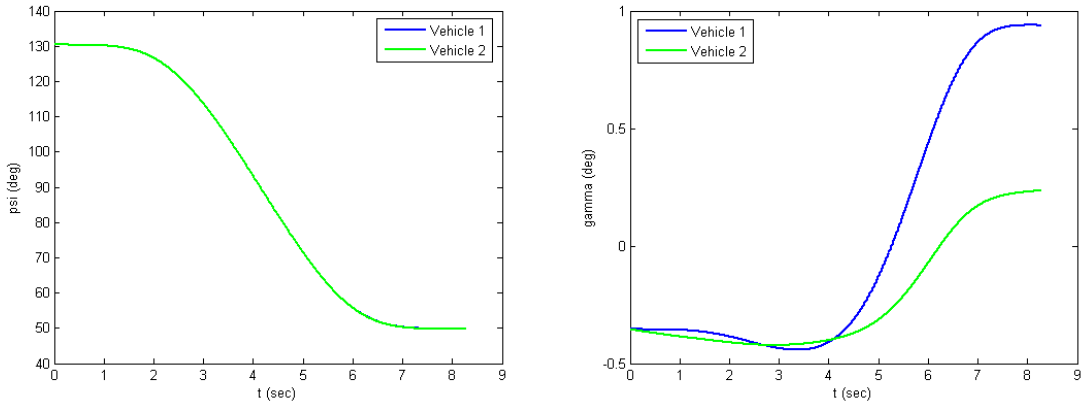

Figure 10.17: Controls for formation flight.

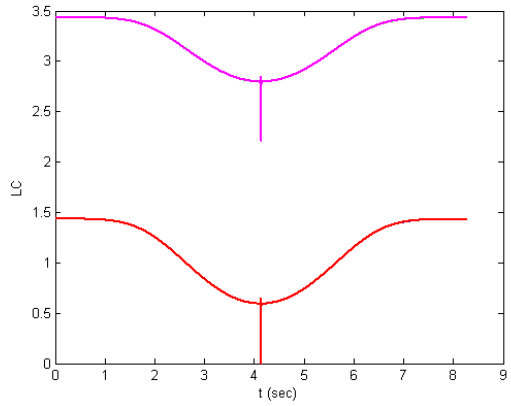

Figure 10.18: Results from Legendre-Clebsch condition.

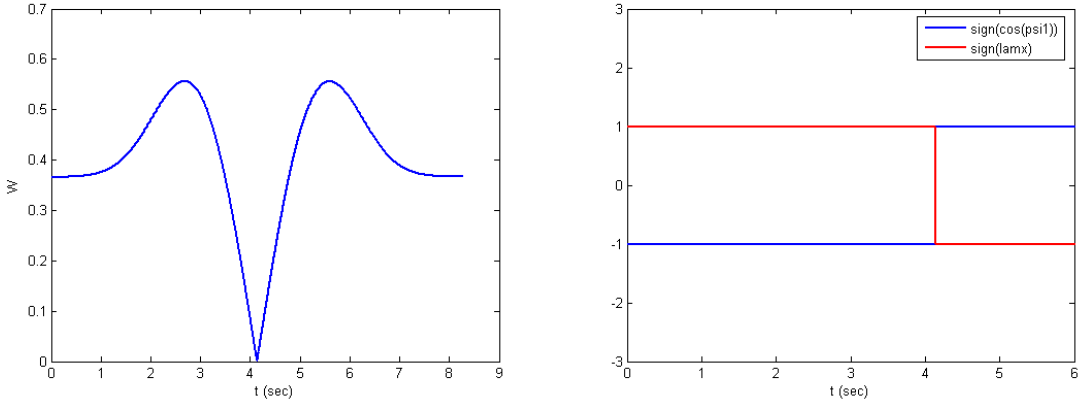

Figure 10.19: Results from Weierstrass test.

CHAPTER 11

SOLVING THE PROBLEM

In order to solve these problems, it was necessary to find between one and seven initial conditions to optimize the trajectories, depending on the formulation. Two different methods were utilized to find these initial conditions, depending on the number necessary. When only one value was needed, a variable step sweep was employed to find it. Otherwise a genetic algorithm was used.[41-43]

To begin the genetic algorithm, a set of 48 chromosomes was initialized representing different sets of initial conditions to test. Each initial value in the chromosomes was represented by digits with five decimal places included. In addition the costates, flight path angles and Hamiltonian values included an extra digit to indicate a positive or negative value.

After the chromosomes were initialized, they were each tested to determine their relative costs. To accomplish this, the current chromosome being tested was broken into its respective initial conditions, which were then used in the differential equations. The cost, J, was found for the run as well as the distance from the final position of the run to the final target position. The sum of these two values was used as the total cost for the chromosome.

After each chromosome was tested and a total cost assigned, the chromosomes were ranked from last to first based on a tournament procedure. Two chromosomes would be randomly chosen to compete and the one with the higher cost was placed in the next position on the list while the one with the lower cost was returned to the available

set of chromosomes to be tested. This process was continued until all the chromosomes were ranked. The top 24 chromosomes were then kept to begin the next generation.

In all subsequent generations, the 24 available chromosomes were combined to create 24 new chromosomes to complete the population of 48. Here, chromosomes 1 and 2 would be combined to create two new chromosomes, and then chromosomes 3 and 4 would be combined to create two new chromosomes and so on until all the chromosomes were mixed. This was accomplished by first mixing the individual segments of the chromosomes so that each of the new chromosomes had some segments from each parent, where a segment consisted of the digits for each initial condition needed. Next a mutation was introduced into the new chromosomes such that up to about a third of the digits could be changed. The number of digits changed, which digits were changed, and their new values were all determined randomly. After all the new chromosomes were created, the cost assignment and tournament were repeated as before. This process was repeated until it converged on a solution.

The differential equations were solved using a standard fourth order Runge-Kutta method. In addition, a variable time step was implemented to decrease the time needed to numerically solve the set of differential equations. For most of the flight, the time step was 0.1 seconds; however, when the distance to the target final position was close enough, the time step was decreased to 0.01 seconds.

Another condition was added to the differential equation solver to help decrease the solving time of the genetic algorithms. For each formulation, inequalities were derived that had to be satisfied at all times in order for the Legendre-Clebsch necessary condition and the Weierstrass test to be satisfied. These inequalities were then tested at

each time step. If either was violated, then the current run was ended at that point. This decreased the solving time significantly, but was even more useful in ensuring the convergence to a strong local minimum.

Table 11.1 contains some average run times for the different formulations. This table contains the number of initial conditions to be solved for, the run time length for each problem, then the average time it took to solve the problem. It can be seen that the single vehicle formulations were all generally solved in less than a minute for a case with a run time of 10 seconds. The multiple vehicle formulations took longer to solve because those cases tended to have a large number of local minima.

Table 11.1: Time to Solve

Formulation	Number of Variables	Run time	Time to Solve
Pseudo 3D	1	10 sec	25 sec
3D	2	10 sec	40 sec
Varying Velocity	3	10 sec	65 sec
2-vehicle	3	25 sec	6 min
3-vehicle	5	25 sec	15 min
4-vehicle	7	25 sec	60 min
2-vehicle 3D	5	10 sec	10 min

CHAPTER 12

CONCLUSIONS

This thesis examined path planning methods using a reduced order formulation for both single and multiple vehicles. In all cases the cost equation was set such that the path could be optimized with respect to either minimizing flight time or terrain masking. For most of the formulations, a constant velocity assumption was made, although one attempt was made at creating a more realistic varying velocity approach.

To begin with two pseudo-3D equations of motion were utilized and the altitude was constrained to be a set height above the terrain. It was found, in general, that there was very little difference between the paths found with these two sets of equations of motion. One problem, though, was accounting for the time necessary to move vertically. The simplified equations of motion ignored this detail entirely, while the local tangent plane equations of motion were able to mostly account for it.

This formulation was expanded to use a full set of 3D equations of motion, which allow a little more realism in the problem formulation. In addition, a greater variety of problems can be examined, such as the case when the vehicle does not start the desired distance above the terrain. This formulation also fully accounts for the time to fly vertically. Also, a simplified varying velocity component was added to the 3D equations of motion by including the velocity as an additional state. For this, the vehicle is now assumed to be flying with a constant – maximum – thrust. Now, the path generated will more accurately lose speed going uphill and gain speed going downhill.

The formulations using the two sets of pseudo-3D equations of motion as well as the full 3D equations of motion were also examined in the case of simultaneous path planning for multiple vehicles. In these cases, two different situations were examined. The first was the situation of aircraft avoidance such as having two vehicles operating in the same area and ensuring they do not collide. The second involves the case of formation flight. For all sets of equations of motion considered, the necessary equations to generate the paths were derived for an unspecified n- number of vehicles. Results are depicted for 2, 3, and 4 vehicles using the pseudo-3D equations of motion and for 2 vehicles using the 3D equations of motion.

One major problem with this multiple vehicle formulation is that the number of differential equations to be solved and the number of initial conditions to be found increases quickly with the number of vehicles considered. Using the pseudo-3D equations of motion, there will be 4n-1 differential equations and 2n-1 unknown initial conditions. Using the full 3D equations of motion, there will be 6n-1 differential equations and 3n-1 unknown initial conditions. This means that the solving times can become lengthy.

To create trajectories that better mimic actual flight capabilities, a better varying velocity model and rate constraints should be added. At this point, a very simple velocity model is used. Improving this model will better reflect a vehicles speed flying over hills and around sharp turns. Including an angle of attack constraint or acceleration constraint will also create a better representative model for horizontal maneuvering. As seen with the simulator comparisons, limits on both the heading angle and flight path angle rates are being reached, causing the simulator to be unable to accurately follow the designated path. Some method of limiting these rates should be incorporated. These additions will

greatly increase the flyability of the optimal paths, thereby increasing the safety of the missions.

APPENDIX A

SECOND VARIATION ANALYSIS

Optimal control for a problem can be proved using various tests of the second variation of the problem.[44] A sufficient condition for a weak local minimum is that the second variation be strongly positive. To achieve this, two conditions must be met. First the Legendre-Clebsch necessary condition must be met, and then the Jacobi test for conjugate points must be satisfied. To show that the extremals provide a strong local minimum, the Weierstrass condition must be satisfied.

A.1 Legendre-Clebsch Necessary Condition

The Legendre-Clebsch necessary condition[44] considers the positive-definiteness of the second partial derivative of the Hamiltonian equation such that

$$H_{uu} \geq 0 \tag{A.1}$$

or, for the strengthened form

$$H_{uu} > 0 \tag{A.2}$$

where

$$H_{uu} = \begin{bmatrix} H_{u_1u_1} & \cdots & H_{u_1u_n} \\ \vdots & \ddots & \vdots \\ H_{u_nu_1} & \cdots & H_{u_nu_n} \end{bmatrix} \tag{A.3}$$

In these equations, u represents the vector of control variables for the optimal control problem such that

$$u = \begin{bmatrix} u_1 \\ \vdots \\ u_n \end{bmatrix} \tag{A.4}$$

If equation (A.2) is satisfied for every time step, the extremals will be smooth and provide a weak local minimum for sufficiently short intervals.

A.2 Weierstrass Test

The Weierstrass test[44-47] can be used to verify an extremal is a strong local minimum. From the calculus of variations, the Weierstrass test is stated such that the Weierstrass excess function must be positive.[45, 46]

$$E(x, \dot{x}, p) = f(x, \dot{x}) - f(x, p) - (\dot{x} - p)\frac{\partial f(x, p)}{\partial p} \geq 0 \tag{A.5}$$

This can be shown to be the same as the Variational Hamiltonian *H(u)*.[44] This test states

$$H(t, x^o, \lambda^o, u) \geq H(t, x^o, \lambda^o, u^o) \tag{A.6}$$

where the superscript denotes an optimal value. When the Hamiltonian is not explicitly dependent on time, it will be equal to zero at all time with an optimal solution meaning

$$H(t, x^o, \lambda^o, u^o) = 0 \tag{A.7}$$

Thus

$$H(t, x^o, \lambda^o, u) \equiv H(u) \geq H(t, x^o, \lambda^o, u^o) = 0 \tag{A.8}$$

In the strengthened form, (A.8) should be equal to zero only when

$$u = u^o \tag{A.9}$$

The Variational Hamiltonian is found by inserting the algebraic equations for the optimal costates into the Hamiltonian equation evaluated at any test control point, such that

$$H(u) = A_4 + \lambda_x\left(u^o\right)\dot{x}(u) + \lambda_y\left(u^o\right)\dot{y}(u) + \cdots \tag{A.10}$$

A.3 Jacobi Condition

In the calculus of variations, an accessory-minimum problem is used to show that the second variation is nonnegative for extremals of finite length. This test attempts to find a neighboring solution that is competitive to being an optimal solution by searching for a system consisting of nonzero variations which also make the second variation zero. According to Ref. 45, given an extremal $x = x^o(t)$, the point M is said to be conjugate to X if M is the limit as $||x^o(t)-x(t)|| \rightarrow 0$ of the points of intersection of $x = x^o(t)$ and the neighboring extremal $x = x(t)$, starting from the same initial point X. To ensure at least a weak local minimum, it must be shown that there are no conjugate points.

The accessory minimum problem leads to an analysis of the nature of solutions to the linearized Euler-Lagrange equations. These equations can be solved algebraically, but would become quite involved. Instead, a numerical conjugate point test that was developed by H. J. Kelly and H. G. Moyer will be employed here.[34,47-48] The linearized Euler-Lagrange equations can be written as

$$\begin{bmatrix} \dot{x}_1 \\ \vdots \\ \dot{x}_n \end{bmatrix} = \begin{bmatrix} \dfrac{\partial x_1}{\partial \lambda^o_{x1}} & \cdots & \dfrac{\partial x_1}{\partial \lambda^o_{xn}} \\ \vdots & \ddots & \vdots \\ \dfrac{\partial x_n}{\partial \lambda^o_{x1}} & \cdots & \dfrac{\partial x_n}{\partial \lambda^o_{xn}} \end{bmatrix} \begin{bmatrix} \lambda^o_{x1} \\ \vdots \\ \lambda^o_{xn} \end{bmatrix} \tag{A.11}$$

where the matrix is composed of the partial derivatives of each state with respect to the initial costate values.

A conjugate point is marked as a time when the rank of the matrix drops. Therefore, if the matrix retains full rank at all time, there are no conjugate points to that extremal. In order to create this matrix, the following numerical approximation was used for each partial derivative.[49]

$$\frac{\partial x_i}{\partial \lambda_{xj}^o} = \frac{x_i\left(\lambda_{xj}^o + \Delta\lambda_{xj}\right) - x_i\left(\lambda_{xj}^o - \Delta\lambda_{xj}\right)}{2\Delta\lambda_{xj}} \tag{A.12}$$

This means that the initial values of each costate was perturbed both positively and negatively and this value was implemented in the set of differential equations to create two new vectors for each state. These values of the states from the perturbed costate initial conditions were then subtracted and this value was divided by twice the perturbation value. This process was repeated at every time step of the trajectory for the entire matrix. The rank of the matrix was then determined for every time step to ensure that it always has full rank at all time. All of the results presented in this thesis meet this requirement and it is not discussed specifically for each formulation.

APPENDIX B

MATHEMATICAL PROOFS

B.1 Single Vehicle 3D Weierstrass Test Proof

Considering the Weierstrass test for 3D equations of motion, it was found that

$$H(u) = A_4\left[1 - \left(\cos\psi\cos\psi^o + \sin\psi\sin\psi^o\right)\cos\gamma\cos\gamma^o - \sin\gamma\sin\gamma^o\right] \quad \text{(B.1)}$$

To satisfy the Weierstrass test, the following inequality must be satisfied.

$$H(u) \geq 0 \quad \text{(B.2)}$$

Equation (B.1) can be rewritten as

$$H(u) = A_4\left[1 - N\right] \quad \text{(B.3)}$$

where

$$N = \left(\cos\psi\cos\psi^o + \sin\psi\sin\psi^o\right)\cos\gamma\cos\gamma^o + \sin\gamma\sin\gamma^o \quad \text{(B.4)}$$

This section examines N from the previous equations. Given the trigonometric identity

$$\cos(a \pm b) = \cos a\ \cos b \mp \sin a\ \sin b \quad \text{(B.5)}$$

(B.4) can be rewritten as

$$N = \cos\left(\psi - \psi^o\right)\cos\gamma\cos\gamma^o + \sin\gamma\sin\gamma^o \quad \text{(B.6)}$$

or

$$= M\cos\gamma\cos\gamma^o + \sin\gamma\sin\gamma^o; \qquad M \in [-1 \quad 1] \quad \text{(B.7)}$$

where M is any number between -1 and 1.

Then the following identities can be substituted into (B.7)

$$\cos\alpha = \frac{e^{i\alpha} + e^{-i\alpha}}{2}$$
$$\sin\alpha = \frac{e^{i\alpha} - e^{-i\alpha}}{2i} \tag{B.8}$$

This will result in

$$N = M\left(\frac{e^{i\gamma} + e^{-i\gamma}}{2}\frac{e^{i\gamma^o} + e^{-i\gamma^o}}{2}\right) + \frac{e^{i\gamma} - e^{-i\gamma}}{2i}\frac{e^{i\gamma^o} - e^{-i\gamma^o}}{2i} \tag{B.9}$$

Multiplying the terms will result in

$$= \frac{M}{4}\left(e^{i(\gamma+\gamma^o)} + e^{-i(\gamma+\gamma^o)} + e^{i(\gamma-\gamma^o)} + e^{i(-\gamma+\gamma^o)}\right) +$$
$$\frac{1}{4}\left(-e^{i(\gamma+\gamma^o)} - e^{-i(\gamma+\gamma^o)} + e^{i(\gamma-\gamma^o)} + e^{i(-\gamma+\gamma^o)}\right) \tag{B.10}$$

Rearranging the terms will allow this to be rewritten as

$$= \frac{M+1}{2}\left[\frac{e^{i(\gamma-\gamma^o)} + e^{-i(\gamma-\gamma^o)}}{2}\right] + \frac{M-1}{2}\left[\frac{e^{i(\gamma+\gamma^o)} + e^{-i(\gamma+\gamma^o)}}{2}\right] \tag{B.11}$$

Using the identities from (B.8) will give

$$= \frac{M+1}{2}\cos(\gamma-\gamma^o) + \frac{M-1}{2}\cos(\gamma+\gamma^o) \tag{B.12}$$

$$= X\cos(\gamma-\gamma^o) + (X-1)\cos(\gamma+\gamma^o) \tag{B.13}$$

where

$$X = \frac{M+1}{2} \in [0 \quad 1]$$
$$A = \cos(\gamma - \gamma^o) \in [-1 \quad 1] \tag{B.14}$$
$$B = \cos(\gamma + \gamma^o) \in [-1 \quad 1]$$

The range of values for N from equations (B.13) – (B.14) are evaluated and summarized in Table B.1. It can be seen that when X is 0, N will be $-B$. Conversely, when X is 1, N will be the same as A. In addition, values for N when X is 0.5 are also displayed in the table.

Table B.1: Values for N

X	A	B	N
0		-1	1
0		0	0
0		1	-1
1	-1		-1
1	0		0
1	1		1
0.5	-1	-1	0
0.5	-1	0	-0.5
0.5	-1	1	-1
0.5	0	-1	0.5
0.5	0	0	0
0.5	0	1	-0.5
0.5	1	-1	1
0.5	1	0	0.5
0.5	1	1	0

It can be seen from the table that

$$N \in [-1 \quad 1] \tag{B.15}$$

Therefore

$$1 - N \in [0 \quad 2] \tag{B.16}$$

B.2 Multiple Vehicle Weierstrass Test Proof

Examining the Weierstrass test for the 2-vehicle simplified equations of motion results in

$$H(\psi_1,\psi_2) = A_4\left[1-\cos\left(\psi_2^o-\psi_2\right)\right]+\frac{\lambda_{x1}V_1}{\cos\psi_1^o}\left[\cos\left(\psi_1^o-\psi_1\right)-\cos\left(\psi_2^o-\psi_2\right)\right] \quad \text{(B.17)}$$

To satisfy the Weierstrass condition, equation (B.17) must be positive.

$$A_4\left[1-\cos\left(\psi_2^o-\psi_2\right)\right]+\frac{\lambda_{x1}V_1}{\cos\psi_1^o}\left[\cos\left(\psi_1^o-\psi_1\right)-\cos\left(\psi_2^o-\psi_2\right)\right]\geq 0 \quad \text{(B.18)}$$

Multiplying through by $\cos\psi_1^o$ will result in two possible inequalities, depending on the sign of $\cos\psi_1^o$.

$$\begin{aligned} &A_4\cos\psi_1^o\left[1-\cos\left(\psi_2^o-\psi_2\right)\right]+\lambda_{x1}V_1\left[\cos\left(\psi_1^o-\psi_1\right)-\cos\left(\psi_2^o-\psi_2\right)\right]\geq 0;\ \cos\psi_1^o\geq 0\\ &A_4\cos\psi_1^o\left[1-\cos\left(\psi_2^o-\psi_2\right)\right]+\lambda_{x1}V_1\left[\cos\left(\psi_1^o-\psi_1\right)-\cos\left(\psi_2^o-\psi_2\right)\right]\leq 0;\ \cos\psi_1^o\leq 0\end{aligned} \quad \text{(B.19)}$$

Next, defining the following equality

$$N=\cos\left(\psi_2^o-\psi_2\right) \quad \text{(B.20)}$$

and substituting it into (B.19) will result in

$$\begin{aligned} &A_4\cos\psi_1^o\left[1-N\right]+\lambda_{x1}V_1\left[\cos\left(\psi_1^o-\psi_1\right)-N\right]\geq 0;\quad \cos\psi_1^o\geq 0\\ &A_4\cos\psi_1^o\left[1-N\right]+\lambda_{x1}V_1\left[\cos\left(\psi_1^o-\psi_1\right)-N\right]\leq 0;\quad \cos\psi_1^o\leq 0\end{aligned} \quad \text{(B.21)}$$

with

$$\begin{aligned} &N\in\left[-1\quad 1\right]\\ &\cos\left(\psi_1^o-\psi_1\right)\in\left[-1\quad 1\right]\end{aligned} \quad \text{(B.22)}$$

Now let

$$\begin{aligned} &M=1-N\\ &P=\cos\left(\psi_1^o-\psi_1\right)-N\end{aligned} \quad \text{(B.23)}$$

and (B.21) can be rewritten as

$$\begin{aligned} A_4 \cos\psi_1^o M &\geq -\lambda_{x1} V_1 P; \quad \cos\psi_1^o \geq 0 \\ A_4 \cos\psi_1^o M &\leq -\lambda_{x1} V_1 P; \quad \cos\psi_1^o \leq 0 \end{aligned} \tag{B.24}$$

where

$$\begin{aligned} M &\in [0 \quad 2] \\ P &\in [(M-2) \quad M] \end{aligned} \tag{B.25}$$

Therefore

$$\begin{aligned} M = 2 \quad &\Rightarrow \quad P \in [0 \quad 2] \\ M = 1 \quad &\Rightarrow \quad P \in [-1 \quad 1] \\ M = 0 \quad &\Rightarrow \quad P \in [-2 \quad 0] \end{aligned} \tag{B.26}$$

First, the top inequality from (B.24) will be evaluated, where $\cos\psi_1^o$ is positive. A summary of this evaluation is given in Table B.2. From the first case, it can be found that λ_{x1} must always be negative. In the fourth and fifth cases, both sides of the inequality are positive, so the left side must e more positive.

Table B.2: Evaluation of Top Inequality

M	P	Given inequality	Needed condition
0	-2	$0 \geq 2\lambda_{x1} V_1$	$\lambda_{x1} \leq 0$
0	0	$0 \geq 0$	Always satisfied
2	0	$2A_4 \cos\psi_1^o \geq 0$	Always satisfied
2	2	$A_4 \cos\psi_1^o \geq -\lambda_{x1} V_1$	$A_4 \cos\psi_1^o \geq -\lambda_{x1} V_1$
1	1	$A_4 \cos\psi_1^o \geq -\lambda_{x1} V_1$	$A_4 \cos\psi_1^o \geq -\lambda_{x1} V_1$
1	-1	$A_4 \cos\psi_1^o \geq \lambda_{x1} V_1$	Always satisfied given $\lambda_{x1} \leq 0$

Next the bottom inequality from (B.35) is examined. In this situation, $\cos\psi_1^o$ is negative. A summary of the evaluation of this inequality is presented in Table B.3. In the first case examined, it is found that λ_{x1} must always be positive. In the fourth and fifth, both sides of the inequality will be negative, so the left side must be more negative. Combining the results from this evaluation with the previous one, some general conclusions can be made to ensure the inequality from (B.19) is always satisfied.

$$\begin{aligned} &sign(\lambda_{x1}) = -sign\left(\cos\psi_1^o\right) \\ &\left|A_4\cos\psi_1^o\right| \geq \left|\lambda_{x1}V_1\right| \end{aligned} \tag{B.27}$$

Table B.3: Evaluation of Bottom Inequality

M	P	Given inequality	Needed condition
0	-2	$0 \leq 2\lambda_{x1}V_1$	$\lambda_{x1} \geq 0$
0	0	$0 \leq 0$	Always satisfied
2	0	$2A_4\cos\psi_1^o \leq 0$	Always satisfied
2	2	$A_4\cos\psi_1^o \leq -\lambda_{x1}V_1$	$A_4\cos\psi_1^o \leq -\lambda_{x1}V_1$
1	1	$A_4\cos\psi_1^o \leq -\lambda_{x1}V_1$	$A_4\cos\psi_1^o \leq -\lambda_{x1}V_1$
1	-1	$A_4\cos\psi_1^o \leq \lambda_{x1}V_1$	Always satisfied given $\lambda_{x1} \geq 0$

REFERENCES

(1) Richards, Nathan D., Manu Sharma, David G. Ward. "A Hybrid A*/Automaton Approach to On-Line Path Planning with Obstacle Avoidance." AIAA 1st Intelligent Systems Technical Conference. 20-22 September, 2004.

(2) Yang, Hong Iris and Yiyuan J. Zhao. "Trajectory Planning for Autonomous Aerospace Vehicles amid Known Obstacles and Conflicts." Journal of Guidance, Control, and Dynamics 2004. vol. 27 no. 6 (997-1008).

(3) Madani, I. and D. Allerton. "An Optimized Routing Method for Terrain Referenced Navigation." AIAA Guidance, Navigation, and Control Conference and Exhibit. 21-24 August, 2006.

(4) Doebbler, J., P. Gesting and J. Valasek. "Real-Time Path Planning and Terrain Obstacle Avoidance for General Aviation Aircraft." AIAA Guidance, Navigation, and Control Conference and Exhibit. 15-18 August, 2005.

(5) Kehoe, J., A. Watkins and R. Lind. "A Time-Varying Hybrid Model for Dynamic Motion Planning of an Unmanned Air Vehicle. AIAA Guidance, Navigation, and Control Conference and Exhibit. 21-24 August, 2006.

(6) Amin, J., J. Boškovic and R. Mehra. "A Fast and Efficient Approach to Path Planning for Unmanned Vehicles." AIAA Guidance, Navigation, and Control Conference and Exhibit. 21-24 August, 2006.

(7) Bortoff, Scott A. "Path Planning for UAVs." Proceedings of the American Control Conference. June, 2000.

(8) Judd, Kevin B. and Timothy W. McLain. "Spline Based Path Planning for Unmanned Air Vehicles." AIAA Guidance, Navigation and Control Conference and Exhibit. 6-9 August, 2001.

(9) McLain, Timothy W., Phillip R. Chandler, Steve Rasmussen and Meir Prachter. "Cooperative Control of UAV Rendezvous." American Control Conference. 25-27 June, 2001.

(10) Chadler, Philip R., Meir Pachter and Steven Rasmussen. "UAV Cooperative Control." American Control Conference. 25-27 June, 2001.

(11) Chandle, P. R., S. Rasmussen and M. Pachter. "UAV Cooperative Path Planning." AIAA Guidance, Navigation and Control Conference and Exhibit. 14-17 August, 2000.

(12) McLain, Timothy W. and Randal W. Beard. "Trajectory Planning for Coordinated Rendezvous of Unmanned Air Vehicles." AIAA Guidance, Navigation, and Control Conference and Exhibit. 14-17 August, 2000.

(13) Yang, Guang and Vikram Kapila. "Optimal Path Planning for Unmanned Air Vehicles with Kinematic and Tactical Constraints." 41st IEEE Conference on Decision and Control. December, 2002.

(14) Wong, Hong, Vikram Kapila and Ravi Vaidyanathan. "UAV Optimal Path Planning using C-C-C Class Paths for Target Touring." 43rd IEEE Conference on Decision and Control. 14-17 December, 2004.

(15) Betts, John T. "Survey of Numerical Methods for Trajectory Optimization." Journal of Guidance, Control, and Dynamics 2001. vol. 21 no. 2 (193-207).

(16) Ringertz, Ulf. "Flight Testing an Optimal Trajectory for the Saab J35 Draken." Journal of Aircraft 2000. vol. 37 no. 1 (187 – 189).

(17) Ringertz, Ulf. "Optimal Trajectory for a Minimum Fuel Turn." Journal of Aircraft 2000. vol. 37 no. 5 (932 – 934).

(18) Herman, A. L., and B. A. Conway. "Direct Optimization Using Collocation Based on High-Order Gauss-Lobatto Quadrature Rules." Journal of Guidance, Control and Dynamics, vol. 19, no. 3 (1178-1181).

(19) Williams, P. "Real-Time Computation of Optimal Three-Dimensional Aircraft Trajectories Including Terrain-Following." AIAA Guidance, Navigation, and Control Conference and Exhibit. 21-24 August, 2006.

(20) Benson, D., G. Huntington, T. Thorvaldsen, and A. Rao. "Direct Trajectory Optimization and Costate Estimation via an Orthogonal Collocation Method." AIAA Guidance, Navigation, and Control Conference and Exhibit. 21-24 August, 2006.

(21) Riehl, J., S. Paris, and W. Sjauw. "Comparison of Implicit Integration Methods for Solving Aerospace Trajectory Optimization Problems." AIAA/AAS Astrodynamics SpecialistConference and Exhibit. 21-24 August, 2006.

(22) Paris, S., J. Riehl, and W. Sjauw. "Enhanced Procedures for Direct Trajectory Optimization Using Nonlinear Programming and Implicit Integration." AIAA/AAS Astrodynamics SpecialistConference and Exhibit. 21-24 August, 2006.

(23) Windhorst, Robert, Mark Ardema, and David Kinney. "Fixed-Range Optimal Trajectories of Supersonic Aircraft by First-Order Expansions." Journal of Guidance, Control, and Dynamics 2001. vol.24 no.4 (700-709).

(24) Dogan, Atilla. "Probabilistic Path Planning for UAVs." 2nd AIAA Unmanned Unlimited Systems, Technologies and Operations. 15-18 September, 2003.

(25) Lian, Feng-Li and Richard Murray. "Real-Time Trajectory Generation for the Cooperative Path Planning of Multi-Vehicle Systems." Proceeding of the 41st IEEE Conference on Decision and Control. December, 2002.

(26) Jardin, Matthew R. and Arthur E. Byson, Jr. "Neighboring Optimal Aircraft Guidance in Winds." Journal of Guidance, Control, and Dynamics 2001. vol. 24 no. 4 (710 – 715).

(27) Mulgund, Sandeep, et al. "Large-Scale Air Combat Tactics Optimization Using Genetic Algorithms." Journal of Guidance, Control, and Dynamics 2001. vol. 24 no. 1 (140 – 142).

(28) Yokoyama, Nobuhiro and Shinji Suzuki. "Modified Genetic Algorithm for Constrained Trajectory Optimization." Journal of Guidance, Control, and Dynamics 2005. vol. 28 no. 1 (139 – 144).

(29) Anderson, M., J. Lopez, and J. Evers. "A Comparison of Trajectory Determination Approaches for Small UAV's." AIAA Guidance, Navigation, and Control Conference and Exhibit. 21-24 August, 2006.

(30) Rubio, Juan Carlos, Juris Vagners and Rolf Rysdyk. "Adaptive Path Planning for Autonomous UAV Oceanic Search Missions." AIAA 1st Intelligent Systems Technical Conference. September, 2004.

(31) Rathbun, David, Sean Kragelund, Anawat Pongpunwattana, and Brian Capozzi. "An Evolution Based Path Planning Algorithm for Autonomous Motion of a UAV Through Uncertain Environments." The 21st Digital Avionics Systems Conference, 2002.

(32) Rathbun, David and Brian Capozzi. "Evolutionary Approaches to Path Planning Through Uncertain Environments." AIAA's 1st Technical Conference and Workshop on Unmanned Aerospace Vehicles. May 2002.

(33) Capozzi, Brian J. and Juris Vagners. "Evolution as a Guide for Autonomous Vehicle Path Planning and Coordination." Aerospace Conference Proceedings, 2002.

(34) Kim, Eulgon. *Optimal Helicopter Trajectory Planning for Terrain Following Flight.* Thesis. Georgia Institute of Technology. 1990.

(35) Menon, P.K., E. Kim, V.H.L. Cheng. "Optimal Trajectory Planning for Terrain Following Flight." Journal of Guidance, Control and Dynamics, Vol. 14, No. 4, July – August 1991 (807 – 813).

(36) Lu, Ping and Bion L. Pierson. "Optimal Aircraft Terrain-Following Analysis and Trajectory Generation." Journal of Guidance, Control and Dynamics, Vol. 18, No. 3, May – June 1995 (555 – 560).

(37) Ries, Tobias. *Full Dynamics 6DoF-Trajectory-Optimization of an Unmanned Aeronautical Vehicle (UAV).* Thesis. Georgia Institute of Technology / Universität Stuttgart. 2005.

(38) Locatelli, Arturo. *Optimal control: an introduction*. Basel: Birkhäuser Verlag, 2000.

(39) Ben-Asher, Joseph Z. and Isaac Yaesh. *Advances in Missile Guidance Theory*. AIAA, 1998.

(40) United States Geological Survey. Terrain Data. February 8, 2003. ftp://edcftp.cr.usgs.gov/pub/data/DEM/250/

(41) Falkenauer, Emanuel. *Genetic Algorithms and Grouping Problems.* Chichester: John Wiley & Sons. 1998.

(42) Vas, Peter. *Artificial – Intelligence – Based Electrical Machines and Drives*. New York: Oxford University Press. 1999.

(43) Kulankura, Krishnakumar. *Maching Fixture Synthesis using the Genetic Algorithm.* Thesis. Georgia Institute of Technology. 1999.

(44) Bryson, A.E., Jr. and Yu-Chi Ho. *Applied Optimal Control*. np:Hemisphere Publishing Corporation, 1975.

(45) Gelfand, I. M. and S. V. Fomin. *Calculus of Variations.* Englewood Cliffs, NJ: Prentice-Hall, 1963.

(46) Pinch, Enid R. *Optimal Control and the Calculus of Variations.* Oxford: Oxford University Press, 1993.

(47) Ben-Asher, Joseph Z. "Optimal Trajectories for an Unmanned Air-Vehicle in the Horizontal Plance." AIAA Atmospheric Flight Mechanics Conference. 10-12 August, 1992.

(48) Chowdhry, R. S., J. Z. Ben-Asher, and E. M. Cliff. "OptimalRigid Body Motions, part 1: Approximate Formulation." Journal of Optimization Theory and Applications, Vol. 70, No. 1, July, 1991.

(49) Pritchett, Amy. class notes. AE / IsyE 6779 Modeling and Simulation of Dynamic Systems. Georgia Institute of Technology. Spring 2005.

(50) Calise, A.J., "Singular Perturbation Techniques for On-Line Optimal Flight-Path Control," AIAA Journal of Guidance and Control, Vol. 4, No. 4, 1981.

(51) Vanderplaats, Garret N. *Numerical Optimization Techniques for Engineering Design: With Application*. New York: McGraw-Hill Publishing Company, 1984.